

TIME-RESOLVED GLOW DISCHARGE MASS SPECTROMETRY

by

JEFFREY A. KINISLEY

A DISSERTATION PRESENTED TO THE GRADUATE SCHOOL OF THE
UNIVERSITY OF FLORIDA IN PARTIAL FULFILLMENT OF THE REQUIREMENTS
FOR THE DEGREE OF DOCTOR OF PHILOSOPHY

UNIVERSITY OF FLORIDA

1990

This work is dedicated to my father, Alfred Mathias Klingler who taught me
everything I really need to know

ACKNOWLEDGEMENTS

I am indebted to my advisor, Dr. Wilbert Harrison, for his advice, guidance and encouragement throughout my graduate career. He has set a professional standard that I shall continually strive to achieve. I also wish to express my love and gratitude to my wife Kathy (who has been most patient and supportive these past five years) and to my parents who gave me the foundation upon which to build both a career and a life.

I wish to thank Mr. John Hunter, my supervisor while I was a chemistry technician in industry, who nearly seven years ago gave me the opportunity and encouragement I needed to earn, not only my bachelor's degree, but my doctorate as well. Special thanks also goes to Dr. Marie Hankins, my undergraduate advisor, whose support and advice have gone a long way in helping me work toward my degree.

My appreciation also goes out to the outstanding faculty and staff at the University of Florida. Particular appreciation is made to Beverly Lyle, Winola Douglas, Susan Cassanova, and Jeanne Kordly. These ladies made the paperwork machine run alot smoother. The men in the machine shop, who built many of the items that made my research possible, and Russel Pierce and Dave Mize in the electronics shop, have also been especially helpful. The assistance of Martin Guzik and Roger Motter at the University of Virginia is gratefully acknowledged.

Finally, I want to thank my colleagues, Tuan Mai, Philip Patel, Sun Choroants, and Chris Barfield who have shared the day-to-day trials of graduate school with me. They made it all a little more bearable.

This work has been supported by a grant from the U.S. Department of Energy.



Jeffrey A. King

University of Florida
Gainesville, Florida

July 28, 1981

TABLE OF CONTENTS

ACKNOWLEDGEMENTS	iii
KEY TO ABBREVIATIONS AND SYMBOLS	vi
ABSTRACT	ix
CHAPTER 1. GLOW DISCHARGE MASS SPECTROMETRY	1
Glow Discharges	1
Operation of the Glow Discharge	16
Sputter Emission	27
Monitoring the Glow Discharge	40
Analytical Applications	50
CHAPTER 2. INSTRUMENTATION	71
Mass Spectrometer Systems	71
Ion Detection	86
Data Handling	101
CHAPTER 3. PULSED DIRECT CURRENT GLOW DISCHARGE MASS SPECTROMETRY	107
Background	107
Equipment	116
The Prepeak Region	127
The Plateau Region	147
The Afterpeak Region	161
Applications to GDMR Spectra	171
CHAPTER 4. PULSED DUAL CATHODE GLOW DISCHARGE MASS SPECTROMETRY	183
Background	183
Equipment	184
Cross Contamination Between Cathodes	188
Analytical Applications	192

CHAPTER 5. RADIO FREQUENCY SLOW DISCHARGE MASS SPECTROMETRY	189
Experimental Considerations	189
Parameters Influencing r.f. Discharges	205
Comparison of d.c. and r.f. Discharges	219
Application to Nonconducting Samples	227
CHAPTER 6. AMPLITUDE MODULATED RADIO FREQUENCY SLOW DISCHARGE MASS SPECTROMETRY	259
Experimental Considerations	260
Comparison of Pulsed d.c. and Pulsed r.f. Discharges	268
Application to Nonconducting Samples	277
CHAPTER 7. CONCLUDING REMARKS	289
Overview	294
Future Studies	299
APPENDIX	309
REFERENCES	309
BIOGRAPHICAL SKETCH	308

KEY TO ABBREVIATIONS AND SYMBOLS

AA	atomic absorption
amu	atomic mass units
C_p	production rate coefficient for metastable atoms
C_r	concentration of the reference element
C_s	concentration of the analyte
d	distance between electrodes
D	Debye length
i_d	deci current
k	electron constant
f	frequency
GD	glow discharge
k	Boltzmann constant
l	length of cathode dark space
I_r	intensity of the reference peak
I_s	intensity of the analyte peak
m/c	mass-to-charge ratio
mfp	mean free path
MS	mass spectrometry
N_s	probability of ion reaching the surface without a collision
n_e	number density of electrons
n_m	number density of metastable atoms
n_n	number density of neutral atoms
NIST	National Institute of Science and Technology
p	pressure
r	radius of an atom (in cm)
r_0	distance from the quadrupole z-axis to the edge of the rods
r_f	rod frequency
RSD	relative standard deviation
RSF	relative sensitivity factor
S	sputter yield
SP	sensitivity factor
T_e	electron temperature
U	d.c. potential applied to quadrupole rods
v	mean velocity of an atom
V_{app}	applied voltage
V_z	electric field intensity at distance z
Y	loss rate for metastable atoms

α	secondary electrons from ionization electrons
γ	electron emission coefficient from cathode surface
ϵ_0	permittivity of free space
E	electric field intensity position dependent
E_0	electric field intensity position independent
φ	phase angle between maximum voltage and current

Abstract of Dissertation Presented to the Graduate School
of the University of Florida in Partial Fulfillment of the
Requirements for the Degree of Doctor of Philosophy

Pulsed Glow Discharge Mass Spectrometry

By

Jeffrey A. Kingler

August 1991

Chairman: Willard W. Harrison
Major Department: Chemistry

Glow discharge mass spectrometry is accepted as an effective technique for trace elemental analysis of solid materials. The most common application of the glow discharge is to use a continuous, steady-state plasma to atomize and ionize the sample. The focus of this dissertation is the use of an alternate technique whereby the discharge is periodically terminated and the ion signal in the mass spectrometer is recorded. Pulsing of the discharge creates time-dependent ion signals that have been useful for both fundamental studies and analytical applications. The initiation period of the pulsed discharge is controlled by the rapidly changing energy of electrons emitted by the sample surface. These electrons influence the average temperature of electrons in the plasma and affect the ionization of species with high ionization energies. A pulsed discharge that has reached equilibrium behaves much the same as a steady state d.c.

discharge. This equilibrium is disrupted again at the termination of the discharge pulse. Electrons rapidly thermalize at the end of the pulse cycle, and metastable species dominate ionization (Penning ionization). Penning ionization allows mass spectra to be accumulated that discriminate against species with ionization energies higher than the metastable energy level.

Operating two pulsed glow discharges in the same chamber using pulse techniques was also examined. Alternately pulsing two samples allows their mass spectra to be compared directly. The application of the pulsed discharge eliminates the need for sensitivity factors and results indicate that an accuracy approximately $\pm 1\%$ can be expected when comparing a standard and an unknown. Radio frequency discharges were also investigated. Operating the r.f. discharge at lower frequencies (around 1 to 3 MHz) and pressures below 1 Torr increases the resulting d.c. bias voltage for a given amount of input power. Experiments were conducted pulsing the r.f. discharge. The r.f. system proved to be dependent on factors such as in-line capacitive coupling and discharge pressure. Nevertheless, it is possible to obtain many of the same features with the pulsed r.f. discharge as those obtained with the pulsed d.c. discharge.

CHAPTER 1 GLOW DISCHARGE MASS SPECTROMETRY

Gaseous Discharges

Introduction

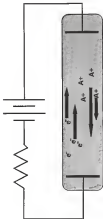
Glow discharge mass spectrometry (GDMS) is a technique for analyzing trace elemental components of solid materials. Originally developed as an alternative to spark source mass spectrometry, GDMS has evolved from a novelty in academic laboratories to a workhorse tool for analytical chemists interested in the analysis of solid samples.

The success of GDMS is based on the atomization and ionization properties of an electric circuit through a gaseous medium. The glow discharge is just one example of a gaseous discharge. Simple in appearance and easy to generate, glow discharges are actually very complex and poorly understood. The work reported in this dissertation focuses on improving our understanding of glow discharges while trying to achieve the glow discharge's reputation as an atomization and ionization source for mass spectrometric analysis.

Gaseous Conductors

Figure 1 is an illustration of a simple gas discharge tube. Gaseous discharges are classified according to the amount of current passing through the

Figure 1. Simple illustration of a gas discharge tube. Electrons (e^-) flow away from the cathode toward the anode, while ions (M^{+}) move in the opposite direction.



system. Plotted in Figure 2 (1) is the relationship between current and voltage. Three general categories of gaseous discharges are recognized (2, p. 2): 1) Townsend discharges characterized by currents less than 10^{-6} amperes (3); 2) glow discharges with currents between 10^{-6} to 10^{-1} A, and 3) arc discharges carrying currents greater than 10^{-1} A.

A Townsend discharge is a very low current discharge that is unable to sustain itself at less than 10^{-12} A without an outside source of electrons. Glow discharges become self-sustaining when a sufficient number of electrons are available to propagate additional electron production. The actual current at which a discharge is self-sustaining is a function of the number of secondary electrons (γ) liberated by discharge gas atoms ionized by electrons passing from the cathode to the anode, the distance between the electrodes (d), and the total number of electrons emitted from the cathode (y) as ions accelerated by the electric field outside with the cathode surface. The current at which the discharge is self-sustaining is called the breakdown point. This occurs when (2, p. 140):

$$y(\exp(\gamma d) - 1) = 1 \quad (2)$$

The Townsend discharge is also referred to as a 'dark discharge' (2, p. 3) because even when the discharge is self-sustaining at current greater than 10^{-6} , the electron density is insufficient to create a visible glow between the electrodes.

In an inhomogeneous electric field, increasing the discharge current transforms the Townsend discharge into a narrow, streamer-like discharge called

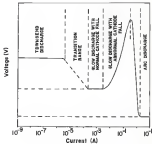


Figure 2 The relationship between voltage and current in a gaseous discharge
76

a corona. The corona is a self-sustaining discharge resulting from uneven current conduction between the cathode and anode (4, p. 141). Corona discharges are most often observed near atmospheric pressure when using unmatched electrodes (e.g., a wire cathode and a planar anode) and are often a prelude to the formation of an arc between the electrodes.

At low pressures (between 10^{-2} and 1 Torr), increasing the current from 10^{-6} to 10^{-4} A converts the Townsend discharge to a glow discharge. At this point, the electron density is sufficient to produce abundant ionizing collisions. The glow discharge region of Figure 2 is divided into normal and abnormal discharges. In a normal glow discharge, the current can be increased without a corresponding increase in voltage; the higher current is accommodated by the discharge expanding to cover a larger portion of the cathode surface area (5, p. 212). Once the entire cathode is in contact with the discharge, further increases in current require a corresponding increase in voltage, whereupon the discharge is defined as an abnormal discharge (5, p. 212).

The voltage and current in an abnormal discharge can increase up to the point when the electron density in the discharge gas allows the medium to become momentarily conducting. The sudden loss of resistance results in a high current arc or spark to form between the cathode and anode that will extinguish the negative glow and reduce the potential across the electrodes to zero. The flow of current in an arc is often intense enough to ablate material off of the cathode surface.

Glow discharges have become an important technique for solid sample analysis because they produce a steady-state population of analyte atoms (3). One common analytical application of the glow discharge is as an emission source in atomic spectroscopy (7). In the late 1950s, it was suggested that the glow discharge could be used as an analyte reservoir for atomic absorption analysis (8) though it was not until the mid 1980s that this application became popular (9). Because both excitation and ionization of analyte atoms readily occur in the glow discharge, it is well suited for mass spectrometric analysis of the trace components of solid materials (10,11).

Glow Discharges

The work in this dissertation centers around abnormal glow discharges. This type of discharge is created by applying a negative potential (500 to -5000 V) between two electrodes submerged in an envelope of air with gas (typically argon at a pressure near 1 Torr). Usually the anode is tied to ground while the negative voltage is applied to the cathode. The potential difference across the electrodes induces a flow of electrons that interacts with the discharge gas to create ions and form several different layers of luminosity. Figure 3 is an illustration of some of the different layers of luminosity, electric field strength, and current density that form between the anode and cathode of the electric circuit. These layers can be broken down into four general regions: the cathode fall, the negative glow, the positive column, and the anode fall.

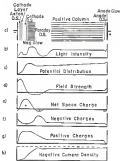


Figure 3 Layers of luminosity, electric fields, and current density in the glow discharge (12).

The cathode fall region appears as a dark boundary surrounding the cathode and is composed of several layers (10, p. 213). Closest to the cathode is the Aston dark space, a transition region where electrons emitted from the sample surface build up a space charge just above the cathode surface (8, p. 212). The Aston dark space is rarely observed because it is covered by a brighter layer called the cathode glow region. The cathode glow results from the neutralization of incoming ions drawn to the cathode surface by the electric field, releasing excitation energy (8, p. 212). The cathode glow is so close to the negative electrode that it appears as a very thin "coating." In a typical argon glow discharge, this coating appears white, whereas if water is present in the discharge it is scarlet red. Beyond the two narrow layers just described, the cathode fall region appears as a nonluminous void called the dark space (also known as the Crookes or Hilbert dark space (4, p. 213)) extending several millimeters from the cathode.

The electric field created by the applied voltage at the cathode is not distributed homogeneously between the electrodes but is instead confined to the dark space (10), leaving the remainder of the discharge almost field free. The dark space is "dark" because the electrons are accelerated to velocities whereby they cannot efficiently excite the discharge gas (14). This confined electric field is responsible for the energetic bombardment of the cathode surface by ions entering the cathode-fall region. This ion bombardment sputters cathode material off of the surface and initiates electron emission, illustrated in Figure-1. Electrons

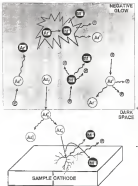


Figure 4. Simplified diagram illustrating sputtering and ionization in the glow discharge.

emitted from the cathode are accelerated by the electric field into the negative glow region. Their effect on ionization will be discussed later in this chapter.

The electric field terminates at the boundary between the dark space and the negative glow. This is determined by the point in the discharge where the flux of electrons exiting the dark space can be balanced by the flux of ions entering it. Hence, the length of the dark space depends primarily on the pressure of the discharge gas, as higher pressures provide for an increase in the number of ions available to enter the dark space. For a given discharge gas, the product of the length of the cathode dark space (δ) and the pressure (p) is such that $\delta(p) = \text{constant}$. Increasing the gas pressure reduces the length of the dark space and vice versa [5].

The electric field is usually modeled to decrease gradually from its highest value at the cathode surface to zero at the edge of the dark space where the ion and electron densities become equal [15, p. 66]. It is important to realize that electrons are rapidly exiting the dark space while ions are entering it. Because electrons are more mobile than ions, a positive space charge exists in the dark space due to the rapid electron depletion. In order to balance the flux of ions and electrons, ions must enter the dark space at a velocity higher than provided for by random motion in the field-free negative glow. This condition is known as the Bohm sheath criterion [16, p. 263] and applies to all systems that come in contact with the glow discharge plasma. The Bohm sheath criterion states that the electric field does not decrease to zero at the boundary between the dark space

and the negative glow (see Figure 5). Indeed, a small electric field extends a short distance into the negative glow, 'injecting' ions into the positive space charge of the cathode fall region where the electric field is the strongest.

The negative glow appears as a luminous cloud surrounding the cathode and extending toward the anode. This luminosity stems from discharge gas atoms relaxing after collisional excitation by electrons passing through the negative glow region. The color of the glow is characteristic of the discharge gas: argon discharges are a light blue color whereas neon gas emits a red glow.

On the macro scale, the negative glow is a homogeneous body with a balance of positive and negative charges. On the micro scale, however, the plasma is actually a complex mixture of interacting point charges that taken as a whole average out to a neutral plasma. Any disturbance in the plasma results in a redistribution of charged particles to bring the system back to equilibrium. The distance across the plasma disturbed by a point charge is called the Debye length (D). The Debye length can be calculated by (15, p.58)

$$D = \left(\frac{kT_e}{4\pi n_e e^2} \right)^{1/2} \quad (1)$$

where k is the Boltzmann's constant, T_e is the temperature of the electrons, n_e is the number density of the electrons, and e is the charge on an electron.

The degree of ionization in the negative glow is quite small, estimated to be less than 1 % [17]. Since the region is considered to be field free, the motion

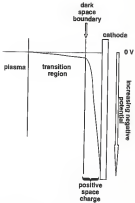


Figure 5. Illustration of the Schottky sheath structure at the boundary between the dark space and the negative glow (21, p. 107).

of charged particles is controlled by diffusion. The electric potential of the negative glow, however, is not neutral, nor is its potential between the values of the anode and cathode. Instead, the negative glow is actually the most positive component of the discharge (18, p. 80). This is another manifestation of the plasma maintaining a balanced flux of electrons exiting the plasma at the anode and ions exiting the plasma at the cathode. The flow of anodic current through the gas demands that the flux of electrons and ions be equal. The problem is that electrons are more mobile than ions and if the plasma potential were at ground the electron current would be greater than the flux of ions at the cathode. By becoming the most positive component of the discharge, the plasma acts as an electron 'sink' and slows the loss of electrons to balance the loss of ions.

Beyond the negative glow is a gradual transition to a nonluminous region called the Faraday dark space (4, p. 88). This fading-away of the negative glow is attributed to the loss of secondary electrons to excite the discharge gas atoms. Because the only electrons available in this region possess very low energy, ionization by atoms (trapped) is an excited energy state (metastable atoms) and photo-ionization from light emitted by the glow region are the only sources of ionization. The electric field in the Faraday dark space begins to reverse polarity from the negative glow and serves as a transition zone to a second luminous region called the positive column (19).

The positive column fits the actual definition of a plasma in that there is an equal number of positive and negative charges and no space charges are present.

(3, p. 147). The entire space between the Faraday dark space and the anode is occupied by the positive column, regardless of the distance separating the electrodes (15, p. 77). The purpose of the positive column is to maintain the conduction of current between the cathode and anode (3, p. 153). Because ion motion is limited to slow diffusion, electrons are the only current carriers in this region. The electric field reversal in the Faraday dark space sets the stage for a slowly increasing electric field across the positive column that imparts sufficient energy into the electrons to initiate just enough ionization to compensate for losses to the chamber walls (3, p. 147). Electrons also cause excitation of gas atoms to produce a luminous glow throughout the positive column.

The glow discharge electric circuit is complete at the anode. No ions are emitted from the anode, hence the arrival of electrons creates a negative space charge just above its surface to form an anode dark space (4, p. 346). Ions required to balance the electron flux are created by electrons accelerated across the sudden potential drop across the anode boundary (3, p. 153); this ionization forms the anode glow that appears attached to the anode surface.

The only features that are absolutely necessary to form a glow discharge are the cathode fall region and the negative glow. If the distance between the electrodes is reduced, the positive column is first consumed, then the Faraday dark space disappears—but the cathode fall and negative glow remain unchanged. The glow discharge will continue until the cathode-anode separation is approximately twice the length of the dark space (5, p. 75). In glow discharge

mass spectrometry, the electrode spacing is such that the Penning dark space is rarely observed and the positive column is never observed.

Ionization in the Glow Discharge

The ability to ionize sample atoms is one of the important features that makes the glow discharge useful for analytical applications in mass spectrometry. Almost all of the ionization occurs in the negative glow region (see Figure 4). Although ionization occurs throughout the negative glow, only ionization reactions that take place immediately in front of the exit orifice are observed by the mass spectrometer [19]. Listed in Table I are some of the ionization mechanisms thought to occur in the negative glow. Many ionization routes are possible, but only two are thought to be responsible for most of the ionization (15): electron ionization and Penning ionization.

Electron Ionization

Electron ionization occurs when an atom collides with an electron whose energy is higher than the ionization energy of the atom. There are two principal sources of electrons in the negative glow: emission from the cathode surface (called primary electrons) and ionization reactions occurring in the negative glow (called secondary electrons) (20).

TABLE I
POSSIBLE IONIZATION MECHANISMS
IN THE NEGATIVE GLOW REGION

ELECTRON IMPACT IONIZATION



PENNING IONIZATION



ASSOCIATIVE IONIZATION (HOMONUCLEAR)



ASSOCIATIVE IONIZATION (HETERONUCLEAR)



DYNALECTIC CHARGE TRANSFER

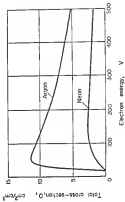


Key: M^0 , neutral analyte atom; M^+ , analyte ion; Ar^+ , argon (or discharge gas) metastable atom; Ar^0 , neutral argon atom; e , electron.

Primary electrons are emitted from the cathode surface as ions accelerated by the electric field collide with the cathode, liberating both cathode material and electrons. (In secondary ion mass spectrometry, electrons emitted by ion impact are called secondary emission electrons – a sometimes confusing difference in nomenclature.) Primary electrons are accelerated by the electric field across the dark space and enter the negative glow at high velocity. The kinetic energy of primary electrons has been measured to be equal to the entire potential dropped across the cathode fall (21), indicating that very little excitation occurs in the dark space. These electrons are certainly energetic enough to ionize atoms in the negative glow, but their velocity reduces their interaction time with the atoms, decreasing the probability of an ionizing collision (22, p. 122), (see Figure 4). Although responsible for some ionization in the discharge, a large percentage of the primary electrons transverse the negative glow and collide with the anode.

The largest population of electrons in the negative glow is secondary and ultimate electrons. Secondary electrons are the by-product of ionization reactions and their energy varies with the excess energy available after ionization. Ultimate electrons are simply secondary electrons that have undergone numerous inelastic collisions and have lost most of their energy. Both ultimate and secondary electrons have an energy distribution that approximates a Maxwell-Boltzmann distribution, though each has a different mean energy value (23, p. 122). The mean energy of secondary electrons is reported to be approximately 4 eV (22), and these electrons are responsible for most of the electron ionization in the

Figure 6: Electron cross section versus electron energy (in eV) and room [2], p. 209



negative glow region. Ultimate electrons are much lower in energy with a mean energy less than 1 eV (18) and do not play a role in ionization (24).

If the energy of an electron is insufficient to initiate its collision partner atomic excitation can occur. Sometimes an atom is excited to a forbidden energy level from which it cannot radiatively relax. Such an atom is said to be in a metastable energy state (25). In the 1920s, F. H. Penning proposed an ionization mechanism by which an atom could be excited above its ionization potential by colliding with a second atom trapped in a metastable energy state (26). Called Penning ionization, this mechanism is now recognized as playing a significant role in ionization in the negative glow.

Penning Ionization

For many years it was assumed that electron-atom/atom-dominated the glow discharge. Although Penning ionization was proposed in the 1920s, its significance to ionization in the glow discharge was not given attention until its importance was demonstrated by Coburn and Ray in 1931 (27). Since that time additional evidence has been reported confirming that Penning ionization must be considered when evaluating ionization in the glow discharge (28-30). It has been proposed that Penning is responsible for 40 to 80 % of the ionization in the discharge (30).

To understand Penning ionization, it is necessary to examine how metastable atoms are created and some of their properties. Metastable species

ionized when electrons collide with neutral particles. Listed in Table I are four pathways for metastable formation [21, p. 175]. In each case, the atom is excited to an energy level that does not have a permitted dipole moment transition trapping the atom in that energy state [22]. Without a radiative decay pathway to allow spontaneous relaxation of the atom, metastable atoms must rely on inelastic collisions that allow these excited atoms to relax by transferring their energy to their collision partner. This means metastable atoms are a reservoir of stored energy to be released upon collision. The lifetimes of metastable atoms are on the order of milliseconds [23] (in sharp contrast to electronic relaxation that occurs on a 10^{-8} s time scale). Because metastable atoms rely on collisional deactivation, it is not surprising that pressure has a large influence on the lifetime of the metastable state. Pressure above 1 Torr results in shorter metastable lifetimes as collisions occur more frequently [24]. The metastable population is also a function of electron current. According to Detorakis et al [21, p. 180], the population of metastable atoms (n_m) is related to the density of electrons (n_e), the neutral species density (n_n), a coefficient for the production rate of metastables (C_m), and the rate at which metastable atoms are lost (γ) (primarily by diffusion to the wall of the discharge chamber). At low current densities and constant pressure, there is a linear relationship between n_m and n_e , such that

$$n_m = n_e n_n C_m / \gamma \quad (2)$$

TABLE II
ARGON METASTABLE FORMATION MECHANISMS

1) EXCITATION BY ELECTRON IMPACT



2) EXCITATION TO A RADITIVE LEVEL THAT RELAXES TO A METASTABLE LEVEL



3) EXCITATION OF A PARTICLE ALREADY IN AN EXCITED STATE



4) COLLISIONAL RADIATIVE DECAY



Source: Delmon *et al.* [36] p. 135.

It is possible to reach an upper limit on metastable formation as destruction by electron impact becomes competitive with metastable formation.

Metastable atoms make an important contribution to ionization in the glow discharge because of their ability to ionize any species with an ionization energy less than the metastable energy level. Almost all of the elements in the periodic table can be ionized by Penning ionization. The exceptions, along with some common contaminant gases not ionized by the metastable atoms, are listed in Table II for neon, argon, and xenon (35).

Other Ionization Mechanisms

Although Penning and electron ionization dominate the glow discharge there are several ionization mechanisms that should also be considered.

Not all reactions involving metastable atoms yield an excited atomic species. It is also possible for heteronuclear associative-ionization to occur (36), where



In associative ionization, the resulting electron carries off any excess energy (37) allowing the reaction products to remain bonded together. The products from equation (4) are often observed in glow discharge mass spectra and can cause spectral interferences if the mass-to-charge ratio of the resulting diatomic

TABLE II
METASTABLE ENERGY LEVELS FOR SOME GAS ATOMS

Element	Metastable State ^a	Energy ^b	Species Not Ionizable ^c
He	2^1S_u 2^3S_u	23.61 eV 19.82	He, Ne
Ne	$3^1P_1^o$ $3^3P_1^o$	16.72 16.62	He, F, Ne
Ar	$4^1P_1^o$ $4^3P_1^o$	11.72 11.65	H, He, N, O, F, Ne Cl, Ar, Br, Kr, Xe H ₂ , O ₂ , OH, H ₂ O CO, CO ₂ , N ₂ O
Xe	$6^1P_1^o$ $6^3P_1^o$	9.45 9.32	H, He, C, N, O, F, Ne, P, S, Cl, Ar, As, Se, Br, Kr, I, Xe, Hg Au, H ₂ , O ₂ , OH, H ₂ O, CO, CO ₂ , N ₂ O, NO ₂

Source: a) Delcroix et al. (21, p. 132)
 b) CRC Handbook of Chemistry & Physics 1973 ed. (26, pp. B394 & B-395)
 c) Same as in (26)

molecule coincides with an analyte species. Interferences often arise when sputtering gas atoms combine with atoms sputtered off the cathode surface (e.g. FeAr^+ ions when using an iron cathode in an argon discharge) or when reactions with contaminant gases in the discharge chamber occur (e.g. ArH^+ or ArO^+).

Any reaction that yields molecular species is a source of potential isobaric interference in elemental analysis. This is true of the discharge gas when it becomes involved in a heteronuclear associative ionization to form, for example, Ar_2^+ . This reaction is very similar to heteronuclear associative ionization, but is proposed to rely on a collision with an atom in an excited radiative state rather than a metastable state (28). Discharge gas atoms do not dominate gas discharge mass spectra, but they are significant enough to render the mass-to-charge ratio they overlap completely useless for analytical purposes.

Another molecular interference often observed is the reaction of hydrogen with water vapor in the discharge chamber (29):



Small amounts of water in the discharge can form a large H_3O^+ peak at mass 33. This reaction occurs so readily that the H_3O^+ peak can be used as a reference point to determine the extent of water vapor in the discharge.

In considering additional ionization pathways in the glow-discharge, charge exchange mechanisms are often postulated to influence the observed species. Charge exchange ionization is thermodynamically possible when the discharge gas (say argon), encounters an atom with a lower ionization energy:



A recent paper suggests that this mechanism does not play a role in ionization in the negative glow region (NG) at least at the pressures used in the reported work [O 2 (a 1 5 Torr)]

Sputter Atomization

One aspect of glow discharge sputter atomization that has contributed to its popularity for solids analysis is the ease with which a sample can be converted from the bulk solid state to its atomic form. This is the result of cathodic sputtering, a process by which ions accelerated by the electric field across the cathode fall on the sample with sufficient energy to dislodge atoms from the cathode surface. The displaced atoms then diffuse into the negative glow where they are subsequently ionized. In GDMS, the cathode is fabricated from the sample to be analyzed and the dislodged atoms are the analyte of interest.

Cathodic sputtering was first observed in early glow discharge lamps as a deposition of cathode material onto the walls of the lamp (91, p. 8). Originally considered a source of contamination in the discharge plasma, sputtering is now seen as an advantageous phenomenon. Continuous sputtering of the cathode surface provides a supply of atoms into the negative glow that can be used as a source of neutral species for analysis with atomic absorption spectroscopy (8). GDMS also capitalizes on this supply of analyte atoms, but relies on ionization in the negative glow to convert neutral sample atoms to ions for mass spectrometric analysis.

Ion Bombardment Energy

Sputtering processes depend on the kinetic energy of bombarding species to dislodge atoms from the sample matrix. In GDMS, this energy comes from the electric field applied to the cathode to initiate the plasma. Discharge gas ions formed in the negative glow randomly move about the discharge space (an essentially electric field-free region) until they encounter the cathode electric field at the boundary between the dark space and the negative glow. Because the electric (static) field is dissipated across the dark space, it is possible for ions to be accelerated to energies equivalent to the applied potential. Few ions, however, actually strike the cathode surface with the energy due to collisions with neutral gas atoms, resulting in a charge exchange collision (42).

$$Ar^{+}_{fast} + Ar^{+}_{slow} \rightarrow Ar^{+}_{fast} + Ar^{+}_{slow} \quad (7)$$

This charge exchange process yields a fast neutral species that retains much of its original kinetic energy and a slow moving ion that must be accelerated by the electric field from essentially zero velocity. The velocity with which the ion finally strikes the cathode surface depends on how many collisions it experiences and how much of the electric field it is allowed to accelerate through. Hence, ion acceleration is not a simple "free fall" through the dark space and there is a distribution of ion energies colliding with the cathode surface. Factors that influence this distribution include the pressure, applied voltage, and length of the dark space.

In order to appreciate the significance of the charge exchange process, it is necessary to review the concept of the mean free path (λ_{fp}). The λ_{fp} is the average distance an atom or ion travels through the plasma before colliding with a discharge gas atom. Both the radius (r) of atoms involved in the collisions and the number density (n_g) at a given pressure are used to calculate the λ_{fp} . As an atom passes through a gaseous medium, it sweeps out a volume of space based on its velocity and radius. Within this "collision volume" is a specific number of discharge gas atoms that are assumed to be evenly distributed and stationary. The radius for an argon atom is approximately 1.7 \AA . Since the discharge gas is also argon, a collision will occur if two argon atoms are separated by less than $3r$, so that the collision radius is 3.4 \AA . At 1 Torr, n_g is 3.64×10^{18} atoms/cm³

(therefore each gas atom occupies $(2.65 \times 10^{-28} \text{ cm}^3)$). The nfp can then be calculated

$$\text{nfp} = \text{volume of each gas atom} / \text{collision volume}$$

$$\text{nfp} = r_0^{-3} / (n \cdot (4r)^2) \quad (4)$$

Using the above values for r and n_0 , the nfp of an argon atom at 1 Torr is 0.0078 ions. If the mean velocity of argon atoms in a glow discharge is $4.8 \times 10^5 \text{ cm sec}^{-1}$ (18, p. 33), then at 1 Torr, 4.8×10^5 collisions can occur per second. At 1 Torr the dark space is typically 0.3 cm deep, meaning 38 collisions can occur before an ion reaches the cathode surface (and with each collision, a charge exchange reaction can occur)

Owen and Wanderslow have developed a simple model for calculating the impact energies of ions at the cathode surface (43). In their model, the following assumptions are made

- 1) Ions enter the dark space from the negative glow
- 2) When an ion collides with an atom, the ion formed in the charge transfer process must begin its acceleration in the electric field from zero velocity
- 3) The probability of a collision does not change with energy
- 4) The electric field increases linearly from the negative glow boundary to the cathode surface

From Davis and Vandenberg's model, the probability that an ion will be accelerated through the dark space from a given distance away from the cathode surface without colliding with another ion is calculated as

$$N_0 = \exp (-x/l \ln p) \quad (9)$$

where N_0 is the probability of an ion reaching the surface without additional collisions and x is the distance between the ion and the cathode surface. The energy with which a collisionless ion can strike the cathode surface is calculated based on its position in the dark space

$$V_0 = [(2\phi_0 - \phi_0^2/l^2)] V_{\text{app}} \quad (10)$$

where V_0 is the voltage through which the ion is accelerated, V_{app} is the total applied voltage, and l is the length of the dark space. Figure 7 is a plot of the distribution of ion energies based on the above equations.

It is also possible to estimate the average energy of ions impacting the surface by incrementally calculating the number of ions that survive without further collisions from a given distance across the dark space, subtracting that number from the total number entering the dark space over a period of time, then repeating the calculations again using the remaining ions from a point slightly closer to the cathode surface. Listed in the Appendix is a BASIC computer

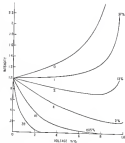


Figure 7. Calculated ion energy distribution at the cathode. The x-axis is the equivalent acceleration voltage as a fraction of the potential across the disk space (K). The y-axis is a relative population of ions arriving at the cathode. The number of collisions in the disk space used in the calculation is indicated below each line and the percentage of ions arriving without any collisions is indicated at the end of each line (AR).

program written to perform these calculations. Summarized in Table IV are the average impact energies for ions at various pressures and applied voltages using this program. As indicated in the table, ions collide with the cathode at energy values typically less than 20 % of the applied voltage.

The Davis and Vandenberg model does not take into consideration the effect of neutral particles colliding with the cathode surface. After a charge-exchange reaction, the neutral atom often retains most (if not all) of its kinetic energy and can contribute to sample sputtering. When the gap is very much smaller than the distance across the dark space, neutral species can make significant contribution to the overall sputtering [44]. These neutral species help sustain the sputtering process even though the ion energy is attenuated by collisions across the dark space [42]. It should be noted that the current measured in the discharge circuit actually represents the number of ions striking the surface. It is not possible to determine directly the contribution neutral species make to the total amount of sputtering. Systems that rely on the ion current as a measure of the number of bombarding species should be taken as only an estimated value.

Electron Scattering

When an ion strikes the surface of a solid, it transfers its kinetic energy into the matrix of the sample. The largest portion of this energy goes into sample

TABLE IV
AVERAGE ENERGY OF IONS STRIKING THE CATHODE
CALCULATED USING TONIMPACT™ PROGRAM

pressure	dark space	mfp	voltage ^a	average acceleration voltage ^b
1.5 Torr	0.22 cm	0.007 cm	-500 V	-111 V
1.3 Torr	0.24 cm	0.008 cm	-600 V	-161 V
1.2 Torr	0.28 cm	0.010 cm	-800 V	-241 V
1.0 Torr	0.33 cm	0.011 cm	-975 V	-321 V
0.86 Torr	0.36 cm	0.013 cm	-1100 V	-391 V
0.72 Torr	0.43 cm	0.015 cm	-1300 V	-552 V
0.55 Torr	0.60 cm	0.020 cm	-1545 V	-750 V

^aVoltage required to maintain 1 mA of current using a 2 mm diameter pin with 3 mm exposed to the discharge.

^bEquivalent acceleration voltage after collisions

heating, but some energy is taken-up as a rearrangement of the solid lattice structure (45). The kinetic energy can also supply enough energy into the sample matrix to dislodge (sputter) one or more atoms from the sample surface. Once free of the sample, the sputtered atom can diffuse away from the cathode and into the discharge space. How efficiently the bombarding ion sputters material off the cathode depends on factors such as the nature and make-up of the sample matrix, impact energy, and the density of the bombarding species.

Sputter efficiency is often characterized by sputter yield (\hat{A}), that is (41, p. 2)

$$\hat{A} = \text{atoms liberated / bombarding particle} \quad (51)$$

In order to get an accurate value for \hat{A} , the energy of the bombarding particle must be known. Because the glow discharge operates at pressures that yield a distribution of bombarding ion energies, sputter yield studies are usually conducted using ion-beams at pressures lower than those capable of sustaining d.c. glow discharges (10^{-4} Torr) (46). These studies are, nevertheless, regarded as an accurate representation of the sputtering that occurs in the glow discharge. As seen in Figure-8, sputter yields increase with ion energy, but the relationship is not linear and the value of \hat{A} differs among sputtered elements.

The minimum kinetic energy required to dislodge an atom from its matrix is approximately four times the material's heat of sublimation (47, p. 18). Above

Figure 8: Double field with monodromy for various models (left)

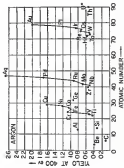


this value the sputter yield rapidly increases with energy, reaches a plateau, then decreases with further increases in impact energy. When an ion collides with the sample surface, it becomes imbedded into the sample matrix and its kinetic energy is taken up by atoms in the immediate vicinity. At low impact energies, the penetration is limited to the surface of the sample where “displaced” atoms can be ejected from the matrix. As the impact energy increases, so does the penetration of the impacting ion into the substrate, resulting in matrix damage to areas inside the sample that are too far away to affect the surface atoms, thereby reducing the sputter yield.

The ability of the impacting ion to transfer energy into the sample matrix depends on how closely matched the mass of the bombarding atom is to the mass of the atoms making up the sample matrix (46). The situation is analogous to two marbles colliding; the energy transfer efficiency between the marbles increases as the mass of the marbles becomes more closely matched. Energy transfer efficiency is an important consideration when selecting the discharge gas. When sputtering alloyed metals (which are primarily composed of transition elements), the highest sputter yields are obtained using a gas such as argon because of the relatively good match between the mass of argon and most of the transition metals. A recent sputter yield study has verified the superior sputtering qualities of argon compared to other inert sputtering gases (47).

The sputter yield also varies with the electronic structure of the elements across the periodic table. This general pattern is illustrated in Figure 5. The

Figure 9: Variations in spider yield across the periods table [44]



origin of this phenomenon is thought to be due to the d-shell of the atoms becoming fully-occupied [46]. As the d-shell becomes more complete, an atom more accurately modeled as a hard sphere [30]. When a bombarding atom such as argon (just a "hard sphere" with a complete electronic structure) strikes the surface of the sample, materials made up of elements such as copper and silver allow efficient transmission of kinetic energy to the surface of the material improving the sputter yield (see Figure 3). Elements such as titanium or molybdenum (with incomplete d-shells) are less efficient at transferring energy, resulting in lower sputter yields. It should be noted, however, that even with different sputter efficiencies across the periodic table, sputter yields do not vary more than a factor of three between elements.

Sputter etching inevitably damages the sample surface. Sometimes referred to as an etching process, the removal of atoms from the sample surface is not a simple, homogeneous process. To begin with, sputter efficiency varies depending on the impact angle of the bombarding species [31]. The sputter efficiency is highest when ions strike at angles closer to the sample surface (that is, at greater angles with respect to normal) because the ions do not penetrate as deeply into the matrix, dissipating their kinetic energy at the surface rather than inside the sample. For argon, the maximum sputter yield occurs at incidence angles between 40° to 70° from normal (at greater angles the incoming atoms bounce off the surface) [34]. Grain structure variations (e.g., crystalline grain boundaries) sputter at a different rate than other areas of the bulk material [47]

p. 18), altering the surface contours. Anisotropic structures may also sputter unevenly as elements with different sputter yields form crevices or undulations in the sample surface (32). Ions that approach the sample at angles yielding the best sputter yields tend to carve out features that favor this angle (33, p. 18). In addition, atoms sputtered between irregularities on the surface risk rapid redeposition onto the surface features, further roughening the surface. The end result is a surface resembling a field of tightly packed cones. These microscopic features are observable after bombardment with 10^{17} ions cm^{-2} onto the surface and macroscopic features can be seen with as few as 10^{16} ions cm^{-2} (34). Fortunately, once the surface attains the roughened condition (often within several minutes of continuous sputtering), its features remain relatively unchanged, resulting in a steady state sputtering condition (35).

The surface conditions just described require magnification (2000X) to be observed. One surface feature much easier to see is the formation of large surface cones or spires protruding from the sample surface (36). Large wires probably form at sites with lower sputter yields than the surrounding bulk (37) due to precipitates or faults in the bulk material or on the surface. It is also thought that difficult to sputter species can migrate across the surface (surface layer) and aggregate at a point of low sputter yield, helping the growth of the cones (37). Once formed, the growing cones can intercept sputtered atoms leaving the sample surface, a process that can play a significant role in expanding the size of a cone, particularly at its base (34).

Maintaining the Glow Discharge

There are several different methods to apply the high voltage that initiates and maintains the glow discharge. The two most significant techniques are direct current (d.c.) discharges and radio frequency (r.f.) discharges. Each of these methods has unique characteristics that make it useful as an ionization/excitation source for mass spectrometry.

Direct Current Discharges

The d.c. discharge is the most commonly used glow-discharge system in mass spectrometry. One reason for this popularity is the ease with which a d.c. discharge can be created using a conducting sample. The surrounding discharge housing serves as the grounded circuit anode, and a negative voltage is applied to the sample (application of a positive voltage would result in the discharge etching/sputtering instead of the sample). A key point of the d.c. system is that it is a steady-state discharge. That is, the system relies on the steady flow of ions toward the cathode and electrons toward the anode.

Many of the properties of the glow discharge are tied to the interplay of three parameters: voltage, current, and pressure. Pressure determines characteristics such as the Debye length, mean free path, diffusion rate, and dark space dimensions and is almost always set to a predetermined value for an experiment (usually between 0.3 to 1.5 Torr). The applied voltage determines the energy with which ions bombard the sample surface and the current is a measure

of the number of ions striking the surface. Illustrated in Figure 10 is the relationship between voltage, current, and pressure.

The dc discharge can be operated in either constant voltage or constant current mode. In constant voltage mode, the power supply is programmed to apply a fixed potential between the cathode and anode, supplying whatever current is necessary to maintain that voltage. This method controls the energy with which ions strike the sample surface, but the total number of ions will vary with the applied pressure. In contrast, constant current mode establishes the total number of ions arriving at the cathode in a given period of time, but their impact energy will vary as the power supply adjusts the applied voltage to maintain the specified current with changes in pressure. Some power supplies allow the total power to be set constant; however this does not allow direct control of either current or voltage.

Direct current glow discharges are well suited for the analysis of conducting materials. Figure 11 is an illustration of some of the various configurations possible with the dc glow discharge (36). The sample (cathode) can be cut into almost any convenient shape, provided that an insulating shield is used protect sample mounting hardware by confining the discharge to the cathode surface. Macor® (Corning), a machinable ceramic, is often used for shielding because it is easily fabricated into a variety of shapes, has good insulating properties, and is easily cleaned with acid or sandblasting. Figure 12 is a schematic diagram of the typical arrangement of shielding, sample holder,

Figure 10. The effect of pressure on current and voltage in the glow discharge low alloy steel jet. 2 mm in diameter with 8 mm exposed to the discharge. These data were accumulated using a

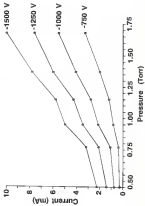


Figure 11. Various source configurations for GEMs: (a) sample pin, (b) sample disk, (c) hollow cathode, (d) screen, (e) hollow cathode plane. The sample is marked with diagonal lines and the resulting plasma is the shaded area. (50)

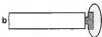
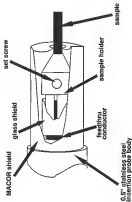


Figure 10. Sample measuring and actual configuration at the end of the expansion profile



and cathode mount used with samples cut into pin shapes. To prevent arcing as the shield becomes coated with re-deposition products from the sample, the resulting shield must cover the mounting hardware without touching the cathode. The space between the shield and the cathode must be no wider than the length of the dark space to prevent a discharge from forming behind the shield [15, p. 185]. The relationship between the sample and insertion probe, discharge housing, and the mass spectrometer is shown in Figure 13.

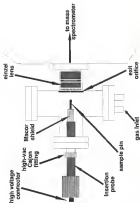
The following parameters are the minimum requirements to use a d.c. discharge as an atomization and ionization source in mass spectrometry:

- 1) The sample must be conducting in order to complete the electric circuit.
- 2) The pressure in the discharge chamber must be greater than 0.3 Torr to provide sufficient electron and ion density to maintain the discharge.
- 3) Sputtering must be confined to the sample cathode so that ions sampled by the mass spectrometer are representative of the analyte.
- 4) The power supply must be able to deliver at least -300 V when operating the discharge at 1 liter argon in order to create enough ionization to initiate the discharge.
- 5) The sputtering gas must be free of contaminants that can create isobaric interferences in the mass spectrum and free of water vapor that can significantly reduce sputtering and interfere with ionization mechanisms.

Radio-Frequency Discharges

Then, if glow discharge is more complicated than its d.c. counterpart, both in theory of operation and application to the analysis of solid samples. Although

Figure 10 Relationship between the criterion (probe) and the mass spectrometric data



r.f. sputtering systems have been used in other applications of the glow discharge [64], it was not until the early 1970s that Oosumi and Hay demonstrated its use as an ion source for mass spectrometry [65]. One important reason to consider r.f. glow discharges as an ionisation source is its ability to sputter both conducting and nonconducting samples.

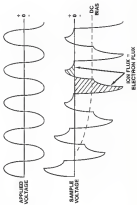
The underlying difference between d.c. and r.f. discharges is that the applied voltage in an r.f. system oscillates above and below ground potential, whereas in the d.c. system the applied voltage is continuously below ground. If an r.f. voltage is applied to a conducting sample, the oscillating electric field will alternate between sputtering the sample and the discharge housing. When the discharge housing is tied to ground, the sample acts as the cathode during the negative portion of the applied voltage and as the anode during the positive portion. In such a system, a stable discharge is never established and effective sample sputtering cannot occur.

The situation is different if a nonconducting sample is used. As an insulating sample experiences the positive portion of an oscillating electric field, it acts as a capacitor and its surface develops a positive charge. Electrons in the discharge quickly bombard the surface to neutralise the built-up charge. When the polarity of the applied voltage changes and a negative potential is applied, positive ions are drawn to the surface to neutralise the charge. Because ions are not as mobile as electrons, the neutralisation process is relatively slow. Before enough ions can arrive at the surface to neutralise the negative charge, the

polarity of the applied field changes again, leaving a residual negative charge on the sample surface. This residual charge must be overcome before the sample can develop a positive charge during the next electric field cycle. As this process is repeated, the residual negative charge increases until an equilibrium is established whereby an equal number of positive ions arrive at the driven electrode (sample) during the negative portion of the oscillating voltage as electrons during the positive portion [35, p. 144]. This process is illustrated in Figure 14. The mobility of the positive ions is slow enough that they do not separate themselves in the electric field, but rather "see" the average value of the negative field in Figure 14 (37). This average field is called the d.c. bias and it determines the energy with which ions bombard the sample surface in an rf discharge.

The d.c. bias that develops on the sample electrode is influenced by the amplitude of the applied voltage and the geometry of the electrodes in the discharge system [38]. In the rf discharge, both the driven electrode (the sample) and the grounded housing can be bombarded by discharge gas ions (unless a d.c. discharge where only the cathode is bombarded)[39]. When the electrodes are the same size, there is equal bombardment on both the grounded and driven surfaces (this is analogous to using a vibrating sample whose role alternates between anode and cathode) [40]. As the electrode becomes asymmetric, the electric field across the dark space (sometimes called the sheath potential) at the smaller electrode must increase in order to maintain the same

Figure 14. Formulation of the d.c. bias voltage as an r.f. discharge (adapted from [20]).



flow of current that the larger electrode experiences. This phenomenon was first reported by Koenig and Michael (50) who proposed that the sheath potential varied as the reciprocal of the ratio between the electrode surface areas, raised to the fourth power. Other researchers have since determined that the effect is closer to a simple reciprocal relationship (51,52). As the electrodes become more asymmetric, the d.c. bias is more closely approximated as half of the peak-to-peak applied voltage (53).

Radio frequency discharges can operate at much lower pressures than d.c. systems. As with d.c. discharges, secondary and ultimate electrons are the most abundant types of electrons in the r.f. plasma. The key difference is that rather than moving randomly in the discharge space, these electrons couple with the electric field (54), gaining enough energy to ionize discharge gas atoms. Beginning around 50 MHz, the minimum pressure at which a discharge will operate begins to decrease with increasing r.f. frequency (55). At several MHz, the minimum operating pressure is in the range of a trillion. Any frequency in the low MHz range will efficiently drive the glow discharge, though the formation of the d.c. bias may be less than optimal below 1 MHz because ions can still respond to the applied field (56). Most r.f. OCMOS power supplies operate at 13.56 MHz as this is the frequency assigned to sputtering systems by the Federal Communications Commission (FCC, vol. 19, p.155).

Despite the differences between d.c. and r.f. discharges, the general model of the glow discharge laid out at the beginning of this chapter is accurate,

provided that most of the potential difference between the driven electrode and the plasma is dissipated across the cathode dark space (32). This occurs whenever the rf discharge is operated below the electron response frequency of 500 MHz (34).

Sputtering in the rf discharge is not limited to nonconducting materials. It is possible to use conducting materials if the sample is isolated from the power supply by placing a capacitor in series between the discharge and the rf amplifier (35). This allows the conductor to simulate the properties of a nonconducting sample and the d.c. bias to form on the sample surface.

The following parameters are recommended for using rf-GCMS for sample analysis:

- 1) The sample must be nonconductive. If conducting, it must be isolated from the rf amplifier to simulate a nonconductor.
- 2) To achieve the optimum d.c. bias voltage, the sample must be the driven electrode and smaller in size than the surrounding electrode.
- 3) The operating frequency should be at least in the low MHz range.

Academic Applications

Glow discharge mass spectrometry is a trace elemental analysis technique that allows direct analysis of solid materials. Because the sample to be analyzed is the sputtered cathode in the discharge electric circuit, there are none of the problems usually associated with solution based analytical methods (i.e., contamination by reagents, dilution of trace components, and incomplete sample

discharge). The sample is converted to its atomic form by the sputtering process that occurs in the negative glow for analysis with the mass spectrometer. The glow discharge uses compact, low-power atomic-ionization source that provides a reservoir of analyte atoms with good reproducibility, sub parts per million detection limits, and a dynamic range of six orders-of-magnitude [56, 60].

Internal Calibration

In order for GDMS to be analytically useful, some correlation between the intensity of the observed spectra and the analyte concentrations must be determined. Calibration techniques usually involve the determination of sensitivity factors (SF), whereby

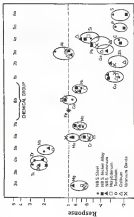
$$SF = (\text{observed intensity})/(\text{certified concentration}) \quad (12)$$

The observed intensity is based on the peak height or total area of individual isotopes in the mass spectrum.

One technique using sensitivity factors is a process called internal calibration (IC). This method assumes the sample (typically a low alloy steel) is composed of only the base matrix (e.g., iron). The natural abundance of iron is ^{54}Fe , 5.8%; ^{56}Fe , 91.7%; ^{57}Fe , 2.14%; ^{58}Fe , 0.31%. An isotope such as ^{57}Fe (which rarely experiences isotopic interferences) is selected and a SF determined by

assuming that the concentration is the isotope's natural abundance times 1.0×10^5 parts-per-million (ppm) (e.g., 21,400 ppm ^{54}Fe). If the peak height of the ^{54}Fe peak is 300,000 counts in the area spectrum, then the SF for iron would be 30 counts/ppm. Internal calibration assumes that all elements have the same SF as iron. This assumption is surprisingly accurate because the sensitivity factors for most elements, relative to iron, have been reported to vary by no more than a factor of three [66,68] as illustrated in Figure 15. The SF for iron is then multiplied by the observed peak area/area for isotopes of the element of interest and the concentration determined taking into account the natural abundance of the isotope measured. Internal calibration is a fast survey method, useful for identifying the type of steel or simulating, does not identify between a number of possibilities. The technique is limited in that the SF applies only to the particular sample currently being analyzed and the intensities of the isotopes must be determined with the same instrument parameters and detector sensitivity as those used with the iron determination. Furthermore, the detection limits for internal calibration are limited to the low ppm because the matrix SF must be determined with detector sensitivities that do not overload the detector as the iron peaks are scanned. For sub-ppm detection limits and improved accuracy, a different analytical method is employed.

Figure 13. Ion pairs relative to water (M)



Relative Sensitivity Factors

To take into consideration the many variables that can affect the observed signal intensity between different samples and separate analysis runs on a given instrument, a more "refined" application-technique called relative sensitivity factors (RSFs) - Originally developed for spark source mass spectrometry (SS), this technique has been successfully adapted to GDMS (76 - 78).

The relative sensitivity factor is defined as (76):

$$RSF = (SF \text{ of analyte}) / (SF \text{ of internal standard})$$

or

$$RSF = (I_A/C_A)/(I_R/C_R) \quad (10)$$

where I_A is the intensity of the analyte peak, I_R is the intensity of the reference peak (typically ^{57}Fe), C_A is the concentration of the analyte, and C_R is the concentration of the reference element. The reference element serves as an internal normalization factor to compensate for differences in tuning, detector sensitivity, and other parameters that affect the ion signal intensity.

An important advantage with RSFs is that they do not vary appreciably between different matrices. A recent analysis (79) of 52 elements in six different matrices indicates that there is little difference between the relative standard deviation (RSD) of RSFs determined in different matrices (about 13 %) and the RSD of the RSF values between elements in a given matrix (about 11 %). This

independence from the sample matrix means that it is not necessary to match the composition of the standard with the composition of the unknown. This can be a significant advantage as matching standards may not be available for specific elements or at the desired concentration range.

Actual sample analysis entails development of a calibration curve for one or more elements using certified standards. If RSPs have been calculated, it is not necessary to determine a calibration curve for every element to be analysed, as long as the internal standard used in the RSPs is determined. Once the calibration curve is established, the following linear relationship can be used to determine the concentration of elements in the sample [6]:

$$I_A = (RSP) (C_A/C_i) + b \quad [14]$$

where b is the intercept of the calibration line and the RSP is the slope of the line (6). In the absence of spectral interferences, $b = 0$ (7) and equation (14) is simply a rearranged version of (1). Sawyer et al. (7) have conducted GDMS analyses using calibration curves and RSPs developed from the analysis of six National Institute of Science and Technology (NIST) standards using ^{235}U as the internal standard. Analysis of a seventh NIST standard yielded calculated values to within an average of 5 % of the certified value.

Analytical Properties of the Glow Discharge

Several assumptions are made when GDMS is applied to the analysis of a solid sample. First, the sample matrix does not significantly affect the RFPS; second, the observed ion signal is representative of the bulk concentration of the analyte; and third, the isotope used to determine the concentration of an element does not have an overlapping interference at the same mass-to-charge ratio. It is worthwhile to examine why these are reasonable assumptions.

Although sample sputterion and ionization occur in the same discharge chamber, each step is actually separate, occurring at different times and at different locations in the glow discharge (75). This property allows these two steps to be treated individually when analyzing the glow discharge.

Removal of analyte atoms from the sample matrix by sputtering was discussed earlier in this chapter. The important point to remember here is that sputter ionization is a surface phenomenon and is representative of the composition of the bulk material only when the solid is homogeneous. After an atom is dislodged from the sample matrix and enters the discharge region, it loses all "memory" of its condition before sputtering. This means that GDMS does not yield any information about the molecular structure of the sample. It also means the matrix cannot interfere with atoms once they are free of the sample thereby removing matrix interferences. This is why RFPS do not vary significantly between different sample matrices (76).

As indicated in Figures 8 and 9, different elements do not have the same sputter yields and there is a pattern to sputter yields based on the element's electronic structure. If sputter yields are different, then how can sputtering result in an atomic population that is representative of the composition of the bulk material? In the initial stages of sputtering, the atomic population does not accurately represent the bulk material. But as sputtering continues, elements with higher sputter yields are depleted from the sample's surface. Eventually, as steady state is reached whereby differences in sputter yields are compensated for by the availability of each element to be sputtered (42). Sputtering at equilibrium yields an atomic population with the same relative sizes as the bulk sample provided elements do not migrate or diffuse from inside the sample to the surface (an unlikely event unless the sample becomes very hot).

Once the sputtered atoms are in the negative glow region, ionization determines whether an accurate representation of the sample can be obtained. There does not appear to be any preferential ionization occurring in the negative glow. Evidence for this comes from simultaneous atomic absorption/mass spectrometric analysis of ion cathodes (18) in which changes in total current and pressure resulted in proportional changes in both the atomic absorption signal of the neutral species and the ion signals observed with the mass spectrometer.

Isobaric interferences (the overlapping of two or more species with the same mass-to-charge ratio) can be a problem in quantitative analyses using GDMS. The source of these interferences is almost always the formation of

molecular species in the discharge. Table V (77) is a list of some common molecular interferences (78). The problem is aggravated by the quadrupole mass spectrometer's low resolution which cannot separate the sub-mass differences between the analyte and the interferent. The presence of isobaric interferences is identifiable by examining the isotopic ratio of the element of interest. If the ratios are incorrect, a molecular interferent is most likely responsible. The resulting interferent will have an easily recognized isotope pattern if one of the atoms in a heteronuclear diatomic interferent has a single dominant isotope (e.g. ArFe^+ has the same pattern as Fe^+ except the mass range is extended by 40 amu.) Molecular interferences with numerous possible isotopic combinations create complicated patterns in the mass spectrum, but these too can be predicted using statistical methods (79, p. 184). Another source of interference, though less common than molecular interferences, is the formation of multiply charged species. Because the quadrupole mass spectrometer separates ions based on their mass-to-charge ratio, doubly charged species appear in the mass spectrum at half their atomic mass. The discharge gas itself is the most common source of multiply charged interferences (e.g., $(\text{Ar})^{2+}$).

Fortunately, most elements have several isotopes in abundances suitable for quantitative analysis, so that if one isotope is covered by an interferent a second isotope is selected. As a general rule, the isotope with the lowest RRF is the least likely to have signal interference (80). Situations in which the discharge gas is the source of interference can be overcome by using an

TABLE V
POSSIBLE MOLECULAR AND MULTIPLE CHARGED INTERFERENCES

m/z	Possible Interfering Species
15	$^{15}\text{N}^+\text{H}^+$
16	$^{16}\text{O}^+\text{H}^+$
17	$^{17}\text{O}^+\text{H}^+$, $^{14}\text{N}_2^+$, $^{12}\text{CH}_3^+$
18	$^{18}\text{O}^+\text{H}^+$, $^{14}\text{N}_2^+\text{O}^+$
19	$^{19}\text{F}^+\text{H}^+$, $^{16}\text{O}^+\text{H}_2^+$, $^{14}\text{N}_2^+\text{O}^+$, $^{12}\text{CH}_3^+$
20	$^{20}\text{Ne}^+\text{H}^+$
27	$^{27}\text{Al}^+\text{H}^+\text{H}^+$
28	$^{28}\text{Si}^+\text{O}^+$, $^{14}\text{N}_2^+$
29	$^{29}\text{Si}^+\text{O}^+\text{H}^+$, $^{14}\text{N}_2^+\text{H}^+$
30	$^{30}\text{Si}^+\text{O}^+$
39	$^{39}\text{K}^+\text{H}^+$
40	$^{40}\text{Ca}^+\text{H}^+\text{O}^+$
43	$^{43}\text{Ca}^+\text{H}^+\text{O}^+\text{H}^+$
44	$^{44}\text{Ti}^+\text{O}_2^+$
46	$^{46}\text{Ti}^+\text{O}_2^+\text{H}^+$
78	$^{78}\text{Kr}^+\text{H}^+$
80	$^{80}\text{Kr}^+$
81	$^{81}\text{Kr}^+\text{H}^+$
84	$^{84}\text{Kr}^+\text{H}^+$
90	$^{90}\text{Zr}^+\text{H}^+$

alternative gas (R7) that moves such interferences to a different mass range (e.g. m/z), replacing an argon discharge with a xenon discharge will move the discharge gas interferences 20 units.

CHAPTER 2 INSTRUMENTATION

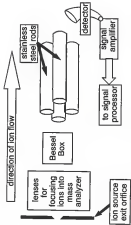
Mass Spectrometry Basics

Mass spectrometers take advantage of intrinsic properties of charged particles in order to isolate specific analyte atoms and molecules based on their mass. The work presented here was performed on a quadrupole mass spectrometer in which mass separation is based on the particle's mass-to-charge ratio (m/z).

Quadrupole Theory

The basic configuration of a quadrupole mass spectrometer is illustrated in Figure 19. At the heart of the quadrupole is four parallel stainless steel rods carefully positioned at the corners of a square. The rods are setup to operate in pairs. The trajectory of the ions as they travel down the length of the quadrupole varies with their m/z and the voltages applied to the pairs of rods. Ions with stable trajectories pass through the quadrupole and are detected by a transducer. Although the path of individual ions through the quadrupole is very complex, it is possible to develop a qualitative picture of how the ions and the applied voltages interact (20).

Figure 18. Current diagram for a quadrupole mass analyzer



When an ion enters a quadrupole mass filter, it immediately experiences the influence of the r_f and d_c potentials. A positive d_c potential is applied to the two rods lying in the $X-Z$ plane (8f) while the rods in the $Y-Z$ plane experience a negative d_c voltage, as illustrated in Figure 17. The r_f potentials applied to the pairs of rods are 100° out of phase with each other. The motion of a positive ion entering the quadrupole mass filter can be examined in each of the two planes independently (8g).

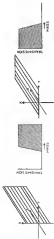
The $X-Z$ rods act as a high pass filter for positive ions (see Figure 18a). Consider the effect of the positive d_c potential in the $X-Z$ plane. Positive ions in this plane are "focused" toward the center region between the rods by the positive d_c bias. Heavier ions only respond to the positive d_c bias. Lighter ions, on the other hand, feel the effects of the r_f field and are periodically drawn away from the center region during the negative portion of the r_f duty cycle. If sufficiently displaced, these lighter ions will collide with the rods and are lost. By increasing the intensity of the r_f voltage, progressively heavier ions can be displaced by the r_f field.

The negative d_c bias in the $Y-Z$ plane has the opposite effect just described for the $X-Z$ plane. In this plane, positive ions are drawn toward the rods. The r_f field serves to correct the paths of the lighter ions, diverting them toward the center of the mass filter (8c). Increasing the r_f voltage increases the mass-to-charge ratio allowed to traverse the quadrupole. In other words, the rods in the $Y-Z$ plane act as a low pass filter (see Figure 18b).

Figure 12 Coordinates used with the quadrupole mass filter



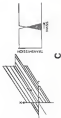
Figure 18. Mass fitting in the quark-pole. (a) K_2 plane: high-pass filter. (b) Y_2 plane: low-pass filter. (c) combined plane: band-pass filter. (d)



B



C



By combining the high-pass properties of the rods in the $X-Z$ plane with the low-pass filtering of the rods in the $Y-Z$ plane, a band-pass filter is created whereby a narrow mass range of ions are transported through the quadrupole filter (Figure 18c). Increasing the applied voltage to the rods increases the mass-to-charge ratio allowed through the band-pass.

The trajectories of ions through the quadrupole are very complex and vary with both the applied voltage and time. The time-varying potential can be expressed as [62]

$$\phi_z = U + V \cos \omega t \quad (15)$$

where ϕ_z is the electric field at some time (t), U is the d.c. voltage, V is half the peak-to-peak voltage of the r.f. field, and ω is $2\pi f$ (where f is the r.f. frequency).

Because the time-varying electric field exists in three dimensional space, Equation (15) can be expressed as

$$\phi = \phi_z (ax + by + cz) \quad (16)$$

where a , b , and c are constants, x , y , and z are the positions along the axes illustrated in Figure 18, and ϕ is the position-dependent intensity of the electric field. Basic quadrupole theory assumes that no space charges are present [63] (Chapter 2); therefore Equation (16) must conform to Laplace's equation, whereby $\nabla^2 \phi = 0$ [64, p. 30]. Because there is no z -component in the quadrupole field

$a = 0$. Therefore, to satisfy Laplace's equation $a = -b$. The value a is related to the distance from the center of the quadrupole field to the edge of the quadrupole rods (r_0), such that $a = 1/(2r_0)^2$. Integration converts the Laplacian form of Equation (16) into a meaningful representation of the electrostatic field (25, p. 10). The final form of the equation for the time and space dependent electric field in the quadrupole mass filter is (20):

$$\phi = (U + V \cos \omega t) (x^2 - y^2)/4r_0^2 \quad (17)$$

Equation (17) indicates that the quadrupole rods must be hyperbolically shaped to produce the ideal electric field. Such rods, however, are more difficult to manufacture. Fortunately, the hyperbolic field can be approximated by circular rods provided the radius of the rods is $1/148 \text{ cm}$ (20).

To calculate the intensity of the electric field (E) along the X - Z and Y - Z planes, Equation (17) must be differentiated relative to the X and Y axis (20) to yield

$$-d\phi/dx = (U + V \cos \omega t)(2x/r_0^2) \quad (18)$$

and

$$-d\phi/dy = -(U + V \cos \omega t)(2y/r_0^2) \quad (19)$$

Charge is introduced into these equations by using the definition of an electric field [44 p. 426] that is a force $\langle F \rangle$ acting upon a charge $\langle q \rangle$ ($E = F/q$). Equation (18) thus becomes

$$F_x = -\beta J + N\omega_0 \langle \mu \rangle C_0 (\omega_0 / v_0)^2 \quad (20)$$

in the xz plane. Mass $\langle m \rangle$ is introduced by considering that $F = \langle m \rangle a$ (acceleration), where acceleration is expressed as d^2x/dt^2 along the x -axis. Substituting these values for F and setting the equations equal to zero, the equations of motion in the quadrupole are [21]

$$d^2x/dt^2 + (\beta J + N\omega_0 \langle \mu \rangle C_0 (\omega_0 / v_0)^2) x = 0 \quad (21)$$

and

$$d^2y/dt^2 - (\beta J + N\omega_0 \langle \mu \rangle C_0 (\omega_0 / v_0)^2) y = 0 \quad (22)$$

Equations (21) and (22) are Mathieu type equations [45 Chapter 3]. Bounded solutions define stable ion trajectories through the quadrupole. Unbounded solutions yield unstable trajectories resulting in the ion colliding with the quadrupole rods. A graphical representation of the solutions to Equations (21) and (22) is used to ascertain the stability of an ion in the quadrupole field. The following substitutions are usually made so that the equations can be written as a single expression [46]:

(8)

$$u = \sin(\omega t) m e^2 V_0 / 2 \quad (20)$$

(19)

$$v = 2 \sin(\omega t) m e^2 V_0 / 2 \quad (21)$$

These substitutions represent the d.c. voltage (u) and the amplitude of the r.f. voltage (v) (20). The stability diagram is constructed by plotting the d.c. voltages that yield stable solutions versus the r.f. voltages that also yield stable solutions for a given mass, as illustrated in Figure 1(b). The area inside the triangular shaped region represents d.c. and r.f. voltage combinations that yield stable ion trajectories.

The quadrupole mass spectrometer controls which masses have stability trajectories by varying the d.c. and the r.f. voltage. Usually, the d.c. voltage is proportional to the r.f. voltage so that a constant ratio is maintained between the two potentials. In the stability diagram, this ratio appears as the slope of a line anchored at the origin (illustrated as a dashed line in Figure 1(b)). This line is called the mass scan line. Where the mass scan line passes through the triangular shaped stability region determines the voltage range over which an ion of a given mass-to-charge ratio has a stable trajectory. Each mass has a slightly different stability diagram. The resolution between masses is determined by how much of the stability diagram is intercepted by the mass scan line. Maximum resolution occurs at the tip of the stability region, but this also coincides with lower transmission efficiency and reduced sensitivity.

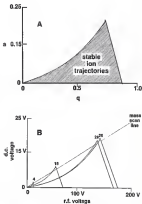


Figure 19: Mathieu stability diagrams. (a) stable trajectory region at a single m/z ratio, (b) the same diagrams at several m/z ratios (52)

Mass Analysis

The mass analyzer used in the work reported here is made-up of three components: the quadrupole mass filter, a *Bessel* box to select ions entering the mass analyzer based on their kinetic energy, and a series of electrostatic lenses to transport and focus ions into the *Bessel* box. Listed in Table VI are the specifications for the quadrupole mass filter used in these experiments.

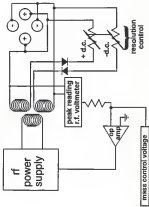
The mass-to-charge ratio passed by the quadrupole mass filter is directly proportional to the voltage applied to the rods. This voltage is controlled in much the same way an operational amplifier maintains zero voltage at its summing point as zero. As illustrated in Figure 2B, an internal operational amplifier in the mass controller "sees" a control voltage set by the operator (or computer) and then attempts to bring the summing point to zero by adjusting the amplitude of the *r.f.* voltage applied to the quadrupole rods. The negative *d.c.* voltage from the rods is first averaged, then passed through a resistor to the summing point of the op amp driving the *r.f.* power supply. Calibration of the mass spectrometer is a matter of varying the applied control voltage to the mass passed by the spectrometer. In the case of computer control, binary coded information is converted to an analog signal which is then applied to the summing point. By correlating the output mass to the binary number driving the digital-to-analog converter, it is possible to calibrate the mass spectrometer.

To maintain the constant *d.c./r.f.* mass *r.f.* voltage to the rods a rectifier to produce the positive and negative *d.c.* bias voltage, which is then applied to the

Table VI
EXTREL QUADRUPOLE MASS SPECTROMETER
SPECIFICATIONS

manufacturer	Extrel Corp. Pittsburgh, PA
model	#001-1
quadrupole rods	
material	stainless steel
length	22 cm
diameter (ex.)	1.55 cm
field diameter	0.527 cm
operating frequency	1.25 MHz
max. d.c. voltage	650 V
peak r.f. voltage	4 kv
max. r.f. power	250 watts
mass range	1-350 amu

Figure 20. Simplified schematic diagram of the hydrologic model structure

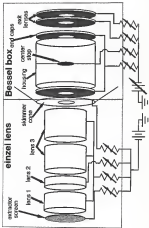


rods (see Figure 20). This insures that the d.c. voltage increases in proportion to the amplitude of the r.f. voltage. The instrument's resolution is controlled with a matched set of resistor pots that control the d.c. voltage applied to the rods, thereby altering the d.c./r.f. ratio.

Between the glow-discharge ion source and the quadrupole mass filter is a set of lenses for focusing and transporting the ions, and an energy discriminator that limits ions entering the mass spectrometer to a narrow energy range. These two electrostatic elements are illustrated in Figure 21. Ion transport is accomplished using an axial lens (37, p. 355). This multi-element lens system allows the transfer of ions from the glow discharge to the Dessel box with minimal changes in energy. Operating the lens with the center element at a higher potential than the entrance element focuses the ion beam toward the center axis down the length of the lens (37, p. 354). To improve the extraction of ions from the glow-discharge, an extractor screen is placed immediately behind the source's exit aperture to draw ions toward the first element of the axial lens.

Proper resolution between different mass-to-charge ratios requires ions to remain in the quadrupole field long enough to experience several r.f. oscillations (to eliminate unstable ions), yet not so long as to have the applied voltage change before ions can exit the mass filter (39, p. 23). Therefore, ions entering the mass filter should be limited to a narrow range of kinetic energy. This energy discrimination is accomplished with an electrostatic energy analyzer called a Dessel box (Rane Model 030-2). Figure 22 is an expanded view of the Dessel box

Figure B1 Schematic diagram of the virtual lenses and beam loss energy discriminator

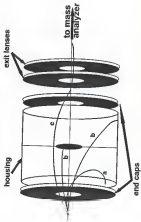


and the trajectories of ions through the analyzer (38). Ions entering the Bessel box first encounter a repelling field created by the potential between the cylindrical housing and the end caps (38). Low energy ions are turned back away from the cylinder, creating a low energy cut-off. Ions must be energetic enough to overcome the repelling field of the end caps, deflected around the centerstop by the housing potential, then reaccelerated out of the second endcap. Ions too energetic either collide with the cylinder walls or with the centerstop, providing a high energy cut-off (38). The centerstop also prevents neutral species and photons from entering the mass filter. The range of ion energies passed by the Bessel box is within 1-2 eV of the potential on the cylindrical housing (38). The Bessel box can be used to profile ion energies by sweeping the potential on the housing. In our system, however, it is not possible to determine absolute ion energies in the discharge because the extractor screen behind the exit orifice plate distorts the energy of sampled ions. The two lenses behind the Bessel box serve to control the velocity of ions entering the mass filter (i.e., the velocity along the z-axis).

Vacuum Systems

The main problem coupling a glow discharge ion source to a mass spectrometer is that differential pumping (31 p. 284) is required to reconcile the difference in pressure between the discharge (around 1 Torr) and the operating pressure of the mass filter ($< 10^{-6}$ Torr).

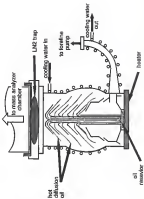
Figure 20. Schematic view of the three box energy distribution. (a) trajectory of an ion with low kinetic energy, (b) trajectory of ions with high kinetic energy, (c) trajectory of ions with kinetic energy within ± 40 of trapping potential (30).



The vacuum system for the mass spectrometer used in these studies is composed of two HPG Model DHS-4 oil diffusion pumps. An interior view of an oil diffusion pump is illustrated in Figure 30. Oil diffusion pumps operate by heating a high molecular weight oil to its boiling point. The oil evaporates up a chimney and are then directed downward towards the outer walls of the pump, creating jets of oil streaming towards the base of the pump (30, p. 418). The walls of the pump are cooled with a chilled water jacket so that oil molecules condense and flow back to the pump reservoir after colliding with the walls (30, p. 180). Atoms and molecules that arrive at the top of the pump encounter the jets of oil vapor and are deflected downward toward the lower regions of the pump, entering progressively higher pressure regions. At the base of the pump, the oil returns to the heated reservoir while gases are removed by the a rotary foreline pump.

Oil diffusion pumps provide both high vacuum and high pumping speeds. In our system, the first diffusion pump bears most of the gas load from the discharge chamber, while the second pump maintains the low pressure required for proper mass filter operation. When the discharge is operating at 1 Torr argon, the first chamber typically maintains a pressure of 1×10^{-4} Torr and the second chamber operates near 6×10^{-6} Torr. The minimum discharge pressure is limited to approximately 0.5 Torr, above which the first diffusion pump reaches its maximum operating pressure of 10⁻⁴ Torr.

Figure 20 General diagram of an air diffusion pump



Care must be taken to insure that the oil diffusion pumps are never exposed to high pressure while still hot. To do so will overheat the pumping capacity of the system, forcing pump oil into the analyzer chamber, as well as oxidizing the pump oil. Relays connected to pressure gauges automatically turn the pumps off if the pressure in the main analyzer chamber exceeds 10^{-3} Torr. To protect the pumps from overheating, the temperature and pressure of the recirculating water is monitored and the oil heaters are turned off if there is a drop in water pressure or if the returning cooling water is above 100°F .

To prevent pump oil from diffusing into the analyzer chamber (backstreaming), diffusion pumps are equipped with baffles at the top of the pump. In addition to the baffles, a liquid nitrogen trap is installed on our system to improve pumping efficiency and to provide additional protection from backstreaming (30, p. 201).

The pressure in each of the analyzer chambers is measured using Bayport-Alpert type hot cathode ionization gauges (PWC, Model 553) (30, p. 43). This type of gauge uses an electron emission filament to ionize the residual gas in the gauge tube. Pressure is determined by measuring the ratio of ion-to-electron current, multiplied by a sensitivity factor. Hot cathode gauges are well suited for operating between 10^{-7} and 10^{-2} Torr (30, p. 428). A thermocouple gauge (Tele Dyna, Model CV-40) is used to monitor pressure in the glow discharge chamber because its operating pressure (around 1 Torr) is outside the range of Bayport-Alpert gauges. Thermocouple gauges measure the resistance of a

thermopile which varies as the conduction of heat to the walls of the gauge changes with the pressure (83, p. 487)

Ion Detection

Ions that pass through the mass filter are detected by a transducer that converts the ions into an electron current. In our system, two transducing elements are available: a Faraday cup and an electron multiplier.

Faraday Cup

The Faraday cup (also called a Faraday plate) is the simplest type of ion detector (91, p. 344). It consists of an electrically isolated metal plate placed in the path of ions exiting the mass filter. As ions strike the plate, they are neutralized by a flow of electrons directly proportional to the ion current. The electron current is then measured across a high ohmic resistor (typically $10^9 \Omega$). A common practice is to connect the collector plate to the inverting input of an operational amplifier (95, p. 134). The feedback across a high ohmic resistor is then used to measure ion current.

The output of a Faraday detector is independent of mass and the system is both inexpensive and rugged (91). When used in conjunction with an amplifier the pick-up noise must be minimized by using as short a connection as possible between the amp and the collection plate (92). The principal drawback to Faraday detectors is the slow response time of the amplifier.

The Faraday detection system in the mass spectrometer reported here uses a metal shield in front of the electron multiplier. As a Faraday detector the plate is isolated from the rest of the housing and connected to a feedthrough at the base of the detector flange. Faraday detection is rarely used with this mass spectrometer because its counterpart, the electron multiplier, offers better signal-to-noise ratio and faster response time. The Faraday plate must be grounded whenever the electron multiplier detector is used.

The Electron Multiplier

Virtually all of the ion detection reported in this work was collected using a channel electron multiplier (Galileo Electro-Optics Model 4411 4-Channeltron). The system is based on a single dynode, continuous channel design (44) that provides high gain with relatively little noise and minimal power requirements. An important advantage with the channel multiplier is that it can be used in either analog or (pulsed) mode (45), allowing ion signals to be recorded with single-shot events, real-time oscilloscope traces, or with digitized electronics.

Inter-quadrupole mass filter, the channel electron multiplier is often mounted off axis to reduce the amount of background noise from neutral species and photons traveling down the axis of the mass filter (46, p. 140). A high negative voltage (-1500 to -2000 V) is applied between the entrance of the channeltron multiplier and the housing enclosing the end of the quadrupole rods. Positive ions exiting the quadrupole "see" the electric field at the end of the multiplier and

are drawn towards its surface. The resulting ion collision emits secondary electrons that are accelerated down the dynode channel, generating additional electrons with each subsequent collision with the walls of the multiplier. The electron current is collected by a metal plate at the base of the multiplier.

In the analog mode, the electron current is connected to a preamp head (Sairi, Model C21-6 Fast Electrometer) in the same manner as the Faraday detector. The preamp head is connected to an electrometer (Sairi, Model C24-2) that controls the detector voltage, directs the analog signal to various outputs and determines the value of the feedback resistor (three possible values: 10^7 , 10^8 , and $10^9 \Omega$). The analog mode is useful for generating a signal compatible with undigitized devices and allows significant features of the mass spectrum to be observed at lower detector voltages than in counting mode.

When used in pulse counting mode, the detector is operated at a higher voltage than in analog mode in order to saturate the output of the multiplier, creating short pulses approximately 30 ns in duration [35]. These pulses are directed to a pulse-height discriminator (PSD Instruments, Model 1120) that filters out pulses below a predetermined intensity, eliminating spurious signals and improving the signal-to-noise ratio. In counting mode, the output signal becomes a stream of pulses that can be directed to various data handling instruments.

Data Handling

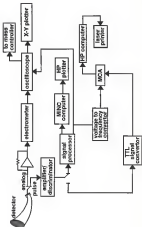
There are several methods available to manipulate the signal generated with the channel multiplier. Figure 34 is a schematic of the commonly used signal router. The particular application determines which method is used to accumulate.

Analog Methods

As described in the previous section, the analog signal is directed to a preamp head before entering the electrometer. The analog signal is then passed to a digitizing oscilloscope (Tetronics, Model 5223 with digitizing/timebase Model 5228) that permits both real time and stored digitized signal display. The oscilloscope has a time base output that sweeps the mass spectrometer in synchronization with the oscilloscope trace, allowing the operator to view the mass spectrum while adjusting instrument tuning parameters.

Any analog signal on the oscilloscope can be converted to a hard copy by digitizing the image, storing the image in the oscilloscope memory, then transferring the trace to an X-Y plotter (Houston Instruments, Model 3000). Since it is possible to output mass spectra using this technique, it is better suited to record the time-dependent shapes of transient signals, such as individual ion profiles from a pulsed glow discharge.

Figure 26 Possible routes for ion signals generated with the channel electron multiplier



Pulse Counting Methods

Pulse signals from the detector are first directed to a amplifier/discriminator (A/D) to reduce signal noise by eliminating signal pulses below a specific threshold (the discriminator), followed by an amplifier stage to provide a high speed (50 nsec) source of pulses for signal counting equipment. The output signal is directed to an an signal processor (EG&G Princeton Applied Research, Model 1112) or a multichannel analyzer (MCA, Tracor Northern, Model 7500).

The ion signal processor is used to collect mass spectra that require the analysis of trace components in the sample. Pulse signals from the A/D are accumulated over a specified time period (1×10^{-3} to 1 sec) and the total counts displayed or transferred to the controlling computer (Digital Equipment Corp., Model MMC-11). When under computer control, the accumulation time is determined by the program (typically 1×10^{-3} sec) and coincides with a single step across the mass spectrum. The current MMC program subdivides each mass unit into 40 steps. After each step, the total counts from the signal processor are transferred to a storage buffer assigned to that mass step. Once the data are stored, the signal processor is cleared, the mass spectrometer is advised to pass the next mass increment, and the signal for the next step accumulated. By repeating this process, a complete mass spectrum over the desired mass range is assembled and stored in the computer memory. The mass range can be started as many times as necessary to accumulate well defined peaks. The mass spectral data are displayed on a high resolution screen (Tektronix, Model

4090-1) for temporary data analysis, stored on floppy disk for future reference, or plotted on paper using a computer controlled X-Y plotter (Hewlett-Packard Model 9870C).

The signal processor also has an output terminal suitable for displaying the digitized data on the same oscilloscope used to trace analog signals. This output converts the accumulated count into a voltage compatible with the oscilloscope. When used in this manner, the accumulation time is set by the operator using thumb dials on the front of the signal processor.

An additional feature of the signal processor is the ability to select data through narrow windows synchronized with an external trigger. This feature is used with pulsed glow discharges and allows mass spectra to be accumulated in specific regions of a time-varying discharge. Data can be stored with the MNC, MCA, or displayed on the oscilloscope.

In situations that do not call for features available on the signal processor, it is possible to bypass the system and accumulate data directly with the MCA. The signal must first be converted through a TTL converter (JDS Instruments Model 1102 NIM SR) because the maximum output of the A/D is less than 1 volt and is not compatible with instruments that require TTL pulses (such as the MCA). The MCA can be connected to a Hewlett-Packard computer (Model 9810) for storing the resolved data on disk and making hard copies of the information with a laser printer. A recently installed interface between the mass spectrometer and

The Hewlett-Packard computer allows mass spectra to be accumulated and stored on the MCA using this by-pass feature.

CHAPTER 3 PULSED DIRECT CURRENT GLOW DISCHARGE MASS SPECTROMETRY

Background

Pulsed Glow Discharges in Optical Spectroscopy

In a pulsed glow discharge the applied voltage is interrupted to periodically extinguish the discharge. The most notable application of pulsed technique is to increase the output of hollow cathode lamps for use in fluorescence and atomic absorption work (94). Dawson and Ellis (97) have reported a 50 to 100 fold increase in the output intensity of pulsed discharge lamps versus lamps operating continuously.

Pulsed glow discharge lamps have also been used to provide the modulated carrier wave to improve signal-to-noise ratios using a lock-in amplifier (95). A more sophisticated application of the pulsed glow discharge is to use the sputtered atoms as resonance absorbers (96, 100). This is accomplished by passing the light from a d.c. glow discharge (or other analytical emission source) through a pulsing discharge; the sputtered atoms in the pulsed discharge absorb light at their resonance frequency; selectively modulating the light from the emission source. Pulsed glow discharge lamps have also been used for simultaneous multielement analysis of samples aspirated into a flame (101) using four or five different lamps as fluorescence excitation sources. The lamps are

sequentially pulsed, producing short bursts of resonant radiation that selectively excite elements in the flame.

The glow discharge produces a plasma cloud of sputtered analyte atoms that can be used for atomic absorption, fluorescence, and emission measurements (9). Here, too, pulsed glow discharges have been put to good use. As an emission source, pulsed discharges have been reported to yield better precision and accuracy than steady-state dc sources (102). Noting that emission signals from a pulsed discharge dissipate before all of the sputtered atoms diffuse to the walls of the chamber (103), Winefordner et al. (104) have used laser excited fluorescence in the dark period between pulses to measure atomic populations in the discharge. This technique has the advantage of eliminating background emission, and has been reported to allow detection limits in the femtogram range for some elements (105).

Pulsed Glow Discharges in Mass Spectrometry

Time-resolved studies of glow discharge emission signals (106) indicate that a significant population of neutral species is present in the afterglow. This led our laboratory to investigate the possibility that a similar phenomenon might exist for elemental ions (107).

In glow discharge mass spectrometry, the ion signal intensity is proportional to the population of sputtered analyte atoms (78). It is possible to increase the population of sputtered atoms by increasing the applied voltage,

thereby increasing the average energy of species bombarding the cathode surface and improving the sputter yield. In an abnormal glow discharge, this increase in voltage is accompanied by a higher current density that can overheat the cathode. It is possible to reduce the amount of cathode heating by circulating cooling water through the cathode holder, but this method is not very effective when using pin shaped samples and introduces potentially catastrophic complications in the vacuum system if a leak develops. Pulsing the glow discharge provides a means to increase the applied voltage as well as a period between pulses for the cathode to cool.

In order to maintain the same average current in a pulsed discharge as in an uninterrupted d.c. discharge, the applied voltage must be increased during the ON portion of the pulse duty cycle. Figure 25 is a plot of the relationship between voltage and current at several duty cycles. Because of the increased voltage required to drive the same average current over shorter duty cycles, ions arrive at the surface with a higher average kinetic energy. A comparative sputter yield study was undertaken to evaluate the effect of the increased voltage on the cumulative weight loss of a copper pin (100). Figure 26 is a plot of the weight loss of a copper pin in a pulsed and uninterrupted discharge operating with the same average current of 1 mA in 1 Torr of argon. A 10 to 15 % increase in sputter yield was noted for the pulsed discharge over an equivalent current d.c. discharge. This is lower than the estimated 40 % increase based on Figure 8, although this estimate is not directly applicable because the sputter yield data in

Figure 25: The effect of changing the pulse duty cycle on the current storage relationship in a 1-Tan argon discharge using a 2 mm diameter capillary pin

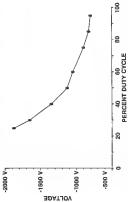


Figure 16. Weight loss comparison between a d.c. and a pulsed discharge using a copper pole (100). The average current was 1 mA, required a discharge voltage of 900 V for the d.c. discharge and 1000 V for the pulsed discharge (pulse was 50 Hz with a 60 % duty cycle). The discharge pressure was 1 Torr.

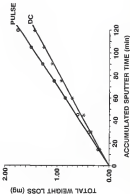


Figure 8 were acquired under vacuum conditions (44). Data in Figure 20 were acquired in a 1 Torr argon environment in which a large amount of sputtered material redeposits back onto the cathode tip, reducing the observed weight loss.

The intensity of the ion signals from the pulsed and steady d.c. discharge was also compared (508). Plotted in Figure 22 is a comparison of the ion signals observed at various discharge currents. The applied voltage increases with increasing current. The ion signal for the pulsed discharge is about a factor of 2 higher than for the steady d.c. discharge. This is higher than the sputter yield increase observed for the pulsed discharge, indicating that ionization factors (which are more complex to evaluate than the sputtering step) also affect the observed signal.

Ion Signal Profiles

In addition to the increased sputter yield and improved ion signal intensity, the time-dependent responses of individual ion signals in a pulsed glow discharge display reproducible anomalies that do not match the square wave signal driving the power supply. Illustrated in Figure 23 are the two types of ion signal profiles observed in a pulsed argon glow discharge.

The output voltage of the power supply as it follows a controlling square wave is illustrated in Figure 24a. The ion signal profile observed for contaminant gas species (C^+ , H_2O^+ , CO^+ , and N_2^+) is shown in Figure 24b. Figure 24c is the time-dependent response for pulsed sputtered species. At the beginning of the

Figure 27 Comparison of the relative ion signals ($I_{\text{ion}}/I_{\text{H}_2}$) from a d.c. and a pulsed discharge using a cryogenic jet expanding to 1 Torr (upper) [127]. The pulsed discharge was operating at 100 Hz with 50 % duty cycle.

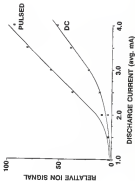
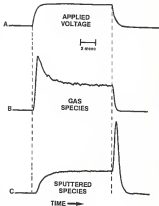


Figure 28 Ion signal profiles in the pulsed discharge. (a) applied voltage (0 to -1000V). (b) signal for ionized gas species (here: H_2O^+). (c) signal for sputtered species (here: $^{56}Fe^+$). The discharge gas was argon at a pressure of 1 Torr using a low-alloy steel pin.



pulse cycle, the distinguishing feature is the increase in the ion signal intensity for contaminant gas species, called the *prepeak*. The prepeak is noticeably absent in the ion profile for sputtered species. Instead of a prepeak, there is a slight delay, then the sputtered species signal gradually increases to a plateau value. Both sputtered and contaminant gas signals reach a plateau value as the applied voltage stabilizes and remain unchanged for the remainder of the ON portion of the pulse period, regardless of the pulse duration.

At the termination of the applied voltage, the ion signals for sputtered species and contaminant gases again behave differently. Gas signals rapidly decay to the baseline at the end of the pulse. In contrast, the sputtered species signal intensity increases at the end of the pulse, forming a *post-discharge peak*, called an *afterpeak*.¹

The effect of the pulsed discharge on the ion signals observed in mass spectrometry has, to date, been unexplored. In this chapter, factors controlling pulsed ion signal profiles and the use of those factors to improve the analytical performance of glow discharge mass spectrometry are investigated.

Equipment

Caland, Power Supply

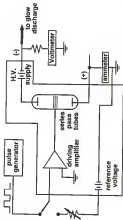
The principal piece of equipment controlling the pulsed discharge is a high voltage power supply (Rapon, Model CP50500) whose output can follow a 0 to +6 V control voltage. The high voltage is controlled by two series pass tubes

whose conductance varies with the voltage applied to internal tube grids as illustrated in Figure 28. By controlling the voltage on these grids (e.g., applying a square wave pulse), the operational power supply can be used as a pulsed mode amplifier. The maximum output voltage for this power supply is rated at 2800 V with a maximum current of 10 mA.

The output of the CP50000 is controlled by manipulating the voltage in the heating terminal of the driving amplifier (see Figure 28). Two control paths are possible. The first uses an internal reference voltage that passes across a variable resistance pot and is connected to the heating terminal. This is the method used to control steady state d.c. voltage. The second control path relies on the input of an external control voltage, such as from a pulse generator, this allows control of the output voltage in the pulsed mode. A control voltage of +5 V will drive the power supply to its maximum output.

Current and voltage to the discharge are monitored using Q Anorval meters. The type of meter averages the current and voltage measurements during the pulse cycle. Therefore, at a 50 % pulse duty cycle, the discharge current and voltage are twice the values indicated on the meter. The voltage is monitored by placing the voltmeter (Jenpron, Model 32) and its matching 50-M Ω resistor in a circuit parallel to the d.c. voltage. The current is monitored by placing the ammeter (Triplett, Model 425-1) in series with the return side of the high voltage circuit (this was done as a safety consideration because the meter

Figure 28 Simplified schematic diagram for a high voltage operational power supply



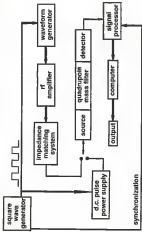
housing was not designed to hold back the voltages used with the glow discharge.

Pulsing Circuit

The operational power supply was controlled by one of two pulse generators, depending on the type of discharge pulse desired. Most of the work reported here required a simple square wave pulse. For this purpose a Hewlett-Packard Model 8000A was employed. Important features of this pulse generator are output voltages up to +45 V, pulse rates from 0.01 Hz to 10 MHz, variable duty cycle from 1 to 99 %, and an external control feature that allows an auxiliary signal to trigger single pulses whose duration is controlled by the pulse generator. A Hewlett-Packard Model 3302A waveform generator was used in experiments requiring pulse shapes other than a square wave. This waveform generator can produce square, sine, sawtooth, and triangle shaped pulses at a fixed 50 % duty cycle. The output is variable from 1 mV to 10 V (peak-to-peak), with a frequency range between 0.001 Hz to 10 MHz (20 MHz with the sine wave function). This unit cannot be triggered externally by a single trigger pulse.

Figure 10 is a schematic of the instrumentation layout used with pulsed discharges. Regardless of which pulse generator is used, the output is connected to the OPS 3000 power supply using a BNC cable hardwired to the internal terminal that leads to the voltage driving amplifier. To control synchronization between the data collection system and the pulsing discharge, a trigger signal is

Figure 10 Block diagram for pulsed GDM



sent to the data system at the beginning of the pulse cycle. The timing between the pulsed discharges and the data system is controlled by a pulse delay box that can slow the arrival of the trigger pulse up to 50 msec.

To perform time-resolved studies with the pulsed discharges, it is important to be able to partition data collection windows over selected areas of the pulse period. Selective data collection is made possible with the use of a Princeton Applied Research, Model 1112, signal processor. Originally designed to process signals from a photomultiplier using background subtraction techniques, the instrument features two identical electronic data gates that can collect data at different times in the pulse period. The first data gate opens with the positive-going edge of a synchronizing square wave and remains open for a period of time set by the operator (or computer). The second data gate opens at the negative-going edge the square wave for the same duration as the first gate.

The position of the data gates in the pulse period is controlled by the pulse delay box. In the pulse delay box, the synchronization trigger from the pulse generator is divided to a retriggerable monostable multivibrator (Texas Instruments # SM74LS120) that outputs a square wave to control the signal processor. A resistor-capacitor (RC) time constant determines the delay before the square wave is sent to the signal processor and a second RC circuit determines the duration of the square wave. By varying the resistor values, the arrival time and duration of the square wave can be adjusted, thereby controlling the position of the data gates.

The usual procedure is to initiate the pulsed discharge and to use one channel of an oscilloscope to observe the resulting ion signal at a single mass-to-charge ratio. The gates from the signal processor are simultaneously displayed on the second oscilloscope channel. The position of the data gates is adjusted while observing their position relative to the pulsed ion signal. This procedure allows a data gate as narrow as 1 μ sec to be placed anywhere in the pulse period. The signal processor will integrate the total number of counts collected for the duration of either of the two data gates and then pass this information to the computer.

The Prepeak Region

The Sample Surface Between Pulses

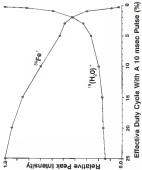
The prepeak region is defined as the beginning of the discharge pulse to the time that ion signals reach their plateau values. When examining the factors that influence the pulsed discharge, the condition of the sample surface at the beginning of the pulse period must first be considered.

In a steady-state discharge, the sample is continuously sputtered by energetic argon ions that remove the surface layers and maintain a "clean" surface. In the pulsed discharge, the sputtering process is periodically interrupted and the sample is exposed to a flux of argon atoms that can physisorb onto the sample surface (105, 544). At a pressure of 1 Torr, the rate at which argon atoms arrive at the surface is approximately 3.0×10^{22} atoms cm^{-2}

year⁻¹ (18, p. 302). Coexisting with the argon will be contaminant gases such as water and carbon dioxide. Some of these gases can react with the cathode to form numerous compounds (e.g., oxides) that are bonded to the surface. Such chemisorption could have a significant influence on the sample surface over time. Although contaminant gases are a minor component of the species striking the surface compared to the number of argon atoms, displacement of physisorbed argon with compounds chemically bonded to the surface would be a cumulative effect.

The effect of absorbed gases on the ion signal was evaluated by fixing the pulsed discharge ON time duration at 10 msec, then increasing the amount of time between pulses and observing the matrix and water signals for 1000 pulses (illustrated in Figure 9) is the effect of increasing the pulse OFF time using an iron pin in a 1 Torr argon discharge. The ion signal intensities were recorded in the plateau region so as not to be influenced by the prepulse or afterpulse. As the time between pulses increases, the ON time duty cycle. The x axis in the plot shows the ON time duty cycle. The OFF time between pulses increases from left to right in the plot. There is little change in the H_2O^+ signal with increasing OFF time until a 3% duty cycle (190 msec OFF time) after which the water ion signal increases sharply. The iron signal steadily decreases with decreasing OFF time, but the signal loss is particularly rapid after the 190 msec OFF time. Factors that could be influencing the ion signal intensities at OFF times greater than 190 msec include cathode cooling, adsorption of contaminant gases, increasing thickness

Figure 6: Saturated (H_{sat}) and contained gas ($p_{\text{g},0}$) ice signals as the CPT lens substrate (pulses is increased) the distance (0) lens will measured at 10 meter and represents a decreasing duty cycle as the time between pulses is increased (i.e. from left to right on the x-axis).



of adsorbed layers, or the accumulation of chemically bonded species such as oxides. It is unclear whether this effect represents a sputtering phenomenon or if changes in desorption are occurring as well. These data indicate that if an upper limit of 150 msec between pulses is maintained, the effects of the OFF time on the pulsed discharge signals are not significant.

Analysis of the Ionization Period

The prepeak illustrated in Figure 1(b) is only observed for contaminant gas species. Figure 1(b) is an expanded view of the prepeak region. In addition to the prepeak, the other distinct characteristic of this portion of the pulse cycle is that gas species signals appear earlier in the pulse period than sputtered species.

Earlier work has shown that ions sampled by the mass spectrometer originate from ionization reactions near the exit orifice (137). Therefore, the distance between the sample and the exit orifice should play a role in determining the timing of ion signals in the pulsed discharge. To study the effect of sample distance on signal timing, an experiment was conducted in which the distance from the end of a low-alloy steel pin to the exit orifice plate was varied from 2.5 cm (the edge of the dark space is a 1 Torr discharge) to 11.1 cm (beyond which ion signal intensity begins to decrease rapidly). Ion signals for individual species were collected with a multichannel analyzer (MCA) and the signal induction time determined by counting the number of channels from the application of the high voltage to when the signal begins to appear on the MCA. Listed in Table VI are

Figure 86. Expanded view of the prepeak region showing gas species (H_2O^+) and ionized species (H_2e^+). The probe interval 50 ms with a 50 % duty cycle operating in a 1 Torr argon environment. The sample was a low-alloy steel (wt)

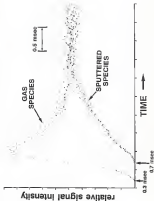


Table VII
Signal Initiation Times
in a 50 Hz Pulsed Discharge

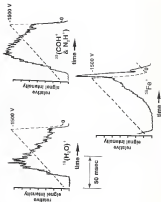
	0.30 cm	0.55 cm	0.87 cm	1.1 cm
H_2O^+	0.171	0.171	0.171	0.247
$^{56}\text{Fe}^+$	0.456	0.513	0.703	0.817

All initiation times are in milliseconds (± 0.036 msec).

the initiation time for gas species (H_2O^+) and sputtered species ($^{55}\text{Fe}^+$) as the sampling changes. As the cathode was moved closer to the exit orifice the initiation time for the sputtered species decreased with distance. The gas species signals, however, remain unaffected by sampling distance. Sputtered species signals are associated with the time required for sputtered atoms to diffuse across the sampling distance to the exit orifice, the closer the sampling distance, the earlier in the pulse period sputtered species signals appeared. Because gas species exist throughout the discharge space, diffusion time does not play a role in the appearance of these signals at the beginning of the pulse cycle. Instead, electron ionization of the gas species near the exit orifice determines when these signals appear during the pulse period. These data indicate that the factors controlling the prepulse must be associated with ionization mechanisms and are not directly related to sputtering.

In order to examine closely how ionization affects the prepulse, the high voltage pulse was modified by replacing the rapidly changing square wave with a slowly increasing smooth wave. Figure 33 is an illustration in which the applied voltage is overlapped with the observed ion signal. The responses of H_2O^+ and COH^+ (two examples for hydride interferences that are often observed in the glow discharge) is typical of signals observed with gas species. At the beginning of the ramping voltage, no ions are observed until the glow discharge is initiated (around 300 V), then the signals increase with increasing voltage. The signal continues to increase with increasing voltage, up to approximately 400 to

Figure 50. Sawtooth pulses for signal profiles. Obtained from a steel pen operating in a 1 Torr argon discharge with a pulse rate of 10 Hz.



-1000 V, whereupon further increases in the applied voltage result in a lowering of the observed ion signal. Also shown in the figure is a trace of a sputtered species signal to illustrate that ion signals associated with sputtering phenomenon react differently to a slowly changing voltage. This phenomenon is also observed using triangle waves, with gas species signals reaching a maximum at approximately the same voltage on both the rising portion and the decaying portion of the triangle voltage pulse, as seen in Figure 24.

The intensity of the prepeak relative to the plateau is associated with the applied voltage. This can be illustrated by using a high voltage square wave of varying amplitude as shown in Figure 25. In the figure, the voltage at which each trace was collected is the peak voltage of the applied square wave. As the maximum of the applied voltage is reduced, the difference between the prepeak and the plateau becomes smaller because the applied voltage does not extend past that yields electron energies that effectively transfer their energy to the electrons in the negative glow.

To explain the prepeak, it is necessary to consider the ionization mechanisms that control the contaminant gas species ion signals. The important ionization mechanisms in the glow discharge are Penning ionization and electron ionization (EI). In an argon glow discharge, the only source of ionization for gas species is EI, because the metastable energy levels of argon atoms are too low to ionize these species (see Table II). As noted in Chapter 1, the energy of electrons in the negative glow region is usually modeled as conforming to a

Figure 24. Triangular pulse ion signal profile for H_2O^+ . The applied voltage (left axis) is the dashed line overlaid onto the water ion signal (right axis). Operating conditions were a pressure of 1×10^{-6} Torr argon using a small sample pin and a pulse rate of 50 Hz.

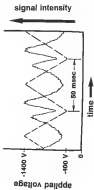
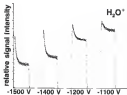
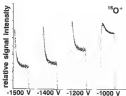


Figure S5: Ion signal profiles for two gas species at varying discharge voltages, the discharge voltage is listed under each trace. The pulse rate for all traces was 80 Hz with a 30 % duty cycle, operating in a 1 Torr argon discharge using a steel sample pin.



Boltzmann distribution, though Langmuir probe experiments indicate a deficiency of high energy electrons in the tail of the distribution (24). Most electrons in the negative glow are secondary electrons that have a mean energy of around 2 eV (15, p. 32), and are not energetic enough to excite/condense gas species. For an increase in the ionization of gas species, the distribution of secondary electrons must be shifted to increase the population of higher energy electrons.

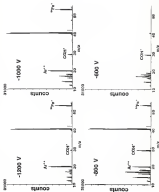
One way in which the discharge influences the secondary electron energy distribution is through interactions between low energy electrons moving randomly in the negative glow and high energy electrons passing through the negative glow. Primary electrons emitted from the sample surface during the sputtering process are the principal source of high energy electrons. These electrons are accelerated by the electric field across the dark space and "injected" into the discharge at high velocity. As primary electrons pass through the plasma, their energy can be attenuated by coulombic interactions with the slower moving secondary electrons (110). These interactions "heat-up" the secondary electrons, shifting their mean energy distribution to a higher value and increasing the population of high energy electrons in the upper end of the Boltzmann distribution. Because the collisional cross section of an electron is higher at lower velocities (32, p. 32), the energy transfer process is anticipated to be more efficient at lower primary electron velocities. That is, the mean energy of the secondary electrons is probably higher when the primary electrons are accelerated with smaller voltages across the dark space. The process would

explain both the transient nature of the prepeak (as primary electrons are accelerated across a rapidly changing voltage) and why gas species plateau values are highest at voltages near those yielding the highest ion signals on a slowly changing waveform.

Applications to GC/MS Spectra

The information gained concerning the relationship between gas ion signal intensities and the applied voltage can be used to improve GC/MS spectra. Referring again to Figure 26, the variation in the plateau values with the applied voltage indicates that operating the glow discharge at voltages greater than those yielding the highest plateau would reduce the signal intensity of gaseous interferences. This effect is shown in Figure 34. All four mass spectra in the figure were collected at 1 Torr argon using an SRM 1284 low-alloy steel pin. The only difference between the spectra is the operating voltage, which varies from -1500 V to -600 V. Interfering gas species signals such as water and COH^+ are lowest at -1500 V. As the voltage is lowered to -600 V, gas species signals reach their maximum, then begin to fall as the voltage is reduced to -600 V. These data indicate that the glow discharge should be operated above the voltage that yields the highest signals for gas species (usually above -1000 V) in order to reduce isotopic interferences from these species.

Figure 58. The effect of the d.c. discharge voltage on the gas species signal in a 1 Torr argon discharge using a low-frequency modulator.



The Plateau Region

The plateau region is the portion of the pulse-duty cycle when ion signals for both sputtered and gas species reach a steady value. For contaminant gases this is the point to which the pressure decays after passing through its maximum, usually 3 msec into the pulse period. Sputtered species also require approximately 3 msec to reach their plateau value, including the time delay required to diffuse across the negative glow.

The output voltage of the power supply is directly proportional to the amplitude of the controlling square wave and the duration of the pulsed discharge is determined by the width of the square wave. Because the operational power supply has a rapid response to the controlling waveform, there is an internal dampening circuit to prevent the output voltage from overshooting the desired voltage and "ringing" as the maximum voltage is reached. This dampening circuit allows the initial portion of the applied voltage to rise rapidly, but the rate slows as the output reaches its maximum, delaying the onset of the plateau. The timing of the pulsed high voltage was measured on an oscilloscope using a special probe (Tektronix, Model P6013A). The P6013A probe is designed to allow pulsing, high voltage waveforms to be observed on an oscilloscope while introducing a rise time error of less than 15 nsec. Three measurements indicate that the power supply reaches 80 % of the programmed output voltage in 0.80 to 0.87 msec. The remaining 10 % of the applied voltage is achieved in approximately 1 msec. From the applied voltage standpoint, the plateau region

occurs approximately 2 msec after the initiation of the pulse cycle. As noted earlier, ion signals stabilize around 3 msec into the pulse period. Therefore it is the ion signals, instead of the power supply, that determine the maximum pulse rate if the discharge is to stabilize during the pulse cycle. This sets an upper limit on the pulse rate at 150 Hz with a 50 % duty cycle (i.e., 3 msec ON and 3 msec OFF).

There is little difference between mass spectra collected in the plateau region of a pulsed discharge and a steady-state discharge when both are operated at the same voltage. This is illustrated in Figure 3F using a low alloy copper pin. Both the d.c. and the pulsed mass spectra are taken from a digitizing oscilloscope. The small difference between the d.c. and pulsed copper peaks is within the signal variation observed on the oscilloscope in real time. The only notable variation between the two discharges is the ratio of the water signal to the H_3O^+ signal. This effect is often observed when using samples susceptible to water contamination, probably because the desorption of water from surface is dependent on the cathode temperature.

One advantage of the pulsed discharge is the ability to operate at higher voltages than its steady-state d.c. counterpart without overheating the sample. This can be illustrated by determining the voltage at which a 2 mm diameter sample pin begins to overheat (i.e., glow red), as listed in Table VII. This becomes an important consideration when using sample pins (> 1 mm diameter,

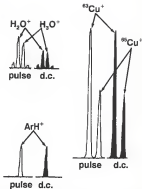


Figure 17—Comparison of ion signals from a d.c. and a pulsed discharge. Both discharges were operating at a 1 Torr argon environment with peak voltages at ~ 1000 V using a copper sample pin. The pulse rate of 50 Hz with a 50 % duty cycle.

TABLE VIII
MAXIMUM DISCHARGE VOLTAGE
WITHOUT OVERHEATING THE CATHODE

	steady-state d.c.	pulsed d.c.
1.0 Torr	-1700 V	>-2000 V
1.2 Torr	-1400 V	>-2000 V
1.5 Torr	-1250 V	-1900 V

which are prone to overheating) or materials that could be damaged by excessive heat.

Once the pulsed discharge reaches the plateau, there is little change in ion signal intensity for the duration of the plateau. The mass spectra in Figure 38 were accumulated with the same data gate (1 msec), but at different times during the pulse period (here using a 55 Hz, 55 % duty cycle pulse for a total pulse period of 20 msec). Figure 38a was collected 4 msec into the pulse period, just after the ion signal and power supply reached their plateau value. Figure 38b was collected halfway through the plateau region, and Figure 38c was collected immediately before the pulse terminated. All three spectra are plotted on the same scale and do not display any significant differences in signal intensity.

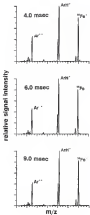
The Afterglow Feature

Discharge Termination

The most outstanding feature after the voltage is terminated is the sudden surge in ion signal intensity called the afterglow. In an argon glow discharge, this feature is unique to sputtered elements and species that combine with sputtered components to form small polyatomic species (e.g., metal-argon chloride molecules).

The time period immediately following the termination of a pulsed discharge has been the subject of other investigations. Bondi (117) has studied electron densities in neon and helium pulsed discharges using a resonant

Figure S8. Mass spectra collected through a drift window at different times in the pulse period.



monomers early. Those studies indicated that collisions between metastable atoms increase the electron population increases in the first 0.1 msec after the pulsed voltage is turned off. Strauss et al. (112) studied the metastable population in the post-pulse region using atomic absorption spectroscopy. The metastable population was observed to increase in the first 0.15 to 0.20 msec after the discharge was terminated. They attributed this phenomenon to low energy electrons recombining with argon ions to form metastable atoms.

Figure 16 is an expanded view of the steep-rise region of a pulsed argon discharge. There is a delay period of 0.15 msec after the termination of the applied voltage, during which the ion signals remain at the same intensity as during the plateau region. The power supply output drops below the minimum voltage to sustain a discharge (around -300 V) too quickly to explain this phenomenon. From fluorescence studies using pulsed discharges (100), it is known that background emission becomes insignificant in less than 0.1 msec after the discharge is terminated. Furthermore, electrons require between 0.1 to 0.2 msec (111, 113) to reach thermal equilibrium in the post-pulse period of the discharge. This suggests that the 0.15 msec delay period in our discharges is due to electron thermalization after the applied voltage is terminated.

Afterglow Formation

When operating pulsed discharges at the same average current as an interrupted d.c. discharge, it is necessary to increase the discharge voltage

Figure 28. Expanded view of the diamond region. The expanded signal is the $^{13}\text{C}_2^+$ signal and the gas species are represented with the H_2O^+ signal. These traces were collected using a dwell time of 10 ms in a 1.5 Torr region discharge.

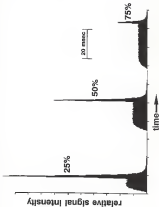


Figure 42 is a plot of the effect of duty cycle on the intensity of the afterpeak. As the voltage increases to drive the higher currents over shorter duty cycles, the intensity of the afterpeak increases.

The changing afterpeak intensity in Figure 42 represents a higher discharge voltage and a greater voltage change between the ON and OFF portions of the pulse cycle. The effect of the magnitude of the voltage change on the intensity of the afterpeak was isolated using a square wave pulse to which an offset voltage was applied during the OFF portion of the pulse period. This allowed the peak voltage to remain the same, but changed the voltage difference between the plateau and the afterpeak. The results of this experiment are illustrated in Figure 43. In the figure, the peak pulse voltage was -1000 V , while a -500 V d.c. offset voltage was maintained between discharge pulses. As the difference between the plateau voltage and the offset voltage decreased, the intensity of the afterpeak decreased as well. From this study, it appears that a voltage difference of at least 400 V is required to form an afterpeak and that the intensity of the afterpeak is proportional the magnitude of the voltage change.

Square wave pulses produce rapid voltage changes. To evaluate whether the rate of change influences the formation of the afterpeak, the square wave was replaced with a slowly changing triangle wave. Figure 42 is a plot of the ^{55}Fe signal while following a triangle and sawtooth waveform. Both traces were acquired with a peak applied voltage of -1000 V , a minimum voltage of -500 V , and a pulse rate of 20 Hz . While the ^{55}Fe signal is slightly higher on the

Figure 40. The effect of duty cycle on a 20 Hz pulsed discharge. The traces are the ^{210}Po signal from an iron sample pulse spacing is a 1 Torr argon discharge.



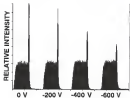


Figure 41. The effect of a d.c. bias voltage between pulses on the intensity of the ^{213}Pb alpha-peak. The pulse rate is 60 Hz with a 50 % duty cycle in 1 Torr argon.

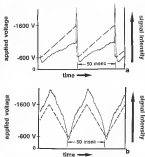


Figure 4b: The effect of voltage change on the steep peak: (a) sawtooth wave, rapid change when voltage terminated; (b) triangle wave, slowly changing

decreasing side of the triangle voltage pulse, the voltage change is too gradual to form an afterpeak. A sudden voltage change of at least 400 V is a prerequisite to form the afterpeak, suggesting that a rapid shift in the ionization mechanism or a sudden departure from equilibrium conditions is required.

Analysis of the Afterpeak

In an argon discharge, only species with ionization energies below the energy levels of the argon metastable atoms exhibit afterpeaks. This indicates that Penning ionization is the principal ionization mechanism after termination of the discharge voltage. The role of Penning ionization in the afterpeak was investigated by altering selected discharge parameters that were expected to interfere with metastable ionization of sputtered analyte atoms (bearing in mind that ionization processes in the negative glow can be interdependent and very complex).

Changing the sputtering gas used in the glow discharge changes the available energy levels available for Penning ionization. Referring to Table II in Chapter 1, the metastable energy levels of an argon atom are 11.58 and 11.72 eV, high enough to ionize most of the elements in the periodic table but not energetic enough to ionize most contaminant gases. Another commonly used glow discharge gas is neon. While neon does not sputter low-stay metals as efficiently as argon, its metastable energy levels (16.62 and 16.72 eV) are energetic enough to ionize most contaminant gases. If discharge gas metastable species are

responsible for ionization in the steeppeak than gas species with ionization energies too high to produce steeppeaks in an argon glow discharge should produce steeppeaks in a near-discharge if their ionization energy is less than 18.8 eV.

Exceeded in Figure 40 are ion signal profiles in the steeppeak region for the H_2D^+ species in argon and neon glow-discharges. The neon signal in the near discharge produces an steeppeak very similar to the steeppeaks observed with spalfield species in both neon and argon. This provides strong evidence that the metastable energy level of the discharge gas is the primary factor controlling ionization in the steeppeak region.

Early work by Strauss et al. (15) indicated that the metastable population increases in the first 0.2 msec after the discharge is terminated. Their study was limited to the time corresponding to the delay period between the end of the applied voltage and the start of the steeppeak. Sankick (16) has conducted a time-resolved atomic absorption study in the steeppeak region using an argon discharge and a copper pin. No increase in the metastable population immediately following termination of the discharge was observed. The metastable population remained constant during the 0.15 msec delay period, then began to decrease. This atomic absorption data is correlated to the steeppeak signal in Figure 40. Note that the metastable population declines faster than the neutral copper population and that the decay of the steeppeak appears to follow the decay of the metastable argon absorption signal. These data indicate that the

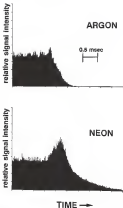


Figure 4b The effect of neon and argon on the afterpeak of ^{59}Fe in a 1 Torr discharge.

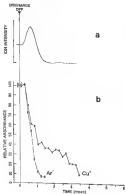


Figure 64. Atomic absorption and copper ion signal in the afterpeak region of a 50 Hz, 80 % pulsed discharge (10).

afterpeak is tied to the population of the ionizing medium (the argon metastable atoms) and not to the availability of the sputtered analyte atoms (the neutral sputter population).

The population of argon metastable atoms in the glow discharge is a balance of formation processes (e.g., the collision of argon atoms with low energy electrons, see Table II), and destruction processes (e.g., collision with the chamber walls or with atoms in the discharge and metastable collisions with electrons energetic enough to ionize the metastable atoms) (313). When the applied voltage is terminated, electrons emitted by the cathode surface are no longer available and the population of electrons energetic enough to ionize the gas species declines rapidly. The termination of electrons in the afterpeak region eliminates the principal source of metastable atoms. It also removes an important medium that deexcites the metastable atoms. With the loss of energetic electrons, metastable atoms must rely on other collisional processes to relax (including Penning ionization of sputtered material in the discharge space). The mean lifetime of metastable atoms in the afterpeak region of a 1 Torr discharge is around 5 msec (34). The loss of energetic electrons means that argon metastable atoms that would have otherwise been deexcited are now available to ionize other atoms in the discharge space. The sudden availability of "surplus" metastable atoms, coupled with a metastable-ionization cross section that is an order of magnitude higher than electrons at the same energy (32), may be the reason the scattered ion signal suddenly increases in intensity after termination

of the pulse voltage. This also would explain why the afterpeak decays at approximately the same rate as the argon metastable population.

If the supply of electrons is influencing the formation of the afterpeak, then an auxiliary source of electrons should alter the intensity of the afterpeak. To test this hypothesis, two discharges were setup in the same chamber. The first discharge was pulsed to form the afterpeak. It consisted of a nickel pin pulsed at 40 Hz, a 50 % duty cycle, and a peak voltage of ~ 1500 V. The second discharge served as the auxiliary source of electrons. It was comprised of a copper pin and was mounted parallel to, and 10 mm away from, the nickel pin. The second discharge was operated in steady-state d.c. mode at various voltages. Nickel and copper pins were selected so as not to introduce interfering atomic signals. Illustrated in Figure 40 is a series of pulsed "Vcr" signal profiles as the d.c. voltage on the copper pin increased. The d.c. discharge introduces a supply of electrons that increases with increasing d.c. voltage. This continuous flux of electrons deexcites the metastable atoms after the initial discharge is terminated. At ~ 1500 V (500 V below the maximum operating voltage of the pulsed discharge), the afterpeak is eliminated. Similar results were obtained when a relatively heated filament was used to inject electrons into the discharge (20). Increasing the intensity of the afterpeak was inversely proportional to the flux of electrons from the filament. The presence of electrons in the post-pulse period reduces the intensity of the afterpeak, presumably by deexciting the metastable atoms.

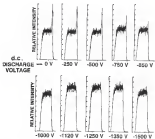


Figure 45: The effect of a second discharge (upper plot) on the afterpeak of "M". The operating pressure was 1 Torr. Voltage values along the x-axis are the d.c. potential to the copper cathode.

The evidence indicates that a sudden loss of electrons is necessary to form the steeppeak. The ion signal increase is associated with long lived metastable atoms, that would normally have been desorbed by electron collisions, surviving long enough to collide with analyte atoms still randomly moving in the discharge. A voltage change of at least 400 V is required to reduce sufficiently the flux of electrons to increase the lifetimes of enough metastable atoms to affect the ionization occurring in the discharge. Because the collisional cross section for metastable atoms is an order of magnitude higher than electrons, they are more efficient at ionizing the analyte atoms and the observed signal increases to form the steeppeak.

Observing Steeppeaks with the Ideal Bandpass Filter

Ion signals observed with most mass spectrometers, including quadrupoles, relied instrument tuning, rather than controlled sampling of the ions present in the source. One property of the steeppeak, not yet discussed is differences in instrument tuning parameters between steady-state dc and pulsed discharges.

From the instrument optimization standpoint, the most significant factor controlling the intensity of the steeppeak is the bandpass of the Bentel box energy discriminator. Recall from Chapter 2 that ions must be limited to a narrow energy range if the mass spectrometer is to resolve adequately sequential mass-to-charge ratios. The energy bandpass of the Bentel box is controlled by the potential on the housing. Figure 40 is a series of ion profiles for the $^{56}\text{Fe}^+$ signal

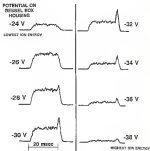


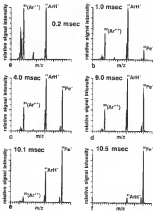
Figure 10: The effect of the Bessel box housing potential on the steepness of "Fe" in a 1 Torr argon discharge

from a -1500 V argon discharge as the potential on the Bessel box is increased from -24 V to -28 V. Although the exact ion kinetic energy cannot be determined from these plots, a relative trend is observed whereby the afterpeak appears in the ion profile at higher Bessel box housing voltages. Ion signals from a steady s.c. discharge optimized at around -28 V in the experiment. Differences in timing that rely on varying Bessel box housing voltages imply that there are variations in the kinetic energy of the sampled ions. Because sputtered atoms undergo numerous collisions as they effuse from the cathode surface to the exit orifice, it is unlikely that variations in kinetic energy originate in the sputtering process; this leaves ionization in the negative glow as the principal source of differences in kinetic energy. Assuming Penning ionization to be the dominant ionization mechanism in the afterpeak (which the evidence indicates), this dependence on the Bessel box housing voltages suggests that Penning ionization yields ions with a higher average kinetic energy than those observed from a steady state discharge (during which ion formation is a balance of field and Penning ionization). This may be due to a transfer of kinetic energy in the collision process as well as a transfer of ionization energy.

Applications to OAMS Studies

It is possible to take advantage of the differences in ion signal profiles for sputtered and gas species using numerical analysis to extract data at different times in the pulse period. Figure 47 is a collection of mass spectra accumulated using

Figure 47: Adeta species collected through a 0.2 mmx data gate placed over different portions of the pulse period

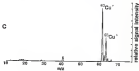
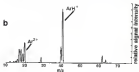
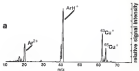


a 0.3 msec/gas systematically moved across the pulse period. At the beginning of the pulse period (0.2 msec), only gas species are observed in the mass spectrum. Sputtered species begin to appear 1.0 msec into the pulse. By 4.0 msec, the discharge has reached the plateau equilibrium and ion signal intensities remain unchanged for the duration of the plateau period (as seen in the mass spectrum 9.0 msec into the pulse period). Immediately after the applied voltage is terminated (10.1 msec), the gas species begin to decline in intensity. The final mass spectrum (10.5 msec) is well into the afterpulse region and the sputtered species become the single feature in the discharge. The spectra in Figure 47 were based on a 1 Torr argon discharge operating at -1000 V, with a pulse frequency of 50 Hz and a 50 % duty cycle. For clarity, all spectra were normalized to the highest peak intensity. There is an sigmoidal increase in the ion signal intensity from (a) to (g).

Figure 48 is a comparison of a steady-state d.c. mass spectrum and pulsed mass spectra collected through data gates placed at different portions of the pulse period. The peak pulsed voltage was set to -1000 V and the steady state d.c. discharge was also operated at -1000 V, using the same sample (STM C11 in brass pin, 2 cm diameter). All three mass spectra were collected through a 1 msec data gate.

Comparing d.c. and pulsed spectra in the prepulse, there is little difference in the vacuum-region species (i.e., $^{40}\text{Ar}^{++}$, $^{40}\text{Ar}^+$, and $^{40}\text{ArH}^+$). This is because the optimum voltage for formation of these species is the same as the operating

Figure 18. Comparison of the mass spectra of a brass pin using (a) a d.c. discharge, (b) a 100-Hz pulsed discharge while collecting data in the prepeak, and (c) the same pulsed discharge with data collected in the afterpeak. The operating pressure was 1 Torr argon.



voltage at which these spectra were accumulated (~ 1800 V), therefore the prepulse region and the d.c. discharge yield very similar signal intensities for these species. The situation is different for contaminants such as water, CO_2^+ and H_2O^+ . The ion signal for these gases optimizes at a lower voltage than the operating voltage of the discharge in Figure 48, and therefore have significant prepulse spectra collected in the prepulse yield ion signals higher than those observed in the steady state d.c. discharge.

Data collected in the afterpulse show an enhancement in ion signals for sputtered species compared to steady-state d.c. signals. This is not surprising given the similarity of the plateau and d.c. ion signal intensities and that the afterpulse intensity exceeds the plateau. This comparison should be viewed with caution. Because all three mass spectra in Figure 48 were collected through a 5 msec data gate, the total data collection time is the same. Under ordinary circumstances, however, the d.c. signal would not be gated. The computer program controlling the mass spectrometer used in these studies takes each unit mass-to-charge ratio and subdivides it into 40 steps. Without gating, the dwell time (data integration time) on each step is 18 msec. When gating is used, the dwell time per step is controlled by the pulse rate and data is collected only a fraction of that dwell time, based on the duration of the gate. In Figure 48, the pulse rate controlling the gate synchronization was 50 Hz (20 msec), but the data gate allowed data acquisition for only 1 msec. Therefore, data integration time for each step per sweep was only 1 msec, only 10% of the integration time used

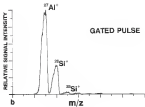
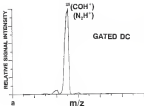
with a typical d.c. mass spectrum without gating. Narrowing the data gate improves the time resolution during the pulse period, but the number of scans must be increased to compensate for the loss of data acquisition time. This means that using pulsed discharges requires sacrificing data acquisition time in order to gain the ability to collect data selectively at different times in the pulse period. Of course, the number of sweeps to collect equivalent mass spectra is not directly proportional to data integration time because pulsed discharges can be operated at higher voltages than steady-state d.c. and the afterglow provides additional signal intensity. Nevertheless, more time is required to accumulate mass spectra from pulsed discharges.

In a steady-state d.c. discharge, the data acquisition time is limited by hardware considerations (e.g., computer speed, mass spectrometer response time) and the data acquisition system. When using pulsed discharges, it is the pulse frequency that is the limiting factor, because only one data point can be accumulated per pulse using data gates. Because the pulse rate is limited to around 10³ Hz if a stable discharge is to be established between pulses, the fastest data collection rate is 1 mass per data point in the mass spectrum.

Whether the advantages using the pulsed discharge outweigh the additional time required to accumulate the mass spectrum depends on the application. An example of a situation when the use of pulsing techniques is particularly advantageous is an examination of the silicon region of the mass spectrum from an ICPM (26) per. This region in the mass spectrum (m/e 28-30)

is particularly troublesome because of interference from CO^+ , N_2^+ , COH^+ , and N_2H^+ with the ^{26}Si and ^{26}Al isotopes. This problem is illustrated in Figure 4(a), in which the silicon peaks are completely obscured by interference. This mass spectrum was collected using a 3 mA, -1500 V discharge operating at 1.5 Torr argon pressure. Figure 4(b) was accumulated using a pulsed discharge operating at 3 mA average current, a peak discharge voltage of -2500 V, a pulse frequency of 10 Hz, a 50 % duty cycle, and collecting data 0.5 msec after the applied voltage had terminated. Both mass spectra were accumulated using the 0:1 mass-to-charge gate so that a direct comparison of the mass spectra was possible. The signal at mass 29 in (a) has an intensity of 181,000 counts and the ^{26}Al signal (which is barely visible in the mass spectrum) has a peak intensity of 1810 counts. In the afterpeak mass spectrum (b), the interfering signal is eliminated revealing the silicon peaks with an isotope ratio within 1 % of accepted values and the ^{26}Al signal (now the dominant peak) has a peak height of 1080 counts. By using the delay gate, the previously indiscernible silicon peaks are clearly visible without altering the signal of the aluminum (that does not experience any isobaric interference).

Figure 4b: Mass spectra in the silicon region using a gated dc discharge (a) and gated pulsed discharge in the afterpeak region (b). Both discharges were operated in a 10^{-6} Torr environment and the spectra were collected using a 0.1 msec data gate.



CHAPTER 4 PULSED DUAL CATHODE GLOW DISCHARGE MASS SPECTROMETRY

Background

The procedure for determining the concentration of trace components of a sample with GDMS is based on developing relative sensitivity factors (RSFs) for each element, using reference materials analyzed with the same instrument employed for the unknown analysis (69–114). A mass spectrum of the unknown is then acquired and the RSFs applied to the resulting isotope peaks, as described in Chapter 1. There are two drawbacks to the use of RSFs for trace analysis: 1) calculated RFS's may not be accurate if there have been significant changes in the instrument operating parameters, and 2) there is no way to compare quickly the standard and unknown to recheck the RSFs. This chapter addresses the feasibility of comparing directly the mass spectra obtained from a standard and an unknown sample using two pulsed glow discharges operating simultaneously in the same chamber.

Previous studies using multiple glow discharges relied on a second discharge to supplement the excitation and ionization of the primary discharge. Electrons emitted from the auxiliary discharge have been reported to increase the spectral line intensity from hollow cathode lamps (115–118) and analyses

emission sources [118, 120] by enhancing the excitation of atoms sputtered from the primary cathode. A similar technique has been reported using mass spectrometry [121] in which a second d.c. discharge was located in front of the exit orifice leading to the mass analyser. The additional ionisation from the auxiliary discharge improved the detection signals while simultaneously slowing the signals from polyatomic interferences. Another variation of multiple glow discharges in mass spectrometry [122] placed two identical cathodes at an angle of 90° to a line normal to the exit orifice, creating two symmetrical discharges with overlapping negative glow regions that improved the ion signal intensity.

The goal in earlier multiple discharge work was to increase ion signal intensity. The objective of the study reported here is to compare independent mass spectra, accumulated in synchronisation with each cathode, from alternately pulsing discharges. In this way, mass spectra can be accumulated for each pin under the same conditions of pressure and resonant operation. A qualitative determination of filamentation on one cathode can be made by comparing the peak heights of individual isotopes with the corresponding signals from the second cathode that serves as a standard.

Equipment

High Voltage Pulse Steering Box

To compare the ion signals from two electrically isolated cathodes, each must experience the same applied voltage. This precludes the use of separate power supplies because of the difficulty in matching exactly the high voltage outputs over the course of an extended analysis. Furthermore, to compare successfully two pulsing discharges, the timing between the cathodes' pulses and the data collection system must be controlled carefully.

To meet the above criteria, a single power supply is used and the high voltage directed to the desired cathode using a pulse steering box (PSB) that was designed and built by the Chemistry department electronics shop (Steve Miles, University of Florida). The high voltage output from a single power supply is connected to the PSB input terminal through an M/V connector. The high voltage is then directed to the desired cathode by an electronic circuit composed of a pair of FET switches (silicon μ MOSFETs) that, when excited in series, can withstand a maximum applied voltage of ~ 1250 V. The PSB provides pulse rates from 20 to 100 Hz. The duration of the applied voltage and the timing between individual pulses to each cathode is independently controlled through two discharges cannot be turned on simultaneously. Typical operating conditions are a pulse rate of 80 Hz, each pulse with a 25 % duty cycle (3 msec ON time), and with 5 msec between stimulus pulses. This pulsing scheme is illustrated in Figure 80.



Figure 82 Pulse sequence for the dual discharge

As described in the equipment section of Chapter 5, the signal processor can collect data through one of two independently positioned data gates. In dual pulse work, these gates are positioned using a synchronization trigger from the P88. A separate data gate is placed over each discharge (see Figure 5C). Because the duration of the two gates are identical, mass spectra are accumulated with the same integration time per data point.

Dual Insertion Probe and Shielding

To accommodate two-sample cathodes, the usual insertion probe (with a single feedthrough and a shaft 1/2 inch in diameter) is replaced with a probe that has multiple feedthroughs (and a shaft diameter of 1/2 inch). Each feedthrough in the larger insertion probe is electrically isolated and has its own high voltage connection. The insertion probe is placed in the discharge chamber by passing it through a Caprell high vacuum fitting. The fitting is connected to a bellows assembly that permits the position of the insertion probe to be adjusted inside the chamber, allowing alignment of the cathodes relative to the exit orifice. Both the insertion probe and bellows assembly are illustrated in Figure 5D.

The limited space between the feedthrough connections required redesigning the sample shielding. The usual ceramic Macor® shield was replaced with a narrow glass tube that fit securely over the ceramic portion of the feedthrough. Because the inside diameter of this tube is 4.2 mm, and the samples are usually just 2 mm in diameter, it was necessary to leave a ceramic

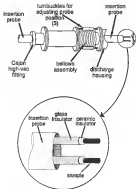


Figure 81 Direct insertion probe assembly

collar into the end of the tube to reduce the diameter and prevent the discharge from striking behind the sample onto the mounting hardware, see Figure 91. To insure that the two sample pins had the same surface area exposed to the discharge, care was taken to match closely the length of the new shields (25.4 mm).

Cross Contamination Between Cathodes

Before mass spectra from two cathodes in the same discharge chamber could be compared, it was necessary to evaluate how much cross contamination occurred between the samples. The principal source of cross contamination is sputtered material from one cathode diffusing across the discharge space and depositing onto the second cathode.

To evaluate the degree of contamination between the two sample cathodes, a copper wire (0.5 mm diameter 99.999% pure) and a Chromel A wire (a nickel-chromium alloy also 0.5 mm diameter) were mounted on the insertion probe parallel to one another in the discharge chamber. The probe was perforated in the discharge chamber so that both cathodes were an equal distance from the exit orifice. To verify that the two wires did not already contain small quantities of the base matrix of the other wire, each was analyzed in the mass spectrometer. This analysis indicated that no copper was detectable in the Chromel wire, and neither nickel or chromium were found in the copper wire.

Canyavar was evaluated by alternately pulsing the copper and Chloral wire, as illustrated in Figure 50, then observing the amount of nickel and copper appearing in each discharge. The mass spectrometer was first set to transmit only nickel ions, then time-resolved data were collected with a multichannel analyzer over the entire pulse period (50 msec) so that pulses from both discharges could be recorded. This allowed analysis of both the nickel pulse (the parent discharge) and the copper pulse (the auxiliary discharge that indicated the amount of contamination by nickel deposition onto the copper pin). The process was then repeated while transmitting copper ions through the mass spectrometer. The ion signal intensities listed in Table IX are typical of the cross contamination observed between cathodes. Values listed in the table are the total number of counts observed using a 800 μ sec data window placed in the plateau region of each pulse. Both discharges were operated in 1 Torr argon with a pulse voltage of ~ 1000 V. Canyavar between pins was 0 to 10 % of the parent ion signal. To reduce the amount of cross contamination, a 10 mm x 10-cm stainless steel plate was placed between the two cathodes to block any line-of-sight interactions between the cathodes. The grounded shield was mounted onto the exit orifice plate, as illustrated in Figure 52. With the shield in place, canyavar was reduced to 0.1 to 0.3 % of the parent ion signal (into the background noise). Similar results were obtained using the same configuration with iron and copper cathodes. Pressure appeared to have little effect on the degree of cross

TABLE IX
CROSS CONTAMINATION WITH AND WITHOUT
A SHIELD BETWEEN THE SAMPLE CATHODES

	parent signal in primary discharges		cathode in secondary discharge		percent cathode
	counts	error	counts	error	
^{241}Pu without shield	4443	± 44	184	± 23	3.7 %
^{241}Pu with shield	2629	± 37	3	± 1	0.11 %
^{60}Co without shield	4363	± 173	330	± 18	6.5 %
^{60}Co with shield	2714	± 117	9	± 3	0.33 %

Error value based on signal standard deviation for four separate measurement

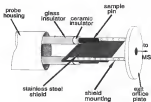


Figure 32 Stainless steel shield assembly attached to exit orifice plate

contamination and changing the discharge voltage did not alter the percentage of sintering between cathodes.

While placing a shield between the cathodes reduced the amount of cross contamination, it also reduced the observed ion signal intensity. For the 0.5 mm wires, the signal was reduced by approximately 50 % with the shield in place. When using 2 mm diameter cathodes, the signal loss due to the shield increased to as high as 80 % of the unshielded signal. This effect is most likely due to the shield interfering with the diffusion of sputtered atoms into the discharge space. The shield intercepts many atoms that would otherwise have contributed to the ion signal intensity. This reduction in signal intensity results in lower sensitivities. With the instrument used in these studies, which normally obtains sensitivities in the low ppm range, placing the grounded shield between the samples reduced the sensitivity by a factor of ten.

Analytical Applications

Comparing Identical Samples

It was necessary to evaluate the performance of the dual pulsed discharge using identical samples before the technique could be applied to the analysis of unknown materials. Two cathodes analysed under the same operating conditions should yield the same ion signal intensities. Using the dual discharge conditions such as tuning and discharge pressure are the same for both cathodes because there is only one discharge chamber and all the ions must pass down the same

mass spectrometer with a single set of operating parameters. With the dual pulse configuration, the most difficult variable to control is sample positioning. Asymmetric positioning of the samples relative to the exit orifice results in ion sampling that favors one of the cathodes. To confirm that both cathodes were sampled evenly, ion signals for the base metals are normalized to the same intensity. This was done by alternately pulsing the two discharges and observing the pulsed ion profiles at a single mass in real-time on an oscilloscope. The pulse plateaus were then brought to the same intensity by adjusting the position of the insertion probe relative to the exit orifice using the turnstiles on the below assembly.

Two SPM 1202 low alloy steel pins were selected for the twin pin comparison. Each pin (2 mm diameter) was mounted onto the insertion probe so that it was parallel to the grounded shield with its center 4 mm away from the shield. This distance allowed the sputter space to form around each sample to ensure even sputtering while keeping the pins near the exit orifice. The systematic positioning of the two pins was verified by monitoring the $^{56}\text{Fe}^+$ signal while adjusting the position of the insertion probe.

The samples were simultaneously pre-sputtered for 15 minutes using a single dc power supply connected to both cathodes. After the pre-sputter "clean up" was complete, the alternating pulse cycle was started. Data were collected using a 2 mm slit slit gate placed over the plasma region of each pulse as illustrated in Figure 63. Comparative mass spectra were accumulated with one

cathode at a time. After completing a mass spectrum in synchronism with one sample pin, a complementary mass spectrum was immediately accumulated for the second cathode. Both discharges were operated at 1 Torr argon and a discharge voltage of -1000 V . The pulse reversed to its with each pulse being 8 msec with a 5 msec decay period between alternate pulses. The data gates were positioned at the end of the QM duty cycle to allow each pulse to equilibrate before collecting data. Listed in Table X is a comparison of the intensity of three isotope elements and a minor isotope of the base matrix. The values listed are the average of four separate runs for each pin and the resulting standard deviation. Average peak intensity for the measured isotope between the two discharges is within the standard deviation of the measurements. These data show that it is possible to obtain mass spectra from alternating pulses that are representative of the cathodes and that a direct comparison of the pulsed spectra is a feasible procedure.

Analysis of Unknowns

Having demonstrated that it is possible to obtain comparative mass spectra using dual pulsed discharges, the next step was to evaluate the feasibility of comparing two samples with different composition. In this experiment, an SRM 1262 pin was alternately pulsed with an SRM 1263 pin. One sample served as the standard and the second sample as a surrogate unknown. The samples were prepared in the same manner as the analysis of both cathodes. The position of

TABLE X
COMPARISON OF SIGNAL INTENSITIES FOR TWO IDENTICAL SAMPLE
ELECTRODES USING THE DUAL PULSED DISCHARGE

element	sample #1	sample #2
iron (50)	11340 \pm 644	11312 \pm 399
nickel (58)	20305 \pm 82	20099 \pm 65
cobalt (59)	12300 \pm 42	12231 \pm 31
copper (63)	8066 \pm 52	8068 \pm 18

the insertion probe was adjusted to normalize the plateau height of the ^{59}Fe signal. Both discharges were operated with a peak voltage of ~ 1050 V and a pressure of 1 Torr argon. As before, data were collected in the plateau region of each pulse. The pulse rate was 50 Hz, with each discharge operating at a 25 % duty cycle and 5 msec between alternate pulses.

A comparison of the two cathodes is summarized in Table XI. Because the goal is to determine relative intensities between the samples, the results for each isotope are reported as the ratio of the peak intensity from the SRM 1262 sample divided by the peak intensity from SRM 1262. Also listed are the theoretical ratios based on the certified assays supplied by NIST for these materials. The error between the "standard" and the "unknown" averaged around 4 %. These results are comparable with values obtained by other researchers using RFA to determine the concentration of bulk low alloy steels (6, 11-14), an example of which is listed in Table XI.

The preliminary tests of the dual pulse discharge indicate that this technique is a viable method for the analysis of unknown materials and that its performance is comparable to using RFA. It is noteworthy that these results were obtained with the same investment of operator time required to determine the sensitivity factor for one standard sample. Furthermore, directly comparing the spectra from the unknown and the standard eliminates the uncertainty as to whether sensitivity factors developed with other samples at different times are accurate.

TABLE XI
Comparison of SRM 1262 & SRM 1263

Ratio	^{60}Co	^{63}Ni	^{64}Cu	^{67}Zn	^{109}Ag	^{107}Mo
Observed	0.163	0.537	0.188	0.282	0.171	0.383
Calculated	0.160	0.533	0.192	0.250	0.163	0.426
Error	4.5 %	0.75 %	2.1 %	13 %	4.9 %	9.1 %

All values based on (SRM 1262/263/1265)

TABLE XI
ANALYSIS OF NIST 1184 USING RSF8
BASED ON THE ANALYSIS OF SIX NIST STEELS

	Vanadium	Chromium	Manganese	Nickel
Measured	0.30	0.083	1.28	0.126
Certified	0.29	0.070	1.32	0.136
Error	3.5 %	6.4 %	3.2 %	7.1 %

From: Bousner et al. [74].

All concentrations were reported as weight percent.

CHAPTER 1 RADIO-FREQUENCY GLOW DISCHARGE MASS SPECTROMETRY

Experimental Considerations

Background

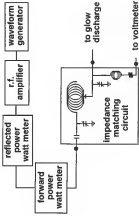
Radio frequency glow discharges were first used as a method to freeze gases for analysis with mass spectrometry [123, 124]. Possibility of using the r.f. discharge to sputter nonconducting materials was demonstrated in 1930 [50], and shortly thereafter, Coburn and Kay reported using the r.f. discharge as an atomization and ionization source for mass spectrometry [43]. In 1970, Donohue and Harrison reported an r.f. cavity ion source for the analysis of metals and solution residues [45]. The method was reintroduced in 1988 by Gudekorth and Marcus [105] for the analysis of metals and glass matrices.

While the electrical properties of r.f. discharges have been studied by the sputter deposition community, how these properties interact to produce ions for mass spectrometric analysis has not been investigated. The work reported in this chapter explores how factors such as pressure, sampling distance, and r.f. operating frequency affect the mass spectrum of both conducting and nonconducting samples.

Experiment

When using a d.c. glow discharge, the power supply is connected directly to the cathode. This simple connection is not possible when using an r.f. power supply. Radio frequency amplifiers are designed to terminate into an impedance of 50 Ω , other impedance values result in a portion of the power reflecting back toward the power supply [126, p. 585]. Under extreme conditions, this reflected power creates a standing wave that can build up sufficient heat to damage the cable-carrying the r.f. voltage. The impedance of a glow discharge operating at 1 Torr in the low MHz range can vary between 100 to 1000 Ω , depending on the pressure and operating frequency [64]. To correct this impedance mismatch, it is necessary to articulate the required 50 Ω impedance by placing a reactive network between the r.f. power amplifier and the discharge [127], as illustrated in Figure 10. The impedance-matching circuit used here was built by Mr. Bill Fure (Pittman MAT, San Jose, CA) and relies on a capacitor-inductor-capacitor circuit, called a pi-network [128, p. 387]. By adjusting the capacitors in the pi-network the reflected power is minimized while the forward power is maximized. Impedance matching is monitored by measuring the forward and reflected power into the impedance matching box. This is done with two in-line directional power meters (Jerd, Model 40) that are respectively coupled to the travelling r.f. wave and balanced for sensitivity to waves travelling in only one direction. One meter monitors the power entering the impedance matching network, while the second meter monitors the reflected power returning to the power supply.

Figure 23: Impedance matching network.



The inductor in the pi-network determines the resonance frequency of the circuit and controls the frequency at which the discharge is operated. By changing the position of the center tap on the inductor coil, it is possible to vary the operating frequency of the discharge from 3 to 11.5 MHz. The rf power amplifier and matching circuit are at any convenient distance from the impedance matching circuit. The distance between the pi-network and the discharge, however, must be as short as possible to minimize power losses from reflections between the discharge and the matching circuit.

In order to protect the sample mounting hardware, it was necessary to modify the shield normally used with a d.c. discharge. A ceramic shield would be required in an rf discharge because a d.c. bias forms on any insulating surface between the driven electrode and ground. The problem was overcome by designing a ceramic shield covered with a conducting skin (usually aluminum foil). The shield design is illustrated in Figure 54. The shield is protected by grounding the conductive skin, creating a counter electrode at the same potential as the discharge housing. A copper or nickel wire-wire ring is placed over the end of the shield to provide a grounded surface near the sample. This prevents the formation of a discharge on the sample holder by producing an anode dark space near the edge of the sample.

Because the d.c. bias voltage is the key factor controlling sputtering and electron emission in an rf discharge, it is important to monitor this voltage as it forms on the sample surface. To perform this task, a 50Ω impedance resistor is

Figure 34 Example signal for an RT channel

STAINLESS STEEL
PROBE BODY

FEEDTHRU
WELDED TO
PROBE BODY

MACOR SHIELD
WITH COPPER SKIN

CERAMIC INSULATOR

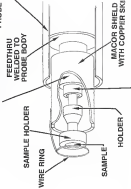
SAMPLE HOLDER

WIRE RING

SAMPLE

HOLDER

GLASS SHIELD

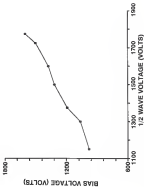


connected parallel to the high voltage circuit. An inductor is placed between the resistor and the high voltage to isolate the measuring circuit from the r.f. portion of the voltage (see Figure 53). The measuring circuit is then connected to an external voltmeter that has a $10^9 \Omega$ input resistance, creating a 1000:1 voltage divider that can be used to measure the d.c. bias on the sample. Because a nonconducting sample acts as a capacitor, the charged surface exposed to the discharge is isolated from the measuring circuit. In this situation, it is possible to measure directly the d.c. bias if the voltage "leader" around the insulator placing a charge on the insulating hardware (320). Fortunately, because the plasma is allowed to form near the edge of the sample electrode, the shield illustrated in Figure 54 allows charge to impart to itself around the edge of the nonconducting sample. This allows the bias voltage to be measured without spattering the sample holder.

Parameters Influencing r.f. Discharges

There is a direct correlation between the r.f. voltage across the discharge and the d.c. bias voltage that forms on the sample, as seen in Figure 55. A significant amount of sample heating occurs in r.f. discharges as power is dissipated by the sample and probe (130). Finding the discharge conditions that minimize the amount of power required to form the r.f. voltage across the discharge (and the d.c. bias voltage) would improve impedance matching conditions and protect the sample from excessive heat. The two parameters that

Figure B6: Relation between the bias voltage (y-axis) and applied RF voltage (x-axis), reported as 10 peaks in peaks voltage).



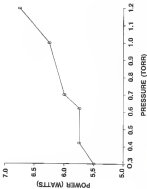
influence the formation of the d.c. bias voltage are pressure and operating frequency.

Pressure

Illustrated in Figure 58 is the effect of pressure on the amount of power required to maintain a -1000 V d.c. bias voltage on a low-alloy steel sample with an operating frequency of 8 MHz. From the figure, it is apparent that less power is required to drive the desired d.c. bias at lower pressures. To explain this phenomenon, one must consider how the d.c. bias forms on the sample surface.

The d.c. bias voltage is the result of the difference in mobility between electrons and positive ions as they neutralise the charge that builds up on the sample surface, as explained in Chapter 1. The intensity of the charge that forms on the sample surface is determined by the amplitude of the applied voltage as it oscillates above and below ground. Therefore, the d.c. bias voltage is dependent on the peak-to-peak voltage appearing across the discharge (as illustrated in Figure 59). Blanger and Fleming [54] have investigated the relationship between pressure and the peak-to-peak voltage. They applied a constant forward power of 5 watts to a glow discharge tube consisting of two parallel plates of equal size (5 cm diameter). Because the electrodes were symmetrical, no d.c. bias was observed. They reported an increase in the peak-to-peak voltage across the discharge as the pressure decreased, as seen in Figure 60. This effect was attributed to the amount of power dissipated across

Figure 10: Effect of pressure on the amount of power required to maintain it at a bias voltage of -1000 V



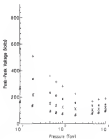


Figure 57 Peak-to-peak voltage across an argon discharge as a function of frequency and pressure (□) 7.1 MHz (+) 10.1 MHz (*) 14.1 MHz (□) 20.0 MHz (Δ)

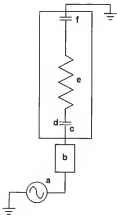
the discharge as the width of the dark space changed with pressure. The dark space and the negative glow can be modelled as a capacitor and a resistor connected in series, as illustrated in Figure 18. The width of the dark space is determined by the distance between the cathode and the point where a neutral plasma is reestablished. This occurs when the flux of electrons exiting the dark space is balanced by the flux of positive ions entering the electric field. As the pressure is reduced, the density of atoms available to form the ions necessary to balance the electron flux also decreases, forcing the dark space to extend further into the discharge space to attain equilibrium. The capacitance of the dark space decreases (121) as it expands because of a decrease in charge density. The capacitive reactance (X_C) of a capacitor to an a.c. waveform is related to both capacitance (C) and frequency (f) by

$$X_C = \frac{1}{2\pi fC} \quad (20)$$

and the average power (P) applied to the discharge is

$$P = \frac{1}{2} I_r^2 \sqrt{R^2 + X_C^2} \quad (21)$$

Figure 56. Equivalent circuit for an rf glow-discharge: (a) rf power source, (b) impedance matching circuit, (c) sample, (d) dark space, (e) negative glow, and (f) anode dark space.



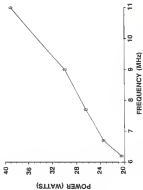
where R is the resistance, I is the maximum current, and ϕ is the phase between the maximum voltage and the maximum current. As the capacitive reactance of the disk space increases with decreasing pressure (due to the decreased capacitance of the disk space) the power applied to the discharge increases as manifested by the higher peak-to-peak voltage. The higher voltage across the discharge increases the d.c. bias appearing on the sample as the pressure decreases.

Discussion

Summarized in Figure 56 is the effect of frequency on the amount of forward power required to form a -1500 V d.c. bias in a 1 Torr argon discharge using a low-alloy steel sample. The frequency range from 3 kHz to 11 kHz represents the window within which our system is capable of operating. It can be seen in the figure that lowering the operating frequency decreases the power required to form the d.c. bias.

To explain the effect of frequency, refer to Equations (25) and (26). As with capacitance, decreasing the operating frequency increases the capacitive reactance of the disk space allowing a higher peak-to-peak voltage to form across the discharge. This is the same effect noted by Gierlinger and Flammig in their parallel electrode system (see Figure 57). Therefore less power is required to generate the d.c. bias voltage at lower frequencies.

Figure 6B Effect of frequency on the amount of power required to maintain a 1000 V dc bias. Operating conditions with 1 Torr



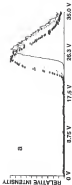
Comparison of d.c. and r.f. Discharges

Ion Kinetic Energy

Comparing the ion signals observed from a d.c. discharge with those obtained from an r.f. discharge provides a reference point for characterising operating parameters in the r.f. system. Instantant optimisation can have a significant effect on ion signal intensities. Optimum tuning parameters (e.g., Baseel box voltage) often depend on the kinetic energy of the ions sampled by the mass spectrometer. Before a comparison of the mass spectra can be meaningful, the kinetic energy of the ions in the d.c. and r.f. discharges must be determined and operating conditions selected that yield similar tuning requirements for both types of discharges.

The average kinetic energy of ions in the discharge can be determined by monitoring the ion signal at a single mass-to-charge ratio while sweeping the potential on the Baseel box. As noted in Chapter 2, absolute ion energies cannot be determined in our system, but the relative energy of the ions in the two types of discharges can be examined. Figure 10 is a collection of energy spectra for the $^{36}\text{Ar}^+$ isotope from two r.f. discharges (one operating at 4.4 MHz and other at 11.8 MHz) and a d.c. discharge. The peak voltage for all three discharges was 10250 V in a 1 Torr argon environment. The values along the x-axis represent the voltage applied to the housing of the Baseel box and are indicative of the energy of the ions passing through the energy discrimination filter. As indicated in the

Figure 16: Energy spectra for ^{79}Br at 0.5 Torr. (a) 1.0 bar argon pressure. The solid line (—) is the 4.4 discharge, open circles (○) are the 11.4 Mbit discharge, and the dotted line (···) is the 4.4 Mbit discharge. The peak voltage was 100 kV. The lower pressure peaks at lower energy are resulting from beam collisions and are not spread in ion kinetic energy.



figure, the d.c. discharge yields ions with higher kinetic energy than those sampled from an r.f. discharge. Pressure has only a small effect on the ion kinetic energy maximum for the d.c. discharge. In contrast, r.f. ion energies at 0.4 and 11.3 MHz are lower than the d.c. ion energies at 0.5 Torr, but are more closely matched at 1 Torr. Frequency does not appear to have a significant influence on ion energy in the r.f. discharge. Because the ion energies are similar at 1 Torr, timing requirements for the mass spectrometer for d.c. and r.f. discharges are more closely matched at this pressure.

As described in Chapter 3, Fanning ionization yields ions with higher kinetic energies than those observed when electron ionization is present (as indicated by the higher thermal ion voltages required to observe the afterpeak in the pulsed discharge). While Fanning and electron ionization are occurring in both d.c. and r.f. discharges, the relative role played by each ionization mechanism may not be the same. One possible explanation for the differences in ion energy between r.f. and d.c. discharges is that Fanning ionization plays a more dominant role in the d.c. discharge than in the r.f. system, resulting in higher average kinetic energies of the sampled ions.

Fanning ionization could also account for the larger difference in ion energy observed for d.c. and r.f. discharges at 0.5 Torr. It has been established that the metastable atom population increases at around 1 Torr argon (110) in a d.c. discharge. It is possible that the relative contribution to the overall ionization by Fanning may be pressure-dependent in an r.f. discharge. A change

in the contribution of Penning ionization with changing pressure would account for changes in the kinetic energy of ions observed by the mass spectrometer. The relative role of Penning in the d.c. discharge may be less susceptible to pressure variations, hence pressure has a smaller effect on the energy spectrum. Unfortunately, these are conditions that cannot be directly measured. While the metastable population in different discharges at various pressures can be measured, what percentage of the ions observed by the mass spectrometer results from Penning ionization is still an unknown quantity.

Sampling Distance

The sampling distance is the separation between the end of the cathode and the exit orifice leading to the mass analyzer. While both discharges must be operated at the same pressure to make any comparison equitable, sampling of n. and r.f. discharges at the same cathode to exit orifice distance may bias the results if the optimum sampling distance for the two types of discharges is different.

Earlier work has determined that d.c. discharges yield the highest analytical signals at a sampling distance of approximately 8 mm (18). To determine if the optimum sampling distance was the same for the r.f. discharges, the intensity of the ion signals at different sampling distances was determined using a 4 MHz discharge operating at 1000 V using a 1 Torr argon environment. Illustrated in Figure 81 is the relative ion signal observed as the sampling distance is varied

Figure 61. Methanol ion signals for $^{12}\text{C}_2\text{H}_4^+$ from a d.c. and an r.f. discharge as a function of sampling distance



from the edge of the disk space to 15 mm. The ion signal intensity from a d.c. discharge is also plotted as a reference. As was the case for the d.c. discharge, the r.f. system optimizes at approximately 5 mm from the end orifice.

Because the ion signals from d.c. and r.f. discharges optimize at the same sampling distance, it is possible to place the insertion probe at a fixed position in the discharge chamber, thereby eliminating one variable that must be reproduced when comparing the two discharges. Moreover, the shield design outlined in the previous section works equally well with both d.c. and r.f. discharges, allowing the same sample and insertion probe to be used with both discharges. Table XII lists the parameters used for the comparison study.

Comparison of Ion Signal Intensities

A comparison of the ion signal intensities between d.c. and r.f. discharges was compiled using an SPS-126-100 alloy steel disk, 4.85 mm in diameter with 0.5 mm extending into the discharge, and operating with the discharge conditions outlined in Table XII. The d.c. discharge was operated at -1000 V with a current of 4.85 mA. Operating conditions for the r.f. discharge were -1000 V d.c. bias and a forward power of 17.0 watts. Mass spectra were accumulated in the range of 30 to 70 atomic mass units, a region that has an abundance of elements commonly used for alloying steels. Summarized in Table XIV are the peak intensities for various elements observed from both discharges. Values listed in the table are based on the integrated area under each peak (reported as total

TABLE XII
PARAMETERS USED FOR COMPARISON
OF d.c. AND r.f. GLOW DISCHARGES

Parameter	Comments
Pressure: 1 Torr	Ion energies for d.c. and r.f. are similar at this pressure, allowing similar tuning conditions
Frequency: 4 MHz	Minimizes the power required to generate the desired d.c. bias voltage
Sampling Distance: 9 mm	Ion signals from both d.c. and r.f. discharges optimize at this sampling distance
Reference Point: d.c.—applied voltage r.f.—d.c. bias voltage	Matches the bombarding energy of ions onto the cathode

TABLE XIV
COMPARISON OF d.c. AND r.f. ION SIGNALS

	d.c. discharge			r.f. discharge			r.f. — d.c. ^a
	peak area	error	RSD	peak area	error	RSD	
¹⁴ N ⁺	118041	±1478	1.2%	190087	±17143	8.5%	1.82
¹⁶ O ⁺	920009	±16111	0.2%	269034	±18079	6.5%	1.88
¹⁸ O ⁺	312043	±1804	0.57%	847033	±35517	4.1%	1.39
¹⁹ F ⁺	458471	±49132	0.83%	199317	±42155	5.5%	1.54
²⁸ Si ⁺	128112	±41132	1.1%	156129	±19080	6.4%	1.55
³⁰ Si ⁺	118115	±128	1.2%	18752	±15363	8.5%	1.51
³² S ⁺	2888	±208	5.2%	6663	±164	9.4%	1.39

^a Peak area from r.f. discharge divided by peak area from d.c. discharge.
Error values based on the standard deviation of three consecutively collected mass spectra.

counts). Each value is calculated from the mean area for three consecutively collected mass spectra, each of which was an accumulation of 10 scans. Also listed are the relative standard deviations and the ratio of the r.f. peak areas divided by the d.c. peak areas.

The immediate observation based on the data in Table XIV is that r.f. discharges yield higher ion signal intensities than d.c. discharges when operated at the same voltage. The r.f. ion signals are between 1.82 to 1.88 times higher than their counterparts. These data are typical of the results obtained from other studies comparing the two discharges, though the improvement in the r.f. signals over d.c. varies between 30 % to 100 %, depending on the instrument using. The tuning for the comparison here released an optimizing the d.c. signal, then collecting the r.f. signal with the same tuning values. Although the ion signal intensities are higher in the r.f. discharges, the relative precision of the measurements is lower. Relative standard deviations (RSD) in Table XIV show that the r.f. discharge signals vary between 4 % to 8 %, while the RSD-values for the d.c. discharges vary from 1 % to 3 %.

Sputter Sputtering

In order to account for the difference in signal intensities, it was necessary to determine the amount of material each discharge was sputtering into the negative glow. To do this, the neutral population of the base noble material (pro) in the negative glow was measured using atomic absorption (AA) spectroscopy

The AA setup used in these experiments is illustrated in Figure 82. Listed in Table XV is the absorbance data for the 394.3 nm line for neutral van at various discharge voltages. The data in the table were collected at the same time as the ion intensities listed in Table XIV. These absorbance data indicate that at -1000 V, the r.f. discharge sputters approximately 14 % more material into the negative glow than the d.c. discharge.

One reason for the difference in neutral population between the two discharges may be that the current density is higher in the r.f. discharge. The d.c. and r.f. discharge comparison is based on using the same applied d.c. voltage and the d.c. bias voltage in order to match the impact energy of ions striking the sample surface. This does not imply, however, that the current density in the two discharges is the same. In a d.c. discharge, current is measured by placing an ammeter in series with the discharge. No such device for the r.f. discharge is currently available in our laboratory. Calculating the current based on the forward power (17 watts) and the bias voltage (-1000 V) yields an r.f. discharge current of 17 mA (as compared to the measured current for the d.c. discharge at 8-85 mA). Although this calculation suggests that the current is higher in the r.f. discharge, the value is not reliable because the forward power readings also include power losses due to capacitive coupling with the grounded insertion probe.

Another factor that could increase sputter yield is cathode heating during the sputtering process. Heat builds up during the sputtering process in both

Figure 10. Atomic absorption spectra (apod.) (1) hollow cathode lamp, (2) discharge, (3) 100 mesh plasma source
 ions, (4) glow discharge, (5) microtronator (and high flux mode at 114), (6) ion column ion mass analyzer, (7) 100
 mesh, (8) synchronization signal from discharge, (9) signal processor, and (10) output.

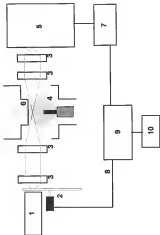


TABLE XV
NEUTRAL IRON POPULATION IN
D.C. AND P.L. GLOW DISCHARGES

voltage	r.f. discharge		d.c. discharge		percent difference
	absorbance	error	absorbance	error	
-1000 V	0.06	± 0.04	0.44	± 0.02	14 %
-750 V	0.60	± 0.02	0.81	± 0.01	37 %
-500 V	0.51	± 0.03	0.78	± 0.01	65 %

Error based on the agreed standard deviation (3 σ sampling).

discharges, but the r.f. discharge is unquestionably hotter. Increased ion current density would account for some of the additional sample heating observed in the r.f. discharge, although capacitive coupling between the high voltage lead and the grounded probe body is also responsible for sample heating.

Sample heating can affect more than the sputter yield in the r.f. discharge. As the temperature of the insertion probe increases (because of sputtering or capacitive heating), its impedance changes, altering the efficiency with which power is transferred to the discharge. This may account for the reduced precision observed for ion signals from an r.f. discharge as compared with a d.c. system. As the temperature of the probe varies through the course of the analysis, small changes in the system impedance affect the power delivered to the discharge.

Analysis Location

Although the r.f. discharge sputters more sample material into the negative glow, the absorbance signal for the nuclei is only 14 % higher than the d.c. discharge. That the observed ion signal intensity for ^{55}Fe in the same discharge is over 50 % higher. To account for the additional ion signal intensity, ionization processes must be considered.

One source of additional ionization in the r.f. discharge is the motion of electrons in the electric field as it oscillates above and below ground. This is a very different situation than is the negative glow of a d.c. discharge, which is essentially free of electric fields. The motion of the electrons in the electric field

can raise the average electron temperature in the plasma, increasing the population of electrons energetic enough to contribute to analyte ionization. Peng and Idrissi (100) have investigated average electron temperatures in both d.c. and r.f. plasmas using Langmuir probes. Their work indicates that the average electron temperature in the r.f. discharge is approximately 1.2 eV higher than in the d.c. discharge. This additional electron energy has also been credited with the increasing analyte emission signals from r.f. discharges in comparison to d.c. discharges (101). It is reasonable to assume that the higher electron temperatures increase the total amount of ionization in the negative glow as well.

The occurrence of Penning ionization may also be different in the two types of discharges. The influence of Penning ionization can be ascertained by monitoring the metastable population in the discharge using AA. Table XII is a plot of the 811 nm argon metastable transition line for both d.c. and r.f. discharges at various sampling distances using ~ 1000 V discharges operating at 1 Torr argon pressure. The r.f. discharge consistently yields higher absorbance values than the d.c. discharge, indicating the argon metastable population is higher in the r.f. system. This suggests that more Penning ionization can occur in the r.f. discharge.

To summarize, r.f. discharges yield higher ion signal intensities than the d.c. discharge(s) operating at the same voltage. The r.f. discharge appears to be sputtering more material into the negative glow region, although the difference is not sufficient to account for the additional signal intensity. Electron energy and

TABLE XVI
ABSORBANCE OF METASTABLE ATOMS
IN d.c. AND r.f. DISCHARGES

sampling distance	r.f. discharges		d.c. discharge	
	absorbance	error	absorbance	error
5 mm	0.549	± 0.006	0.494	± 0.008
6 mm	0.267	± 0.005	0.258	± 0.002
7 mm	0.216	± 0.003	0.267	± 0.001
9 mm	0.187	± 0.003	0.163	± 0.002
11 mm	0.151	± 0.005	0.137	± 0.002
13 mm	0.127	± 0.002	0.113	± 0.001

Error value based on the standard deviation of 10 consecutive readings.

metallic populations are higher in the r.f. discharge than the equivalent d.c. discharge, indicating that additional ionization may be occurring in the r.f. discharge.

Applications to Nonconducting Samples

Metal Oxide Samples

Previous work using r.f. discharges to analyze nonconductors [124] did not consider the effects of various plasma parameters such as pressure and operating frequency on the d.c. bias voltage controlling the discharge. These effects are discussed in this section, as well as examining the feasibility of using an r.f. discharge to analyze small sample disks made from compressed metal oxide powders.

The current method for analyzing nonconducting materials with the glow discharge is to mix the sample into a conducting matrix (e.g., copper or silver), compress the mixture into a pellet, then sputter the compressed sample using a d.c. discharge. The r.f. glow discharge has the advantage of sputtering nonconducting materials without using a conducting matrix. Current r.f. discharge configurations using metal oxides [124] relied on a cumbersome system of compressing the powder into large disks (5 cm in diameter and several millimeters thick), then inserting the disk onto a quartz, alumina, or boron sample holder (8 cm in diameter) [125]. This configuration sputtered both the sample holder and the specimen.

The design of the sample holder reported here is significantly different. Rather than pressing the sample into a large anvil, the material is instead compressed into a cylindrical pellet 4.8 mm in diameter. The die assembly used for this operation is illustrated in Figure 63. The sample pellet is then pressed into a copper cup 4 mm in diameter and 2 mm deep. Once seated in the cup, the top portion of the pellet is cut off, leaving the sample material flush with the top of the cup. The sample was then attached to the insertion probe as illustrated in Figure 64. This design reduces the amount of material required to form the sample pellet, allows rapid sample changing, and prevents the sample holder from sputtering (a process that introduces interferences into the mass spectrum).

Three metal oxides were selected for the work reported here: lanthanum oxide (La_2O_3). Lanthanum metal oxygen bond has one of the highest dissociation energies (DE) among the metal oxides [DE: 8.2 eV, ref. 136], titanium oxide (TiO_2) due to its relatively low bond dissociation energy (5.4 eV) and uranium oxide (UO_2), because it provides both monoxide [DE: 7.6] and dioxide species. All samples were reagent grade materials stored in an oven at 120°C to minimize the amount of water adsorbed on the surface.

The Effect of Nonconducting Materials on Discharge Parameters

Illustrated in Figure 64a is a plot of pressure versus the resulting d.e. loss at a constant applied power of 10 watts using a lanthanum oxide sample (the other oxides follow the same pattern). As with conducting samples, increasing

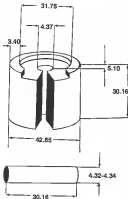


Figure 53. Die assembly used to compress powders into pellets. All components are made from stainless steel. Dimensions in centimeters.

the discharge pressure decreases the d.c. bias voltage that forms on the sample at constant applied power. The effects of operating frequency also yielded results similar to conducting samples, that is, decreasing the frequency increased the d.c. bias at a constant applied power of 10 watts. This is shown in Figure 63c using a bariumum oxide sample at 0.3 Torr argon pressure.

Illustrated in Figure 64a is a plot of the d.c. bias voltage versus the applied forward power with a discharge operating at a frequency of 4 kHz using pure uranium oxide as the sample. The pressure for this study was set at 0.3 Torr to again maximize the d.c. bias forming on the sample. The increasing d.c. bias with increasing power follows the same pattern observed with conducting samples. Figure 64a indicates that nonconducting samples respond to changing discharge parameters in the same fashion as conducting samples, indicating that the sample material does not significantly influence how the sample acquires the d.c. bias.

Sputtering oxide materials can produce both molecular and atomic species. It was necessary to determine what effect, if any, this would have on the optimum sampling distance or if atomic and molecular species would optimize at different sampling distances. Plotted in Figure 65 are the ion signal intensities for La_2O_3 and UO_2 relative to the sampling distance. Both discharges were operated with a 1000 V d.c. bias at a pressure of 0.3 Torr. The metal oxide ion signals optimized at a sample-to-exit orifice distance of 8 to 10 mm, the same sampling distance at which conducting samples optimize. Furthermore, again the metal

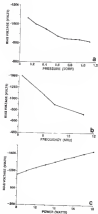
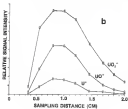
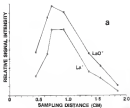


Figure 6. The effect of pressure (a), operating frequency (b) and applied power (c) on the d.c. bias voltage using a nonconducting sample.

Figure 65 The effect of sampling distance on the ion signal intensity for barium ion code (a) and uranium code (b)



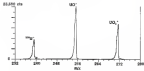
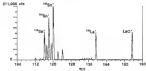
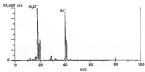
oxide and the atomic metal species reach their maximum signal intensity at the same sputtering distance. These data indicate that the atomic and molecular ion signals from a mixture of different metal oxides can be analyzed without having to reposition the sample to obtain the optimum ion signal for each species.

Mass Spectra of Mixed Oxide Samples

Mass spectra of compressed, nonconducting powders using an rf discharge were evaluated with a mixture prepared using equal portions (by weight) of lanthanum oxide, zirconium oxide, and uranium oxide. The mixture was prepared in the same manner as outlined in the preceding section by compressing the material into a pellet, then passing the pellet into the holding cup.

As with all samples sputtered with a glow discharge, the oxide mixture initially yielded only water species in the mass spectrum at the beginning of the sputtering process. Typically with bulk solids (e.g., steel samples) the water and contaminant gas signals fall to low levels (less than 5 % of the main signal) in less than 10 minutes of continuous sputtering. With the compressed powder samples, however, the water signal persisted for an extended time and never fell to levels significantly below the main material. The mass spectra in Figure 46 were acquired after sputtering the sample for 0.5 hours using a 5.0 Torr argon discharge operating at 12 watt forward power (7-1000 V d.c. bias). The top spectrum (a) is of the contaminated gas region; the middle spectrum (b) covers the

Figure S5. Mass spectrum of a mixture of lanthanum oxide, cerium oxide, and zirconium oxide.



stomium oxide and lanthanum oxide region) and the bottom spectrum (d) is of the uranium oxide region. (For clarity, each spectrum trace is normalized to the highest peak (the intensity is listed at the top of each spectrum). The most intense signal is the stomium ($211\ 000\ \text{cts. for } ^{136}\text{Ba}^+$), followed by the lanthanum and lanthanum oxide signals (around $100\ 000\ \text{cts.}$) then the water signal ($55\ 000\ \text{cts.}$), and the weakest signals are for the uranium oxide ($25\ 000\ \text{cts. for } \text{UO}^+$). The presence of water appears to hinder the breakdown of oxide species in the mass spectrum, even after an extended sputtering period.

The excess water present when sputtering the metal oxide sample is not simply the water normally encountered in the discharge chamber (because bulk materials are rid of the water interference with a short presputter period), but is instead introduced by the compressed powdered oxide material. Iida and Harrison (197) have investigated the effect of compressed powdered samples introducing water into the glow discharge. Using a sample composed of a gettering reagent (e.g., lanthanum or titanium) and a metal oxide, they were able to influence the total amount of water in the discharge by bonding the water molecules to the gettering reagent re-sputtered with the oxide. Their results indicate that a significant amount of water is introduced into the plasma from water desorbing from the surface of the powder during the sputtering process. The release of water from the sample is further exacerbated in an r.f. discharge because the temperature of the sample is increased due to resistive heating and plasma dissipation by the oxide sample (130). Without the use of a gettering

regard, or some other means to remove the water, the plasma is never rid of the water because the sample provides a continuous supply into the discharge.

Inferences from Water

The goal in elemental analysis is to reduce the analyte material into its atomic form. In the *r.f.* discharge, the presence of water in the sample prevents elements that are capable of forming strong metal-oxygen bonds from being reduced to their atomic species. As indicated in Figure 4B, the Sn and SnO signal (the oxide with the weakest metal-oxygen bond of the oxides used in this study) is dominated by the atomic form, although the oxide is still detectable. Oxide species with stronger metal-oxygen bonds such as cerium oxide and uranium produce significant molecular species and will continue to be dominated by the oxide until the water can be eliminated from the sample.

The water introduced into the plasma from compacted powder samples has other detrimental effects. Earlier work (10) has demonstrated that the presence of water in the glow discharge interferes with ionization mechanisms occurring in the negative glow, particularly Penning ionization. Furthermore, water functions effectively as oxygen in spitting material from the sample surface. These two factors, in addition to the oxidative character of water in the discharge, severely reduce the effectiveness of analyzing metal oxides with an *r.f.* glow discharge. While the use of small compacted sample pellets has the potential to

be a quick method to prepare and analyze solid samples, the utility of the technique is entirely dependent on the ability to remove water from the discharge

CHAPTER 8 AMPLITUDE MODULATED RADIO FREQUENCY GLOW DISCHARGE MASS SPECTROMETRY

Experiments/Considerations

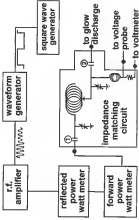
This chapter examines extending discharge pulsing techniques to the radio frequency glow discharge. The goal is to determine if the features that make pulsed d.c. glow discharges useful as a diagnostic and analytical tool can be obtained with the r.f. discharge as well.

Equipment

The radio frequency equipment used in this chapter is the same as that described in Chapter 5. The r.f. glow discharge is pulsed by modulating the amplitude of the applied r.f. voltage. This is accomplished by manipulating the waveform driving the r.f. amplifier (see Figure 87). The HP Model 3000A waveform generator has a modulation feature that attenuates the output voltage of the controlling wave in direct proportion to a 0 to ± 5 V signal applied to a terminal on the back of the instrument. By using a 50 Hz square wave, a corresponding modulation occurs on the r.f. voltage.

The pulsed d.c. discharge can serve as a reference point to which the ion signals in the pulsed r.f. discharge can be compared. This requires the use of

Figure 87 Power supply and impedance matching network for pulsed rf discharges



conducting samples such as 316L 100-series low-alloy steels. The r.f. discharge will sputter metal samples if a capacitor is placed in series between the amplifier and the discharge. In our system, this capacitor was already installed in the impedance matching line between the input terminal and the pi-network (labeled as capacitor #1 in Figure 62).

Pulsing the r.f. discharge does not appear to alter impedance matching conditions. Capacitor and inductor values suitable for the uninterrupted r.f. discharge work equally in pulsed mode. The watt meters used to monitor the forward and reverse power operate on a D Arsonval mechanism, therefore the power measurements are an average across the pulse cycle.

Pulsing the Discharge

Initial experiments pulsing the r.f. discharge were disappointing. Illustrated in Figure 64 are ion profiles for sputtered and gas species for a pulsed d.c. discharge (a) and the corresponding peaks as observed in a pulsed r.f. discharge (b). These traces were acquired at a pressure of 1 Torr, a pulse rate of 50 Hz, and a maximum applied voltage of ~ 1000 V. The afterpeak is visible on the sputtered species, but the dominant gas signals have long tails after the pulse termination. The lingering gas species signal renders time-resolved spectral discrimination useless because collecting data in the afterpeak region would still include ion signals from the dominant gases.

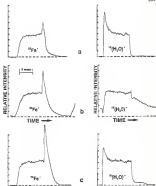


Figure 12. Intensity profiles for a) a dc discharge (a), a pulsed rf discharge with the blocking capacitor between the rf amplifier and the impedance matching circuit (b), and pulsed rf with the blocking capacitor between the matching circuit and the discharge (c). The rf discharge was operating at 4 MHz, with a 50 Hz pulse rate and a 50 % duty cycle.

The ion profiles in Figure 8(b) indicated that the glow discharge was not responding to variations in the applied r.f. voltage. If the discharge were extinguishing after the applied voltage was modulated to zero, a d.c. bias voltage would remain on the sample. The voltmeter used to monitor the bias voltage yielded only the average voltage, not the instantaneous voltage. To observe the d.c. bias in real-time, the voltage divider in the original circuit was by-passed and a terminal installed just past the inductor used to filter-out the r.f. voltage, see Figure E7. A Tektronix voltage converter (Model P6004A) was then connected to this high voltage terminal, allowing a direct measurement of the d.c. bias on the sample.

Real time measurements of the d.c. bias revealed a slowly decaying bias voltage rather than the desired sharp termination. This is shown in Figure 89. In the figure, the top voltage profile (a) is for a pulsed d.c. discharge and profile (b) is the d.c. bias voltage appearing on the sample as the pulsed r.f. discharge. Because sygon ions respond to the bias voltage, not the r.f. voltage (TM), the slow charge decay allowed the discharge to continue past the termination of the pulsed r.f. voltage. In effect, the system was not pulsing ON-OFF but instead was alternating between an r.f. discharge (when the r.f. voltage was ON) and a decaying d.c. discharge (when the r.f. voltage was OFF) that continued to sputter the gas species. The d.c. bias voltage was being maintained by the charge built up on the capacitor in the impedance matching network. The blocking capacitor, originally installed in the impedance matching block, isolates confining

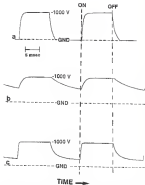


Figure 10. Voltage measurements for a pulsed d.c. discharge (a); pulsed r.f. discharge with blocking capacitor between r.f. amplifier and the impedance matching circuit (b); and pulsed r.f. with the blocking capacitor between the matching network and the discharge (c).

sample from the power supply, was located between the applied voltage and the impedance matching components, illustrated in Figure 67 as capacitor #1. Any charge built up on the sample surface included the charge on the blocking capacitor and the capacitors in the impedance matching circuit. The problem was remedied by relocating the blocking capacitor to a position past the impedance matching components, isolating the sample from the cumulative charge of the capacitors in the pi-network (illustrated as capacitor #2 in Figure 67). Confining the charge to the blocking capacitor improved the response time of the d.c. bias voltage, as seen in Figure 68c. Illustrated in Figure 68d is the effect of relocating the blocking capacitor on the sputtered and gas species ion profiles. The gas species signal now more closely resembles a pulsed d.c. discharge.

Note that the bias voltage in Figure 68c never decays to zero. This is because the charge on the sample surface can be dissipated only as long as sufficient voltage is present to maintain the discharge. The final d.c. bias in the post-pulse region represents the minimum voltage required to drive a d.c. discharge. Below this voltage, the d.c. discharge terminates and one are no longer available to neutralize the residual d.c. bias voltage.

One factor influencing the decay of the d.c. bias is the rate at which ions strike at the sample surface, which is controlled by the discharge pressure. The effect of pressure on charge dissipation is shown in Figure 70. As the pressure is increased from 0.5 Torr to 1.5 Torr, the rate at which the charge on the sample

delays increases as more ions from the negative glow arrive at the sample surface at higher pressures. These data indicate that the pulsed r.f. discharge should be operated at higher pressures (near 1.5 Torr) to maximize the rate at which the discharge is extinguished.

Comparison of Pulsed d.c. and Pulsed r.f. Discharges

A better understanding of the pulsed r.f. discharge can be gained by comparing its ion signals with corresponding pulsed d.c. signals. The comparison includes examining the time-resolved pulsed ion signal profiles, as well as overall ion signal intensities. Unless stated otherwise, the operating conditions for the two types of discharges are the same as the d.c. and r.f. comparison in Chapter 8, as outlined in Table XII.

Ion Profiles

Figure 71 shows the ion profile trace for sputtered and contaminant gas species for d.c. and r.f. pulsed discharges at the beginning of the pulse cycle. Both discharges were operating at a pulse frequency of 40 Hz and a peak voltage of 1000 V. The actual times that the signals appear in the pulse period are listed in Table XVI for several discharge pressures. The pulsed r.f. ion signals for both sputtered and gas species appear earlier in the pulse period than the pulsed d.c. signals. Analysis of the voltage on the sample using the high voltage Tektronix

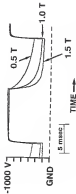


Figure 20 The dc bias voltage is a pulsed $e f$ discharge as a function of pressure

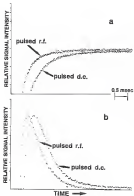


Figure 71. Expanded view of the prepeak region: (a) sputtered species (Fe^+), (b) OII species (O_2O^+). The discharge pressure was 1 Torr.

Table XVI
INITIATION TIMES FOR SPUTTERED AND GAS SPECIES
IN PULSED DISCHARGES

	0.71 Torr	1.0 Torr	1.2 Torr
d.c. $^{56}\text{Fe}^+$	1.0 msec	1.1 msec	0.97 msec
r.f. $^{56}\text{Fe}^+$	0.73 msec	0.65 msec	0.58 msec
d.c. $^{16}\text{H}_2\text{O}^+$	0.42 msec	0.37 msec	0.35 msec
r.f. $^{16}\text{H}_2\text{O}^+$	0.32 msec	0.30 msec	0.27 msec

All time measurements ± 0.03 msec.

probe indicates that the r/f discharge reaches its maximum value approximately 0.6 msec before the pulsed d.c. voltage, as illustrated in Figure 72a.

Application of the pulsed d.c. voltage is a function of how quickly the power supply can rise from ground to the maximum pulsed voltage. The r/f bias voltage, on the other hand, depends on how quickly the discharge can form, a process expedited by the residual charge remaining on the sample after the discharge is terminated (see Figure 72b). Because the residual voltage between r/f pulses is at the threshold required to maintain a discharge, the r/f pulse begins the next cycle at a point from which the discharge can be initiated almost immediately.

In order to determine if the residual d.c. bias voltage was solely responsible for the difference in initiation periods, a pulsed d.c. discharge was examined as a function of offset voltage was applied between pulses. Table XIV illustrates that the offset voltage does decrease the initiation time for gas species signals, but pulsed r/f signals still appear earlier in the period. Only when the offset voltage is high enough to maintain a discharge between pulses does the d.c. pulse signal begin at the same time as the pulsed r/f signal. Furthermore, the residual voltage between r/f pulses is -150 V in the experiment illustrated in Table XIV, yet when an offset voltage of -150 V is applied to the pulse d.c. system, the initiation time is still slower than the pulsed r/f signals. These data suggest that not only does the r/f discharge respond faster than its d.c. counterpart to the pulsed voltage, but the minimum voltage required to maintain the r/f discharge is lower than with

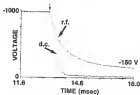
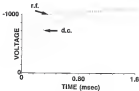


Figure 76. Pulsed voltage at the cathode: (a) prepulse region; (b) steep-spike region. The arrow indicates the time when the applied voltage is terminated.

TABLE XVIII
EFFECT OF A BIAS VOLTAGE ON
PULSED d.c. ION SIGNAL INITIATION TIMES

bias voltage	initiation time
0 V	0.342 msec
-100 V	0.323 msec
-150 V	0.304 msec
-200 V	0.304 msec
-250 V	-0.228 msec ^a
r.f. voltage -150 V	0.228 msec

^aContinuous signal between pulses

All values \pm 0.018 msec (\pm one channel number)

in the i/f discharge. This may be the result of the additional ionization possible in the i/f discharge as electrons reside in the i/f electric field.

Differences in the afterpeak region of pulsed d/c and i/f discharges can be seen by overlapping ion signal profiles in the afterpeak region, as illustrated in Figure 73. The discharges were operating at -1500 V in a 1 Torr argon environment, using a 40 Hz pulse rate with a 50% duty cycle. In the figure, the y-axis values have been equalized to draw attention to differences in the afterpeak region. Both discharges begin to show the afterpeak signal at the same time after termination of the applied voltage. The primary difference is the shape of the afterpeak; pulsed i/f discharges consistently produce wider afterpeaks than pulsed d/c discharges. Because the post-pulse region is dominated by Fleming ionization, the metastable population in the plateau region is expected to influence the afterpeak. It has already been demonstrated that i/f discharges have a higher metastable population than d/c discharges, see Table XIA in Chapter 5. The same ionization exists in the pulsed discharges, as defined in Table XIB. The higher metastable population in the i/f discharge is likely responsible for the wider i/f afterpeak. An analysis of the time-dependent metastable population in the afterpeak region would verify this hypothesis, unfortunately, the AA system currently available in our laboratory is not sensitive enough to yield reproducible signals using the narrow data gates that would be required for such a time-resolved study.

Figure 26. Expanded view of the rhomboid region



TABLE XIX
ABSORBANCE BY ARGON METASTABLE SPECIES
IN PULSED d.c. AND PULSED r.f. DISCHARGES

voltage	pulsed d.c.		pulsed r.f.	
	absorbance	error	absorbance	error
-500 V	0.008	± 0.002	0.076	± 0.002
-1000 V	0.163	± 0.003	0.182	± 0.002
-1200 V	0.206	± 0.002	0.234	± 0.003

Error values based on the standard deviation of ten readings.

Readings were taken in the plateau region. Operating pressures was 1 Torr.

Ion Signal Intensities

Comparing pulsed d.c. and pulsed r.f. ion signals requires tuning conditions that are compatible for ion signals from both discharges. An energy spectrum was compiled for each discharge and is illustrated in Figure 74. Analysis of the ion kinetic energies indicates that pulsed discharges follow the same pattern as steady-state discharges; that is, r.f. systems yield ions at lower average energies than that of dc counterparts. Unlike mass spectra acquired from steady-state discharges, however, small differences in the ion energy can have a significant effect on the plateau and afterpulse intensities (see Figure 40). Nevertheless, it is possible to minimize the effects of small tuning differences by limiting data acquisition to the plateau region which is not as sensitive to the potential on the biased ion energy discriminator as the afterpulse.

When comparing pulsed d.c. and pulsed r.f. operating at the same peak voltage, a pattern emerges whereby pulsed r.f. discharges yield higher ion signals than pulsed d.c. discharges as illustrated in Table IX. Both discharges were operating at 1 Torr argon pressure using an SFM 1264 pin (2 mm in diameter with 5 mm exposed to the discharge) with a 40 Hz pulse rate and a 50 % duty cycle. At +1000 V, ion signal intensities from the r.f. discharge are between 50 to 60 % higher than ion signals sampled from the d.c. discharge. This agrees with the results from the comparison of steady-state d.c. and r.f. discharges.

One important difference between the pulsed and the steady-state r.f. discharge is that the precision of the pulsed r.f. signal is better than its steady-

Figure 74. Energy spectra from steady-state di- and tri-charges (a) and pulsed di- and tri- discharges (b).

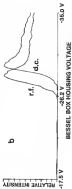
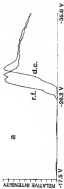


TABLE XX
ION SIGNAL INTENSITIES FOR PULSED d.c.
AND PULSED r.f. GLOW DISCHARGES

	pulsed d.c			pulsed r.f			r.f.d.c.
	peak area	error	RSD	peak area	error	RSD	
$^{51}\text{V}^+$	5640	± 188	3.3%	10637	± 174	1.6%	1.89
$^{16}\text{O}^+$	2653	± 52	3.5%	4938	± 36	0.77%	1.91
$^{56}\text{Fe}^+$	71127	± 1059	1.4%	120009	± 219	0.17%	1.78
$^{14}\text{N}^+$	12727	± 471	3.7%	24077	± 127	0.53%	1.89
$^{59}\text{Co}^+$	5204	± 143	2.8%	9699	± 100	1.0%	1.86
$^{63}\text{Cu}^+$	3760	± 217	5.8%	7242	± 105	1.5%	1.89

Error values are the standard deviations for three consecutive runs

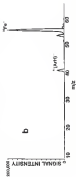
state counterpart. Typical ASD values for the pulsed r.f. discharge range between 0.6 to 2 %, as compared with 4 to 6 % using the steady-state r.f. system. The improved precision is probably due to the reduced heating of the sample and insertion probe. By operating at a 50 % duty cycle, the r.f. voltage is applied only half of the time and some of the heat that builds up can dissipate during the OFF portion of the duty cycle. This results in a constant impedance and a constant power flow into the discharge, improving the stability of the output signal.

During long periods of operation, pulsed r.f. discharges appear to be more stable than their steady state counterpart. The most common problem that interferes with r.f. discharge operation is sample arcing to the grounded outer skin protecting the inner shield. This is caused by the redeposition of sample material forming a conducting bridge that shorts-out the sample to the grounded outer skin of the shield. Pulsing the discharge reduces the redeposition rate because material is removed from the sample surface only during the ON portion of the duty cycle. Hence less material accumulates between the sample and the shield, allowing longer periods of operation without the sample shorting to ground. Reduced sample heat may also play a role in this improved stability by reducing the possibility of increased electron emission from a hot cathode surface.

Species Discrimination

It is possible to discriminate against contaminant gas species in the pulsed rf discharge by collecting data through an acquisition window placed in the afterpulse region. Illustrated in Figure 75 are mass spectra collected from a steady-state rf and the afterpulse of a pulsed rf discharge. The rf discharge was collected without the use of data gate (dead time per data point was 1 msec) and is the accumulation of 10 scans. The pulsed rf discharge was operated at 100 Hz and data was collected through a 0.4 msec data gate using an accumulation of 25 scans. Collecting data in the afterpulse region of a pulsed rf discharge reduces most of the interfering contaminant gas signals, but the process is not efficient enough to eliminate completely the interference as was possible in the pulsed d.c. discharge in the afterion region (see Figure 43). This is because the decay of the ion signals for species ionized by H_2 is not as rapid as in pulsed d.c. discharges, even when operating at higher pressures to increase the decay rate of the d.c. bias voltage. Further study is needed to improve control of the d.c. bias decay (perhaps by varying the value of the biasing capacitor to "fine-tune" the amount of charge appearing on the conducting sample's surface to yield faster bias voltage decay rates).

Figure 26: Mass spectra collected from a steady-state r^* discharge (a) and a pulsed r^* discharge using a data gate in the off-pulse region (b).



Appendix B: Measuring Oxygen

Future Discussions

Although the water content in compacted nonconducting powders severely restricts the usefulness of the r/f discharge, it was decided to investigate the effects of pulsing the discharge with these samples to determine the prospects for future work with metal oxide powders. This study was limited to La_2O_3 as the sample material, because it represents a "worst case" scenario for dissociating the metal-oxygen bond. The sample was prepared in the same manner as outlined in Chapter 5; the dried powder was compressed into a 4 mm diameter pellet, inserted into a copper holding cup, and cut level with the top of the cup. The shield configuration is the same as illustrated in Figure 164.

The first step was to determine if nonconducting powders produce the same ion signal profile that was obtained from conducting samples using a blocking capacitor. Figure 76a is an illustration of the LaO^+ signal, Figure 76b is the La^+ signal, and Figure 76c is the profile for the H_2O^+ signal. The pulsed r/f discharge was operated at ~ 1000 V d.c. bias, 5 Torr argon, and a 500 Hz pulse rate with a 50% duty cycle. The plateau heights have been matched to emphasize the prepeak and steep-rise regions. Pulsing nonconducting samples yields the same basic ion profile features as pulsing r/f and d.c. discharges using conducting samples.

Figure 76: Pulsed r.f. ion profiles for LaO^+ (a), La^+ (b), and H_2O^+ (c)



Dulse Discharge

It was of interest to determine whether the ratio of atomic to molecular species is the same in the pulsed rf discharge as in a steady-state discharge. It has been proposed (10F) that the La^+ to LaO^+ ratio changes as the concentration of water in the discharge changes (with the LaO^+ signal increasing as the water concentration increases). Figure 77 illustrates the La and LaO region of the mass spectrum. Figure 77a is from a steady-state rf discharge operating at 10 watts after the discharge stabilized (when the impedance matching requirements no longer fluctuated). Figure 77b was acquired using a pulsed rf discharge with an average forward power of 5 watts (10 watts peak power). The pulse rate was 150 Hz with a 50 % duty cycle. As before, the mass spectrum was acquired after the discharge stabilized. Both mass spectra were collected using a 2 msec data gate placed in the plateau region of the pulsed discharge. The signals from the pulsed discharge are not only more intense, but the ratio favors formation of the atomic species. This effect appears to be due to the reduced sample heating by the pulsed rf discharge. By waiting until the impedance stabilized before taking the pulsed mass spectrum, the probe and sample had time to cool, reducing the amount of water desorbed into the discharge and improving the La^+ to LaO^+ ratio.

Another interesting feature observed in this preliminary study was that the atomic-to-molecular ratio was not the same over the entire pulse period. This effect can be seen in Figure 78. Data in the figure were accumulated using a 1.5

Figure 77 Lanthanum oxide signal from a steady state rf discharge (a) and a pulsed rf discharge (b)

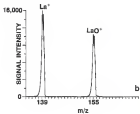
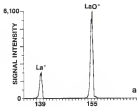
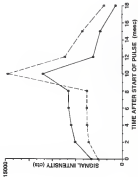


Figure 19: 1km signal intensity for LA (solid line) and LoD (dashed line) across the pulse period



meas data gate beginning at the time indicated along the x axis. The discharge was operating at -600 V d.c. bias, 4 kHz discharge frequency, and a pulse rate of 50 Hz. During the ON portion of the pulse duty cycle, the atomic species was dominant. When the applied voltage was terminated, the oxide species immediately becomes dominant. These data imply that the total amount of oxide in the discharge is not simply a function of its condition when sputtered from the sample surface, but also depends on reformation processes in the negative glow. Another factor may be that the ability of metastable species to break-up oxide bonds is not as efficient as inelastic collisions with high energy electrons. These questions warrant further study, particularly after operating conditions can be developed that minimize the release of water into the discharge so that sputtering and ionization phenomena can be separated from reactions with water in the discharge.

CHAPTER 7 CONCLUDING REMARKS

Outline

The work presented here explains and resolves analysis of pulsed glow discharges and the factors controlling the formation of the d.c. bias voltage in the r.f. discharge. This chapter summarizes the major points and common themes of the various pulsed techniques, and suggests future studies to improve our understanding and exploitation of the pulsed glow discharge.

Pulsed d.c. and r.f. Glow Discharges

There is direct correlation between the current and the voltage in an abnormal glow discharge that places an upper limit on the maximum current density and voltage at which a discharge can operate at a given pressure without overheating the sample. This is particularly troublesome when using pin shaped samples that cannot efficiently conduct their heat into the bulk of the insertion probe. Because ion signal intensity is proportional to the amount of analyte material sputtered into the discharge, it is desirable to operate the discharge at as high a voltage as possible to increase the amount of sputtered material. Pulsing the discharge provides a 'cooling-off' period between pulses that allows

a higher voltage to be used during the ON portion of the pulse period while maintaining the same average current used with the steady state discharge. This improves the sputter yield as ions arrive with higher kinetic energy, thereby increasing the ion signal intensity.

Driving the discharge at higher voltages without overheating the sample is an advantage in both pulsed d.c. and r.f. systems. It is unclear how much of a gain in sputter yield is possible by maintaining the same average current in a pulsed r.f. system because the current cannot be measured directly. One advantage that is clear when using the pulsed r.f. discharge is that the sample electrode operates at a lower temperature during pulsed discharge operation. When using an r.f. voltage, some of the power is dissipated in the insertion probe and sample electrode. Increasing the temperature of these ions and changing the impedance matching characteristics over the course of the analysis. Pulsing the r.f. discharge reduces the amount heating that the sample and probe experience, allowing the impedance to remain constant and yielding a steadier ion signal.

Isobaric interferences are a problem; the practitioner of GDMS must be aware of it in the interpretation of elemental mass spectra. Collecting mass spectra in the atterpeak region of the discharge provides a tool to deal with some isobaric interferences. The use of the atterpeak as a spectral discrimination method is a specialized application dealing with species that have ionization energies below the energy level of the discharge discharge atoms. Isobaric interferences that

can be discriminated against in an argon discharge using the afterpeak include contaminant gas species (e.g., OH^+ , H_2O^+ , CO^+ and N_2^+), combinations of gas species and sputtered analytes (e.g., FeH_2O^+) and most notably ionized species (e.g., Fe^+ and Ar^+). Interferences that form through an associative ionization mechanism with the argon metastable state (e.g., argon-metal dimers) also form afterpeaks and cannot be discriminated against using pulsed techniques. Pulsed d.c. discharges appear to perform better than pulsed r.f. discharges for spectral discrimination because the decay time for the r.f. gas species signals is not fast enough to eliminate the ionic interference, although a significant reduction in the interfering gas species signal is possible.

Because spectral discrimination in the pulsed discharge requires using narrow data collection windows, the time required to accumulate well defined peaks in the mass spectrum is increased. If the dwell time without gating is 10 msec per data point, collecting data through a 0.5 msec gate increases the data collection time by a factor of over 20. Therefore, using the afterpeak to discriminate against interferences is not well suited as a survey technique but can be applied to the determination of a particular element, or group of elements, over a narrow mass range that the spectrometer can scan rapidly.

Pulsed glow discharges have also been useful as a tool to investigate ionization in the discharge. Analysis of the prepeak region using triangle waveforms indicates that electrons emitted from the sample surface and accelerated by the electric field play a significant role in controlling the energy of

secondary electrons in the negative glow region. Operating the discharge at voltages that produce optimum ionization between the primary and secondary electrons increases the intensity of interfering gas species signals. This offers a guideline for the minimum voltage at which a discharge should be operated (typically greater than ~ 1000 V to minimize gas species signals). Studies of the afterglow indicate that a delicate balance exists among electron ionization, Penning ionization, and the formation and destruction of metastable atoms by electrons. Rapidly reducing the discharge voltage disturbs this balance, creating a transiently increase in the influence Penning ionization has on the overall ionization in the discharge.

There is little difference in the formation of the prepeak and afterpeak between pulsed d.c. and pulsed r.f. discharges. This occurs even though the r.f. discharge depends on the d.c. bias to form a useful glow discharge, whereas the d.c. discharge requires just a voltage source to create the plasma. Furthermore, the negative-glow is an electric field-free region in a d.c. discharge, but electrons experience an oscillating field in the r.f. system. These differences appear to have little effect on the mechanisms controlling the features observed in the pulsed discharge. This suggests that the general models proposed for the d.c. glow discharge can be applied to both types of systems.

Dual-Pulsed Discharges

The dual discharge takes advantage of the inherent nature of the pulsed discharge to create two alternating discharges in the same chamber that allows the analysis of two independent cathodes. It's completed that he indicates that multiple discharges offer an alternative to the conventional method using relative sensitivity factors for quantitative analysis. By directly comparing the ion signals from two separate cathodes, the effect of many variables can be minimized or eliminated.

One advantage with the dual pulse is that the ions from both cathodes are analysed almost simultaneously by the same mass spectrometer optimized under the same conditions. The conventional method using sensitivity factors can be influenced by instrument tuning parameters requiring ion signals to be normalized to an internal standard (e.g. ^{57}Fe) before sensitivity factors can be used to determine elemental concentrations. Normalisation factors are not needed in the dual discharge because of the matched conditions. Pressure is another variable that can affect sensitivity factors. Pressure controls the current density at a fixed input voltage, which in turn affects the amount of material sputtered into the discharge. By operating the two cathodes in the same discharge chamber, both samples experience the same discharge-gas pressure.

Sample positioning relative to the exit orifice is the principal variable that must be controlled with the dual pulse configuration. Uneven sampling of the cathodes would bias the ion signals and prevent a direct comparison of the two

discharges. In order to ensure that both cathodes are the same distance from the exit orifice, the position of the cathodes is adjusted inside the discharge chamber while monitoring, in real-time, the ion signal from the base matrix of each sample with an oscilloscope. When the plateau signals of both poles are the same intensity, the samples are assumed to be positioned an equal distance from the exit orifice.

A comparison of the ion signals from two identical cathodes yielded the same ion signal intensities from each cathode, within the signal standard deviation. When comparing the ion signals from two different low-alloy steels, the observed rates of the elemental components were within 5–10% of the calculated values. These values compare favorably with the accuracy achieved using relative sensitivity factors while requiring less operator time.

Currently, the levelling factor for the dual pulsed discharge is sensitivity. A grounded metal shield must be placed between the sample cathodes to reduce the cross contamination. This shield interferes with the diffusion of analyte material sputtered from the sample surface to the exit orifice where the mass spectrometer samples ions for mass analysis. Experiments comparing pulsed ion signals with and without the shield indicate that this barrier reduces the observed ion signal intensity by a factor of ten. This gives the detection limit in the low $\mu\text{g/g}$ on the instrument used in these experiments.

Radio Frequency Discharges

Radio frequency discharges were also investigated. Three areas were emphasized: a) characterizing the parameters that control the formation of the d.c. bias voltage, b) a comparison of d.c. and r.f. discharges using low-alloy steel samples, and c) the analysis of powdered metal oxide samples compressed into small pellets.

Pressure and operating frequency are two parameters that have a significant influence on the r.f. discharge. Both factors affect the impedance across the discharge dark space and the amount of power required to generate the d.c. bias voltage. The higher the discharge gas pressure, the more power required to create the d.c. bias voltage, indicating that r.f. discharges should be operated at pressures less than 1 Torr to minimize the power requirements. Operating frequency also affects the power requirements of the discharge; decreasing the frequency from 11 MHz to 4 MHz decreased the amount of power required to form the d.c. bias voltage. This frequency is lower than that normally used with r.f. discharges (13.56 MHz), suggesting that commercial r.f. systems (which operate at a fixed frequency because of FCC regulations) are not operating at the optimum frequency for efficient power usage. The effects of these parameters are the same whether using a steady-state or a pulsed r.f. discharge.

Before a comparison of d.c. and r.f. ion signals could be conducted, conditions that minimized differences in the instrument optimization parameters

between the two types of discharges had to be determined. Direct current discharges yield ions that are higher in kinetic energy than do r.f. discharges. This may be due to Penning ionization making a larger contribution to ionization in the d.c. discharge. The tuning requirements for the d.c. and r.f. discharges (based on the Geisel box focusing voltage) are more closely matched as the pressure is increased for 0.5 Torr to 1 Torr of argon.

When comparing d.c. and r.f. discharges with the same operating voltage (~ 1500 V) at a pressure of 1 Torr, the r.f. discharge yielded ion signals 25 to 80 % higher than the d.c. discharge, depending on the tuning parameters. This improved ion signal intensity is likely due to the combination of a larger sputtered atom population in the r.f. discharge, higher average electron energy in the negative glow, and a slightly higher measurable argon population. Radio frequency ion signals, however, also had a larger percent relative standard deviation than the d.c. discharge. This is the result of the constantly changing impedance of the probe and sample because of r.f. heating.

The question arises whether it is better to use the d.c. or the r.f. discharge when analyzing conducting samples. While the r.f. discharge yields higher ion signals, it is more difficult to operate than the d.c. system because of the need to impedance match the discharge and the power supply. In analyses that deal exclusively with bulk conducting samples, or in situations where the sample is easily damaged by heat, it is probably better to use the d.c. system. In situations that require dealing with a variety of samples, the r.f. discharge may be the better

choice because of its ability to handle both conducting and nonconducting samples. This is especially true if an efficient cooling method is available (as when dealing with large disk-shaped samples) or when using an automatic impedance matching system that would relieve the operator from constantly monitoring the input power.

An attempt was made to use the r.f. discharge to simplify the analysis of nonconducting powders (here, metal oxides) that are currently being analyzed by first mixing the material into a conducting matrix. These materials were compressed into small pellets (3 mm x 4 mm) and placed on an insertion probe to be sputtered directly with an r.f. discharge. While the r.f. discharge successfully sputtered and ionized the oxide materials, the ubiquitous presence of water seeping from the compressed powder interfered with the discharge operation, producing molecules, instead of atomic ion signals. The water signal was always a significant component of the mass spectrum, indicating that sputtering efficiency was low (because water is not as efficient as argon in dislodging material from the sample surface) and that ionization was not optimized (as water is known to quench the population of metastable atoms). Until the outgassing of water from powdered samples can be effectively dealt with, the use of the r.f. discharge is limited in this area.

Future Studies

Pulsed d.c. Discharges

The full analytical potential of the pulsed d.c. discharge has yet to be investigated. A close examination of sensitivity factors for steady-state d.c. and pulsed d.c. discharges (both in the plateau and the afterpeak) is needed to establish whether the changing ionization mechanisms at different times in the pulse period produce any changes in sensitivity.

It may be possible to increase overall intensity by using both the plateau region and the afterpeak of the pulsed discharge to collect data. Such a process could increase the sputtered analyte signal without adding to the contaminant gas species signal. A comparison study using the trace components of a low-alloy steel could be used to detect any gains in sensitivity using this method.

It may also be possible to increase steady-state d.c. ion signals by overlaying a pulsed discharge on top of a constant d.c. voltage. If the d.c. voltage were above the optimum voltage to form gas species, no prepeak should be formed. By applying a pulsed voltage that changes by more than 400 V, it may be possible to produce afterpeak "spikes" on the d.c. ion signal that could increase the available ion signal.

Dual Pulsed Discharges

The dual pulsed discharge may prove to be a useful alternative to the traditional methods that rely on the development of relative sensitivity factors. Its

greatest inhibition is low ion signal intensity because of interference by the grounded shield between the sample cathodes. A new shield design is called for that provides the necessary isolation between the cathodes, yet allows sufficient diffusion so as not to interfere with the ion signal intensity. One possible solution is to remove a portion of the shield near the exit orifice. This would still block any line-of-sight interactions between the cathodes while clearing the space where the mass spectrometer samples the ions in the plasma. Until a method is developed to improve the dual pulse sensitivity, the technique will be limited to identifying samples that can be distinguished using elements in the sub-parts-per-thousand regime.

One application of the dual pulse configuration may be to use the second discharge to introduce 'plasma modifying' agents. For example, gettering reagents are known to reduce the water signal observed in the discharge. The dual pulse may provide a convenient means to sputter gettering material into the discharge.

Radio Frequency Discharges

The rf discharge provides a means to analyze directly nonconducting samples. Unfortunately, the rf discharge is very susceptible to interference from water, a situation aggravated when using powdered samples because of the desorption of water from the surface of the powder particles. The situation is made worse by the sample heating that occurs in the rf system. A method is

needed to manage the water in the discharge if this system of assigning nonconduction is to be used to its full potential.

One possible recourse is the use of a liquid nitrogen cooling coil around the discharge to "freeze out" water molecules in the discharge space. This method has been successfully applied in commercial instruments using d.c. discharges to reduce water interference introduced with the discharge gas. It is unclear whether the technique would be efficient enough to deal with large amount of water introduced by the sample itself. Another alternative may be the use of gelling reagents, either mixed into the sample matrix or ejected into the plasma using a second glow discharge.

Pulsed r.f. Discharges

The pulsed r.f. discharge is a new area that will require a considerable amount of characterization before its analytical utility can be realized. For example, the dose independence between the plasma and the equipment driving the plasma warrants further study.

A pressing issue is to determine what blocking capacitor value yields the fastest d.c. bias decay times in order to remove the last traces of electron ionization from the afterpulse region. In the process of determining this value, it may be possible to calculate the actual capacitive value of the dark space, a value that is currently measured indirectly. Once better control of the pulsed r.f.

discharge is obtained, studies can begin that will draw parallels between this system and the pulsed d.c. discharge.

These proposed studies are only the "tip of the iceberg" of possible studies to improve both our understanding of the glow discharge and our ability to use it as an atomization and ionization source for analytical chemistry. No doubt these areas will provide a rich arena for further research.

APPENDIX

"IONIMPACT"

This program (written in HP BASIC) calculates the average energy of the ions striking the cathode surface, based on the calculations developed by Deane and Yverdisice (42). All distance values are in centimeters.

The dark space (L) is divided into increments (Δx). At each step, the number of ions likely to survive without further collisions is calculated (N_0). This number is then subtracted from the total current (I_0), and the process repeated at the next increment using the remaining ions. The applied voltage (V_0) is assumed to decrease linearly across the dark space. Average ion energy is calculated by dividing the sum of ion energies (ΣE) by the total current.

10	INPUT "Ca="; Ca	Number of increments from across the dark space
20	L=0.35	Length of the dark space
30	M=0.01	Mean free path
40	I=0.4E+18	Current in ions per second
50	V=1000	Applied voltage
60	X=0	X is the position in the dark space
70	N=I	
80	FOR X=L/M TO 0 STEP -1/M	Elements progress across the dark space
90	N=EXP(-X/M)*N	Number of ions striking the surface with this energy
100	N0=N0+N	Number of remaining ions
110	V=2*V*(X+M)/L	Ion energy at X
120	IF N0<1 THEN GOTO 140	
130	E=(V*N0)+E	E is the sum of ion energies
140	NEXT X	
150	I=I/N	
160	PRINT "E (average) = "; E	Generate output after stepping across the dark space
170	PRINT "N0="; N0	
180	PRINT "N="; N	
190	PRINT "V="; V	
200	PRINT "I="; I	
210	PRINT "X="; X	
220	PRINT "Ca="; Ca	
230	END	

REFERENCES

1. Serf, D.A. *Contemp. Phys.*, **22**, 27 (1981)
2. Houston, A.M. *An Introduction to Gaseous Discharges*, 2nd ed. Pergamon, New York, 1979.
3. Vais, L. *Atoms and Ion Sources*, Wiley, New York, 1977
4. Collins, J.D. *Gaseous Conductors*. Dover, New York, 1958
5. Brown, B.C. *Introduction to Electrical Discharges in Gases*. Wiley, New York, 1965
6. Harrison, W.W.; Baurick, O.M.; Ringler, J.A.; Ratiff, P.H., *Anal. Chem.*, **52**, 943A. (1980)
7. Geron, W. *Spectrochim. Acta*, **22B**, 443 (1966)
8. Russell, B.J. and White, A. *Spectrochim. Acta*, **15**, 603 (1959)
9. Gils, K. *J. Anal. Chem.*, **322**, 111 (1985)
10. Coburn, J.W. and Ray, B. *Appl. Phys. Lett.*, **25**, 380 (1974)
11. King, P.L. and Harrison, W.W. *Mass Spectrom. Reviews*, **3**, 265 (1983)
12. Von Engel, A. *Glow Discharges: Their Nature and Uses*. International Publications Services, Taylor and Francis, New York, 1963
13. Aston, F.W. *Roy. Soc. Proc.*, **94**, 326 (1916)
14. Little, P.F. and von Engle, A. *Proc. Royal Soc.*, **224A**, 209 (1954)
15. Chapman, B. *Glow Discharge Processes*. Wiley, New York, 1960
16. Chen, F.F. *Plasma Physics and Controlled Fusion*, Vol.1, 2nd ed., Plenum, New York, 1984

17. Oades, G. *J. Anal. Atomic Spectrom.*, **5**, 841 (1990)
18. Ragan, Y.M., Cohen, C., Aoki, P. *J. Appl. Phys.*, **33**, 60 (1968)
19. Harrison, W.W. and Loving, J. *Anal. Chem.*, **34**, 1525 (1962)
20. Langmuir, I. *Phys. Rev.*, **23**, 585 (1928)
21. Brown, A.K. and Matthews, J.W. *J. Appl. Phys.*, **5**, 718 (1937)
22. Massey, H.S.W. and Burhop, E.H.S. *Electronic and Impact Phenomena*, Vol. 1, 2nd ed., Oxford Press, New York, 1959.
23. Anderson, J.M. *J. Appl. Phys.*, **31**, 811 (1960)
24. Fang, D., and Marcus, R.K. *Spectrochim. Acta*, **15B**, 1269 (1959)
25. Sodman, D.H. and Bates, D.W. *Prog. In Reaction Kinetics*, **6**, 163 (1971)
26. Fearing, P.M. *Z. Physik*, **57**, 759 (1929)
27. Coburn, J.W. and Kay, E. *Appl. Phys. Lett.*, **18**, 458 (1971)
28. Davis, P.J. and Harrison, W.W. *Appl. Spectrosc. Rev.*, **13**, 201 (1978)
29. Hess, K.R. and Harrison, W.W. *Anal. Chem.*, **30**, 651 (1958)
30. Smith, R.L., Sencer, D., Hess, K.R. *Anal. Chem.*, **32**, 1123 (1960)
31. Delcroix, D.L., Feneis, D.W., Richard, A. In: *Principles of Laser Plasmas*, G. Bekefi, Ed., Wiley, New York, 1972
32. Murchio, C.C., *Science*, **122**, 585 (1957)
33. Phelps, A.V. and Molnar, J.P. *Phys. Rev.*, **85**, 1252 (1952)
34. Patch, A.H. and Green, P.A. *Phys. Rev.*, **124**, 308 (1960)
35. *CRC Handbook of Chemistry and Physics*, 65th ed., R.C. Weast, Ed. CRC Press, Boca Raton, 1985
36. Coburn, J.W. and Ray, E. *J. Chem. Phys.*, **33**, 857 (1975)

37. Hoxby, H. and Reineas, A. *J. Phys.* **225**, 68 (1969).
38. Hambeck, J.A. and Molnar, J.P. *Phys. Rev.* **85**, 821 (1951).
39. Dawson, P.H. and Tidner, A.H. *J. Chem. Phys.* **32**, 672 (1960).
40. Levy, M.K., Senner, D., Angstadt, A.D., Smith, R.L., Hess, K.R. *Spectrochim. Acta*, **22B**, 263 (1961).
41. Bethe, R. *Scattering by Particles*, *Second Edition*, Vol. 1, Springer, New York, 1967.
42. Colburn, J.W. and Harrison, W.W. *Appl. Spectrosc. Rev.* **12**, 59 (1981).
43. Davis, W.G. and Vandenberg, T.A. *Phys. Rev.* **121**, 279 (1962).
44. Alori, I., Gini, M., A., Valis-Almici, J.A. *Phys. Rev.* **228**, 2677 (1963).
45. Carter, G., Holmes, M.J., Rutherford, I.V. *Nature*, **225**, 479 (1969).
46. Lagned, M. and Wehner, G.K. *J. Appl. Phys.* **32**, 345 (1961).
47. Wehner, G.K. In *Methods of Surface Analysis*, A.W. Coatsworth, Ed., Elsevier, New York, 1975.
48. Oechler, H. *Appl. Phys.* **8**, 185 (1975).
49. Bartsch, O.M., Ph.D. Dissertation, University of Virginia (1980).
50. Carter, G. and Coligon, J.S. *Ion Bombardment of Solids*, Elsevier, New York, 1968.
51. Oechler, H. *J. Phys.* **281**, 37 (1979).
52. Bruhn, C.G. and Harrison, W.W. *Anal. Chem.* **32**, 18 (1979).
53. Navrotsky, B. *Prog. Surf. Sci.* **2**, 49 (1976).
54. Salberg, W.A. and Span, L.L. *J. Vac. Sci. Technol. A*, **8**, 2807 (1990).
55. Harrison, W.W., Hess, K.R., Marcus, R.K., King, P.L. *Anal. Chem.* **52**, 241A (1980).
56. Anderson, D.G., Meyer, W.R., Wehner, G.K. *J. Appl. Phys.* **33**, 2951 (1962).

87. Meier, S. *J Appl Phys.*, **63**, 1022 (1988).
88. Collins, J.W. and Kay, B. *J Appl Phys.*, **62**, 4895 (1972).
89. Horvath, C.M. *J Vac Sci Technol A*, **1**, 40 (1983).
90. Koenig, H.R. and Kossel, L.J. *IBM J Res Develop.*, **18**, 188 (1975).
91. Gottsche, R.A., Schaller, G.B., Steinbach, D., Inoué, T., *J Appl Phys.*, **65**, 452 (1988).
92. Kufner, M. *J IEEE Trans Plasma Sci.*, **15**, 188 (1987).
93. Bruce, R.H. *J Appl Phys.*, **62**, 7004 (1987).
94. Ditzinger, P. and Fleming, M.J. *J Appl Phys.*, **62**, 4868 (1987).
95. Sanderson R.E., Charnick, P., Hall G.J., Brown, R. *J Res National Bureau Standards*, **93**, 428 (1988).
96. Jakubowski, H., Stuever, D., Voth, W. *Anal Chem.*, **59**, 1825 (1987).
97. Harrison, W.W. *J Anal Atom Spectrom.*, **3**, 85F (1988).
98. Robinson, K. and Hall, E.F.H. *J Micro.*, **22**(1), 14 (1987).
99. Hamilton, E.J. and Mirak, M.J. *Int J Mass Spectrom Ion Phys.*, **10**, 77 (1972/73).
100. Donahue, D.L. and Harrison, W.W. *Anal Chem.*, **62**, 1828 (1990).
101. Eulen, G.G., Benz, R.L., Harrison W.W. *Anal Chem.*, **61**, 873 (1989).
102. Hunsake, J.C. *J Res National Bureau Standards*, **63**, 382 (1968).
103. Voth, M. and Hunsake, J.C. *Spectrochim Acta*, **65B**, 137 (1981).
104. Jakubowski, H., Stuever, D., Voth, W. *Fortschr Z Anal Chem.*, **32**(1), 145 (1988).
105. Mytilineou, A.P., Benishuk, P., Ergonen, B. *Spectrochim Acta Rev.*, **11**, 1 (1992).

76. Chu, P.H., Hunsake, J.O., Statner, R.J. *J. Vac. Sci. Technol. A*, 3, 305 (1985)
77. King, F.L., Ph.D. Dissertation, University of Virginia (1988)
78. King, F.L., McCormack, A.L., Harlick, W.W. *J. Anal. Atomic Spectrom.*, 3, 889 (1988)
79. Karvick, P.B. In *Trace Analysis by Mass Spectrometry*, A.J. Alcock, Ed., Academic Press, New York, 1972.
80. Miller, P.B. and Denson, M.B. *J. Chem. Ed.*, 53, 817 (1986)
81. Dawson, P.H. *Mass Spectrom. Rev.*, 3, 1 (1984)
82. Bailey, J.H. *Vacuum*, 32, 639 (1987)
83. Dawson, P.H. *Quadrupole Mass Spectrometry and Its Applications*, Elsevier, New York, 1978
84. Loran, P. and Corson, D.R. *Electromagnetism, Principles and Applications*, Prentice Hall, New York, 1979
85. Denson, J. *Vac. Sci. Tech.*, 8, 355 (1971)
86. Serway, R.A. *Physics For Scientists and Engineers*, Saunders College Publishing, New York, 1982
87. Wilson, R.G. and Grewer, G.R. *Ion Beams with Applications to Ion Implantation*, Wiley, New York, 1979
88. Harlick, W.W. and Gerts, B.L. *Prog. Analyt. Spectrom.*, 11, 59 (1988)
89. Craig, J.H. and Hock, J.L. *J. Vac. Sci. Technol.*, 12, 1268 (1980)
90. Craig, J.H. and Dumer, W.D. *J. Vac. Sci. Technol. A*, 1, 3337 (1983)
91. Watson, J.T. *Introduction to Mass Spectrometry*, Plenum Press, New York, 1989
92. Shoemaker, D.P., Garland, C.W., Steinfeld, J.I., Miller, J.W. *Experiments in Physical Chemistry*, 4th ed., McGraw-Hill, New York, 1981

- 93 Grinton, J.F. *A User Handbook to Massum Technology*. Wiley, New York, 1980.
- 94 Burrows, C.M., Lieber, A.J., Zakariass, V.T. *Rev. Sci. Instr.*, **38**, 1477 (1967).
- 95 Kart, E.A. *Am. Lab.*, **22**, 47 (1979).
- 96 Dylagerova, R.D. in *Improved Hollow Cathode Lamps for Atomic Spectroscopy*, S. Gorda, Ed., Intsted Press, New York, 1966, Chapter 9.
- 97 Dawson, J.B. and Ellis, D.J. *Spectrochim. Acta*, **23A**, 649 (1967).
- 98 Barnett, W.B. and Rahn, H.L. *Anal. Chem.*, **44**, 895 (1972).
- 99 Boorman, J.A., Sullivan, J.V. *British A. Spectrochim. Acta*, **22**, 805 (1966).
- 100 Lowe, R.M. *Spectrochim. Acta*, **24B**, 191 (1969).
- 101 Mitchell, D.G. and Johansson, A. *Spectrochim. Acta*, **25B**, 175 (1970).
- 102 Mathewson, M.B. and Hurvitz, J.K. *Appl. Spectrosc.*, **22**, 310 (1976).
- 103 van Ock, C., Smith, B.W., Winefordner, J.D. *Spectrochim. Acta*, **37B**, 755 (1982).
- 104 Smith, B.W., Greenstein, N., Winefordner, J.D. *Spectrochim. Acta*, **22B**, 1349 (1966).
- 105 Glick, M., Smith, B.W., Winefordner, J.D. *Anal. Chem.*, **62**, 147 (1990).
- 106 De Jong, G.J. and Plepmeier, E.H. *Spectrochim. Acta*, **29B**, 155 (1974).
- 107 Seidman, P.J. Ph.D. Dissertation, University of Virginia (1984).
- 108 Krampe, J.A., Seidman, P.J., Harrison, W.W. *J. Am. Soc. Mass Spectrom.*, **1**, 136 (1990).
- 109 Allinson, A.W. *Physical Chemistry of Surfaces*, 3rd ed. Wiley, New York, 1976.
- 110 Bohm, D. and Gross, E.P. *Phys. Rev.*, **75**, 1584 (1948).

- 111 Bond, M.A. *Phys. Rev.* **55**, 660 (1942).
- 112 Straus, J.A., Fennie, H.P., Hulan, H.G. *Spectrochim. Acta*, **23B**, 147 (1968).
- 113 Hardy, J.A. and Sheldon, J.W. *J. Appl. Phys.*, **33**, 8522 (1962).
- 114 Sanderson, H.E., Hall, E., Clark, J., Chamberlain, P., Hall, D. *Molecular. Acta (Phys)*, **1**, 275 (1947).
- 115 Sullivan, J.V. and Walsh, A. *Spectrochim. Acta* **21B**, 771 (1965).
- 116 Lane, R.M. *Spectrochim. Acta*, **22B**, 121 (1971).
- 117 Hulan, H.G., Seegars, P.J.T., van der, J.A. *Spectrochim. Acta*, **22B**, 111 (1970).
- 118 Wagatsuma, K. and Hirokawa K. *Anal. Chem.* **51**, 2137 (1979).
- 119 Lane, R.M. *Spectrochim. Acta* **23B**, 127 (1978).
- 120 Sullivan, J.V. and Gough, D.S. *Analyst* **122**, 907 (1975).
- 121 Harrison, W.W. and Berry, S.L. *Anal. Chem.* **51**, 1853 (1979).
- 122 Liang, T.J. and Harrison, W.W. *Anal. Chem.* **54**, 1525 (1982).
- 123 Gilkerson, J.L., Field, H., Charin, L.M. *J. Appl. Phys.* **35**, 2050 (1964).
- 124 Schout, F.C. and Heuvelink, D.D. *Inter. J. Mass Spectrom. Ion Phys.*, **5**, 21 (1972).
- 125 Quakenbush, D.C. and Mynatt, R.K. *Anal. Chem.* **51**, 1875 (1979).
- 126 Roberts, P. and Hill, W. *The Art of Electronics*, Cambridge Univ. Press New York, 1980.
- 127 Nonheims, H. and Bloch, H.-O. *Thin Solid Films*, **55**, 205 (1978).
- 128 Hollahan, J.R. and Bell, A.T. *Techniques and Applications of Plasma Chemistry*, Wiley, New York, 1974.
- 129 de Vries, G.A.M. and van den Hoek, W.G.M. *J. Appl. Phys.* **55**, 2074 (1979).

100. Womack, J.L. *J. Vac. Sci. Technol.*, **9**, 512 (1971).
101. Kotler, K., Coburn, J.W., Horne, D.E., Ray, E., Keller, J.H. *J. Appl. Phys.*, **57**, 89 (1985).
102. Fang, D. and Marcus, R.K., Paper presented at the 17th Annual Meeting of the Federation of Analytical Chemistry and Spectroscopy Societies, Cleveland, OH USA (October 7-12, 1990).
103. Winchester, M.R., Lask, C., Marcus, R.K. *Spectrochim. Acta* **45B**, 489 (1989).
104. Coburn, J.W., Tagawa, E., Ray, E. *Japan. J. Appl. Phys. Suppl.*, **2**, 801 (1974).
105. Coburn, J.W., Tagawa, E., Ray, E. *J. Appl. Phys.* **45**, 177 (1974).
106. Pading, A.A. and Smeyers-Verbeke, R.M. *Reference Data on Atoms, Molecules, and Ions*, Springer-Verlag, New York, 1980.
107. Mei, Y. and Harrison, M.M. *Spectrochim. Acta* **45B**, 135 (1989).
108. Foster, F., Lamont, L.T., Myers, G.O. *J. Vac. Sci. Technol.*, **9**, 124 (1971).

BIOGRAPHICAL SKETCH

Jeffrey Klingler completed his Bachelor of Arts degree in chemistry at the University of Southern Indiana in May 1987. His graduate career began at the University of Virginia in analytical chemistry under the direction of Willard W. Hansen. In 1989, he transferred his graduate studies to the University of Florida after Dr. Hansen accepted a position with Florida.

At both Virginia and Florida, his research interests included studies using time-resolved glow discharge mass spectrometry as an elemental analysis technique and as a method to investigate the fundamental parameters controlling the discharge. He completed his doctoral studies in August 1991 and has accepted a position as an associate research chemist with Shell Development Company.

I certify that I have read this study and that in my opinion it conforms to acceptable standards of scholarly presentation and is fully adequate in scope and quality as a dissertation for the degree of Doctor of Philosophy


Edward W. Harrison, Chairman
Professor of Chemistry

I certify that I have read this study and that in my opinion it conforms to acceptable standards of scholarly presentation and is fully adequate in scope and quality as a dissertation for the degree of Doctor of Philosophy


Richard A. Yost, Chairman
Professor of Chemistry

I certify that I have read this study and that in my opinion it conforms to acceptable standards of scholarly presentation and is fully adequate in scope and quality as a dissertation for the degree of Doctor of Philosophy


Anne P. Snyder, Chair
Associate Professor of Chemistry

I certify that I have read this study and that in my opinion it conforms to acceptable standards of scholarly presentation and is fully adequate in scope and quality as a dissertation for the degree of Doctor of Philosophy


Joseph R. Lyle
Professor of Chemistry

I certify that I have read this study and that in my opinion it conforms to acceptable standards of scholarly presentation and is fully adequate in scope and quality as a dissertation for the degree of Doctor of Philosophy


Paul H. Holloway
Professor of Materials Science and
Engineering

This dissertation was presented to the Graduate Faculty of the Department of Chemistry in the College of Liberal Arts and Sciences and to the Graduate School and was accepted as partial fulfillment of the requirements for the degree of Doctor of Philosophy

August 1991

Dean, Graduate School